LSU Doctoral Dissertations   Graduate School

2011

Structural and electronic properties of noble metals on metal oxide surfaces

Fei Wang

Louisiana State University and Agricultural and Mechanical College, fwang6@lsu.edu

STRUCTURAL AND ELECTRONIC PROPERTIES OF NOBLE METALS ON METAL OXIDE SURFACES

A Dissertation

Submitted to the Graduate Faculty of the
Louisiana State University and
Agriculture and Mechanical College
in partial fulfillment of the
requirements for the degree of
Doctor of Philosophy

in

The Department of Physics and Astronomy

by
Fei Wang
B.S., University of Science and Technology of China, China, 2004
August, 2011

To my father and my mother

Acknowledgements

At the time of finishing this dissertation writing and my graduate studies at LSU, I would like to express my gratitude to many wonderful people, who have contributed so much to my work.

First of all, I owe my deepest gratitude to my graduate advisors, Dr. Phillip T. Sprunger, and Dr. Richard L. Kurtz for their support, guidance, encouragement throughout the whole course of my PhD studies, especially the extreme efforts on revision of this dissertation for the past few weeks. They showed me the beauty of the nano-world and led me into this fascinating research area. I have learned so much from them in every aspect related to research, such as how to design and perform experiments, how to process and analyze data, how to present my work, and how to troubleshoot and fix problems. These skills are not only limited to my research, but also will be beneficial to my future work and living. I also witnessed their enthusiasm and passion about research, their positive attitude, and never give up spirit when facing frustrations. These merits have deeply influenced me and made me a better researcher and person.

I would like to show my gratitude to all my colleagues and dear friends in our lab and at LSU. I am thankful to Dr. Indrajith Senevirathne for being a loyal friend and elder brother, who is always caring and helpful whenever needed. I am thankful to Frank Womack for his endless help on showing me how to use all kinds of tools and instruments. I am thankful to Ziyu Zhang for the help on data collection and many inspiring discussions. I am thankful to Matthew Patterson for his intelligent suggestions on experimental details. I am thankful to Dr. Orhan Kizilkaya from CAMD, for his help and advice when I was taking data there. I am thankful to all the current group members and our previous undergraduate students, Brendon Watson, Justin Runnel, and Arrielle Opotowsky, for pleasant lab time we have shared.

Table of Content

Abstract

Noble metals on metal oxide surfaces play crucial roles in many catalysis applications. Due to extreme complexity of the interfaces and catalytic reaction processes, basic science studies of model systems are needed to guide the construction and optimization of new industrial catalysts. We have employed ultra-high vacuum techniques to investigate the morphology, electronic structure, and surface reactivations of clean metal-oxide/metal nanocluster interfaces in ideal conditions. The systems we chose are Ag/TiO_2, a popular photocatalyst, and Cu/ZnO, recently a hot candidate for liquid fuel production. The main characterization techniques that we have employed include Scanning Tunneling Microscopy (STM), Photoemission Spectroscopy (PES), Electron Energy Loss Spectroscopy (EELS), as well as Auger Electron Spectroscopy (AES) and Low Energy Electron Diffraction (LLED) for surface quality determination.

Ag on $TiO_2(110)$ grows in a manner that produces 3D hemispherical clusters with uniform sizes in the several nanometer range. The preparation of the surface is found to control the nucleation sites and cluster sizes. Our photoemission data show that the initial coverage of Ag has very different properties when compared with the larger clusters at higher coverage, or that of "bulk" Ag. The optical properties of larger Ag clusters show strong collective excitations at ~ 3.8eV, in the UV part of the solar spectrum. We have found that when we encapsulated the titania supported Ag clusters in a thin titania overcapping layer, the nanoclusters retain their structural integrity and we find that new excitations are induced that better match the solar spectrum. Cu on $ZnO(10\bar{1}0)$ is another sample of 3D nanoclusters that we have grown and in this case the motivation is the catalytic reduction of carbon dioxide to methanol. In this case we find that multiple Cu-oxide phases form, depending on oxidation treatment, and electrochemical measurements show that Cu(I) species of Cu_2O is particularly active on

ZnO(10$\bar{1}$0). Along with additional studies of Cu on TiO$_2$(110) and Au on ZnO(10$\bar{1}$0), we observed a diversity of metal growth behaviors on the different oxide substrates. The preferred nucleation site, cluster size, and the shape of clusters are all different for a different metal/oxide combination.

Chapter 1: General Introduction

The understanding of heteroepitaxial growth and consequent properties of noble metal-on-metal oxide systems has strong influence to a wide variety of technologically important industrial applications, particularly in the field of heterogeneous catalysis. Economically, the importance of catalysts cannot be overstated, it has been estimated the impact is over 10 trillion dollars per year worldwide. There are many excellent studies and reviews on metal-oxide interfaces [1-5]. In practical catalysts, catalytically reactive metal particles with sizes in the few- nanometers range are dispersed on dissimilar supporting materials, typically metal oxides. With dispersed metal nanoparticles, very high active surface areas can be obtained, which plays an important role in catalytic efficiency. Minimal cost can also be achieved in this way, because in the case wherein precious metals are employed, the supported metal-on-oxides are much cheaper. The metal-oxide interface plays a key role in these catalytic activities. In those catalysts, the metal oxides are not simply a physical supports for metal particles, but rather can be judiciously chosen to optimize the metal-and-oxide interaction, and consequently enhance the reactivity and selectivity. When metal-on-oxide contact is formed, both the geometric and electronic structures change. As mentioned above, many real catalysts consist of dispersed nanoparticles and supporting oxide substrate. The catalytic performance often depends strongly on the size of metal particles. For example, in the case of Au/TiO_2 catalyst used for low temperature CO oxidation, optimal catalytic efficiency is achieved when the Au clusters have a very narrow size distribution of 2 - 3nm [6]. Other variables include the degree of charge transfer to/from oxide substrate to metal particles observed in most metal-oxide interfaces, the high surface area of electron rich metal nanoparticles, and the degree to which some metal nanoparticles can be

encapsulated with a thin layer of substrate oxide, blocking their catalytic abilities [7]. In general, the understanding of the interface between the metal and oxide is crucial to catalysis process. The interface has to be optimized to achieve highest reaction efficiency and best product selectivity for certain catalysis activity. Unfortunately, due to the complexity of the catalysts, it is very difficult to optimize a given catalyst without fundamental understanding of the catalytic process. During the catalytic reactions, the exact reaction pathway is hard to decipher, as there are many intermediates involved, and the catalyst itself may also change during reaction. To elucidate the mechanism of the complex process, the first step is to thoroughly understand the structural and electronic properties of the metal/metal oxide systems, and following that, work to understand the interactions of simple molecules with them.

With the development of ultra-high vacuum (UHV) based surface science techniques, the structural and electronic properties of the metal-oxide interface can be selectively investigated, and many metal/oxide systems have been studied and discussed [3-5, 8-10]. Ideal models of metal/oxide interfaces can often be established with the aid of multiple-technique UHV surface science studies. Single-crystalline oxides cut and revealing chosen crystallographic facets can be prepared to ascertain candidates for the supporting substrates. The surface is obtained by either cleavage or by orienting and polishing, depending on the particular crystal system of interest. Metal particles/thin films can be produced by vapor deposition onto the oxide surface in UHV conditions.

The geometric structure and morphology of the surface of the catalyst can be well characterized with several different techniques, and among these, Scanning Tunneling Microscopy (STM) is an invaluable tool to "look" at the surface with resolution often at the atomic scale. With STM studies, we may be able to answer many questions regarding the structure of nanoclusters and their interface with the substrate. How does the metal grow on the oxide surface? Does first monolayer of metal deposited

on the surface wet the surface or does it grow 3D nanoparticles? Does high coverage create 3D clusters or thick films, and what are the facets and orientations of the nanoclusters that results? We can also follow how the metal particles change with different preparation and reaction conditions.

The electronic structures including details such as charge transfer can be explored with some spectroscopy techniques such as Ultraviolet Photoemission Spectroscopy (UPS) and Electron Energy Loss Spectroscopy (EELS). Photoemission provides information on the occupied electronic states, the molecular orbitals of adsorbates, and the chemical valence states taken by both substrate and metallic cluster atoms. On the other hand, EELS provides information on electronic scattering and excitation properties and can provide both electronic and vibrational information of near-surface species. These basic science studies are all performed in UHV conditions, and although there is indeed a large chasm between the well-prepared catalytic studies under UHV performed in the lab and large-scale industrial applications. However, keeping this fact ever in mind, the observation and understanding of metal-on-oxide systems (and surface chemistry thereon) under ideal conditions are essential, because they may be exploited to guide the development of technologically important, practical catalysts.

In this thesis, experimental results of two major metal/metal oxide systems will be discussed, and they are Ag/TiO$_2$ and Cu/ZnO. The two systems share many similarities. Both TiO$_2$ and ZnO are semiconductors with a wide bandgap of $\sim$ 3eV. They are the most popular catalysts in industry, covering a large variety of applications in the synthesis of a broad range of chemicals. The metals selected here all grow nanoparticles on the substrate, providing an overriding theme for their structure, electronic properties and chemical reactivities.

For the first study of Ag/TiO$_2$, we will start with the single-crystalline TiO$_2$(110) surface as a substrate, which is the most stable TiO$_2$ surface. TiO$_2$ has been the model system for surface science

studies because of its many advantages. Single crystal TiO_2 with very good polished surface can be easily purchased commercially. Although stoichiometric crystals have a wide bandgap, TiO_2 can be easily reduced by vacuum sputtering and annealing, and become an n-type semiconductor. The reduction will allow enough electrical conductivity to permit the use of STM to study its surface morphology down to the nanoscale, and this also avoids the associated surface charging problem in electron spectroscopy measurements. Most importantly, TiO_2 has played very important roles in numerous industry applications. TiO_2 is used in heterogeneous catalysis, white pigment, ceramics, self-cleaning coatings, and optical coatings [11-17]. It is also widely used for photo-induced degradation of organic wastes into CO_2 and H_2O. Most recently, nanoporous TiO_2 has become a key component of solar cells for hydrogen generation and electric power production. Unfortunately, due to the 3eV wide bandgap, which is a poor match to the solar spectrum, the conversion rate of solar energy to electricity is very low without bandgap modification. Because of this, a significant amount of work has been devoted to enhance the solar energy conversion efficiency of TiO_2. M. Grätzel proposed the so called dye-sensitized cells, which use dye molecules to absorb solar energy and couple the resulting electron-hole pairs effectively to the electrolyte to produce and efficient cell [18]. This type of cell shows very high light-to-electric conversion yield, and are promising candidates for future commercial solar cells. The solar absorption of TiO_2 can also be enhanced by narrowing the band gap, which is achieved by doping it with other elements [19-21].

In this work, we attempted to incorporate Ag nanoclusters into the near surface of TiO_2 to act as antennas for absorbing solar energy by coupling to the inherent plasmon resonance of Ag. We began with basic science studies of Ag growth on both reduced and oxidized $TiO_2(110)$ surfaces. On reduced $TiO_2(110)$ surfaces, 3D nanocluster growth has been observed for very low Ag coverage, and these

nanoclusters are preferentially nucleate and grow at substrate step edges. As the Ag coverage increases, the nanoclusters start to grow on terraces and finally disperse homogeneously across the surface. It is believed that the bonding between Ag and the reduced TiO_2 surface is weak. On oxidized $TiO_2(110)$, dissociation of O_2 will provide adatom O atoms on the surface, which greatly enhance the bonding between Ag and substrate [22]. STM reveals that at initial Ag coverage, growth of much smaller nanoclusters nucleate and grow homogeneously across the surface, and no step edge nucleation was observed. The Ag 5sp band has been found to show atomic behavior at very low coverage, whereas bulk features are seen to develop when the coverage increase to about 2ML wherein a strong indications of metallic behavior emerge. Various surface defects are created after TiO_2 has been sputtered and annealed, and these defects appear at 0.8eV below Fermi edge within the bandgap in photoemission spectra. The origin of the defect state observed in photoemission studies has been debated but most agree that it involves contributions from two sources, one being a bridging O vacancy that traps an electron and the second involving an interstitial subsurface Ti^{3+} cation [23-26]. The defect state peak in photoemission can be partially quenched upon O_2 dosage, consistent with healing of bridging O vacancies but remaining intensity indicates that the Ti interstitials in the near-surface region also contribute to the peak. In EELS measurements, the defects feature is easily quenched with only a small O_2 dosage, and it is thought to be mainly due to the surface defects (oxygen vacancies). When dosing with silver, few ML Ag on TiO_2 surface is found to exhibit a strong plasmon peak located at ~3.8eV, which can act as a light absorbing antenna. The 3.8eV plasmon energy, however is a poor match to solar spectrum, only coupling to the UV components and thus the light absorption will be very low. By coating the Ag clusters with a thin layer of titania, we expect to change the dielectric environment of the Ag clusters, thus modifying the plasmon energy to better

match the solar spectrum. EELS spectra show enhanced absorption of $TiO_2/Ag/TiO_2$ system in the 1-2.5eV energy range when we produce such a sample.

The second study in this thesis is one of Cu and Cu oxides on $ZnO(10\bar{1}0)$, which is motivated by the application of methanol synthesis from CO_2. Catalysts for methanol synthesis from CO_2/CO have been intensively investigated since the introduction of commercial catalyst $Cu/ZnO/Al_2O_3$ [27]. Cu on ZnO has been employed here as the model system to better understand the mechanisms underlying the catalytic process [28, 29]. Besides the Cu catalyst, Cu oxide was also found to have unique catalytic activities for methanol synthesis from CO_2 [30]. A non–polar $ZnO(10\bar{1}0)$ surface was chosen as the support for Cu growth studies. Vapor deposited Cu forms 3D nanoclusters nucleated along specific orientations at low coverage, while terraces are the least possible nucleation sites for Cu. Annealing Cu clusters in vacuum leads to ripening of small Cu clusters and is accompanied by strong chemical reactions between Cu clusters and the substrate, observed in photoemission and EELS measurements. Cu clusters were clearly oxidized even without addition of a background of O_2, and shallow pits found after vacuum annealing indicated the removal of O and Zn atoms to produce this oxidation. Cu clusters annealed in vacuum and background O_2 result in different oxidation states, among which Cu_2O clusters are formed and are found to be more active in the CO_2 reduction process [30]. Cu growth on $TiO_2(110)$ is very similar to that on $ZnO(10\bar{1}0)$, but Cu does not react with the substrate in this case. Another catalyst Au/ZnO has very similar catalytic activities for methanol synthesis to Cu/ZnO. Unlike Cu, Au tends to grow quasi 2D islands on the surface. Even at high Au coverage, the Au islands are still not as tall as Cu clusters. We continue with ongoing studies of these catalysts to elucidate the mechanism for methanol synthesis, and these extensive STM work could contribute as an important part.

This thesis starts with a brief introduction to the theoretical considerations, instrumentation and methodology in Chapter 2 *"Experimental Principles and Instrumentation"*, followed by Chapter 3 *"Silver growth on r- and o- TiO$_2$(110) surface"*, which describes the surface morphology and electronic properties of Ag clusters on TiO$_2$(110) substrate. Chapter 4 *"Optical excitations of metallic Ag nanoclusters buried in TiO$_2$ for solar photochemistry"* introduces a sandwich structure TiO$_2$/Ag/TiO$_2$ for enhancing solar absorption. Chapter 5 *"Cu and Cu oxides growth on ZnO(10$\bar{1}$0) and TiO$_2$(110) surfaces"* presents the STM studies of several model catalyst systems. Finally Chapter 6, *"Summary"* tries to tie together these differing sets of experiments. By comparing and contrasting the observed atomic and electronic of differing noble metal [Cu, Ag, and Au] nanoclusters on metal oxide [r- and o-TiO$_2$(110) and ZnO(10$\bar{1}$0)], it is hoped that, with further studies, general trends emerge which may truly help to nanoengineer new catalytic and photocatalytic systems.

Chapter 2: Experimental Principles and Instrumentation

2.1 Introduction

In this chapter, theoretical principles, experiment setup and instrumentation used in this dissertation research will be explained. This will include sample preparation, ultra-high vacuum (UHV) techniques, as well as surface characterization using spectroscopies, such as Scanning Tunneling Microscopy (STM), Electron Energy Loss Spectroscopy (EELS), and Photoemission Spectroscopy (PES). Additional surface science techniques will also be briefly discussed.

2.2 UHV Chamber and Sample Preparation

The key to surface science experiments is ultra-high vacuum. To keep sample surface clean and prevent it from being contaminated with residual gases, a vacuum chamber with base pressure of low 10^{-10} Torr is usually required. Gas adsorption on surface is described with unit Langmuir (L). The Langmuir unit is defined by multiplying the gas pressure and the time of exposure, where $1L = 10^{-6}$ Torr·s. This means at pressure of 10^{-6} Torr one layer of gas will be adsorbed on the surface in 1 second, assuming a unity sticking coefficient (all gas molecules collide with the surface will stick onto it). In a vacuum chamber with pressure of 1×10^{-10} Torr, the sample surface will stay clean for about 3 hours. Often the sticking coefficients of clean surfaces are much smaller than 1, which will guarantee us a course of experiment as long as days.

In order to obtain and maintain UHV conditions, three stages of pumping are needed. A roughing pump is used to pump the chamber down to 10^{-3} Torr, limited by compression of gas into the pump. The second stage of pumping is accomplished with a turbo pump, which can pump the chamber down to 10^{-9} Torr. The key component in a turbo pump is a fast spinning motor with speed as high as 70krpm. When lower pressure is desired, an ion pump is used for pumping. However, a bakeout of the chamber is usually needed to achieve very low pressure in a short period of time. The bakeout is

performed by heating the system to at least 100˚C for 24hours or even longer. The heating process removes impurities (mostly water) adsorbed on the inner walls of the chamber. Pressure in the chamber is monitored with ion gauge. In an ion gauge, residue gas molecules are ionized and collected, and the current measured is proportional the pressure.

The sample mostly studied in this work is rutile $TiO_2(110)$ single crystal. Rutile $TiO_2(110)$ crystals are purchased from several vendors, such as Commercial Crystal Laboratories, Princeton Scientific Corp., and MTI Corp. The typical sample size is 10mm×10mm×1mm, and the sample is polished on one side. The sample is mounted on a Ta or stainless steel plate and loaded into UHV chamber. $TiO_2(110)$ sample surface is cleaned with cycles of sputtering (0.5-2kev Ne^+, I_{sample} ~ 10μA, 30min) and annealing to 600˚C for 20-30min. The sample is heated by a W filament mounted at the back of the sample plate. Sometimes electron bombardment is applied to obtain high temperature with lower filament current, which is achieved by positively biasing the sample to several hundred volts. The sample temperature is monitored with type K – Chromel (Nickel-Chromium alloy)/Alumel (Nickle-Aluminum alloy) thermocouple.

2.3 Scanning Tunneling Microscopy (STM)

2.3.1 Introduction to Scanning Probe Microscopy (SPM)

Scanning probe microscopy (SPM) has been a significant advance in surface analysis, because it is able to provide three dimensional images of surfaces with a resolution on the atomic level. In general, a very small and sharp tip is used to probe the surface, because of the interaction between the probe tip and the surface, localized information on the surface can be detected. Among all the SPM techniques, atomic force microscopy (AFM) and scanning tunneling microscopy (STM) are the most important and widely used in laboratory and industry research.

STM was invented by Binnig and Rohrer at IBM Zürich in 1981, and they were awarded the Nobel Prize for Physics in 1986 [31-33]. Since its invention, STM has been an invaluable tool in

surface science research, and many reviews of STM can be found [34-36]. For very clean and flat surfaces, 1Å lateral and 0.1Å vertical resolution can be achieved with STM, which enables us to observe individual atoms on the surface. Another advantage of STM is that the operation of STM is not limited to ultra-high vacuum and other environments such as ambient (air) and water are also possible for STM conducting experiments. Recently, variable temperature STM (VT-STM) allows inspection of surfaces at temperature ranging from liquid helium (LHe) temperature (4K) to a few hundred degrees Celsius. However, there is one crucial limitation for STM measurement. STM requires electron tunneling between tip and sample, so only conducting samples such as metals and semiconductors can be studied with STM. Sometimes a thin layer of insulating adsorbate on conducting surface can also be studied. STM is not only used to image the surface, but can also be used to study the electronic structures at the atomic scale using scanning tunneling spectroscopy (STS), and one can even perform atom or molecule manipulation by changing tip bias.

Later in 1986, Binnig, Quate and Gerber invented AFM[37], another type of SPM allowing imaging at atomic level resolution, which does not require conducting samples. AFM works by measuring tip-surface interactions. Depending on the separation between tip and surface, the interactions between tip and surface may be dominated by various types of forces. When the tip is very close to the surface, short-range interactions such as van der Waals forces are dominant, otherwise long-range interactions such as electric and magnetic forces become dominant. In AFM, a silicon or silicon nitride cantilever with a sharp tip at the end is used to probe the surface. Usually, a laser spot reflected from the back of the cantilever is used to measure the deflection due to the forces between tip and surface. There are two basic probing modes for AFM, contact mode (static) or non-contact mode (dynamic). In contact mode, the tip simply rasters across the surface, and the force between tip and surface is kept constant by adjusting the deflection of the cantilever. In non-contact mode, the cantilever is oscillating at high frequency while scanning. Forces between tip and surface will result in

a shift of resonant frequency, and the oscillation frequency or amplitude is maintained by moving the tip in the z direction.

2.3.2 Principles of STM

The key idea to STM is tunneling, which is a quantum mechanical phenomenon originated from the wave nature of particles. In classical mechanics, when an electron is incident onto a barrier with a potential energy greater than the kinetic energy of the electron, there is no chance that the electron can penetrate the barrier and appear on the other side of the barrier. However, quantum mechanics says there is a possibility that the electron can traverse the barrier under certain conditions. When two metals are brought together with a very small separation, and a voltage is imposed on the two metals, there will be electrons tunneling from the filled states of one metal to the empty states of the other metal. The tunneling current I_t decays exponentially with the barrier width, and reaches its maximum value when the two metals are touching. The energy diagram and tunneling process are shown in Fig. 2.1. The metal on the right in this figure is positively biased, and this bias lowers the Fermi level, which creates enough empty states for electrons to tunnel into. The tunneling mechanism also applies to other conducting solids, such as semiconductors. In STM experiments, the two conducting solids are the tip and the surface we are probing. The most commonly used STM tips are electrochemically etched W wire or mechanically sheared PtIr wire. The quality of the tip is crucial to the resolution of STM images. A very sharp tip with only one atom protruding at the end of the tip is required to obtain atomic resolution. The tunneling current, at a first order approximation, has the form of:

$$I_t(d,V_t) \propto \rho V_t \exp(-1.025d<\Phi>^{-1/2}) \qquad (2.1)$$

Where ρ is local density of states (LDOS) of tip and surface, d is the distance between the atom at the very end of tip and surface, V_t is tunnel voltage applied between tip and sample, $<\Phi>$ is average work function or tunnel barrier. We will know from this equation that the tunnel current I_t changes by an

order of magnitude when d changes just 1Å. This explains why the extremely high vertical resolution of 0.1Å can be achieved with STM.
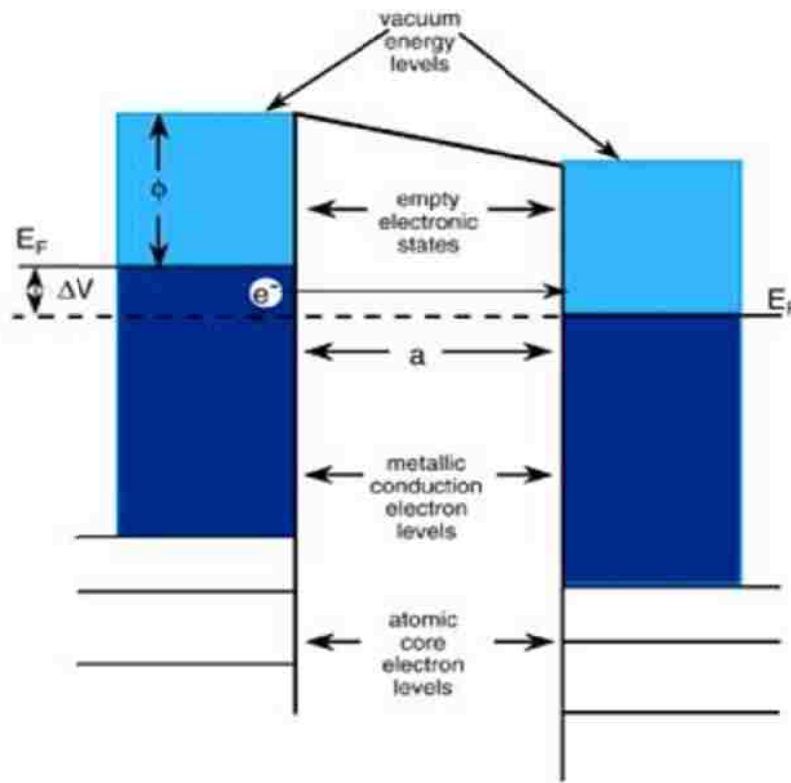

Fig. 2.1 Schematic for electrons tunneling through high energy barrier [38]

A typical setup of STM is shown in Fig. 2.2. There are two probing modes in STM, called constant current mode and constant height mode, and the most used probing mode is the constant current mode. In this mode, when the tip is scanning the surface which defines the x-y plane, a feedback loop adjusts the z-position of the tip by applying voltage to the piezoelectric tube in order to keep the tunneling current constant, the tip movements in x- and y- directions are realized by applying

voltages to two side electrodes on the piezoelectric tube. In this way, the z(x,y) profile can be mapped, in most cases, as contour of local density of states (LDOS) of the surface

2.3.3 Omicron VT STM XA

Two different STMs were used in this work, an Aarhus-Type STM and an Omicron VT STM XA. The details of Aarhus-Type STM have been thoroughly explained in the PhD thesis of our previous group members [39-42]. I will describe the Omicron VT STM XA here.

The Omicron VT STM XA is an UHV scanned probes microscope equipped with a Q-Plus sensor for AFM, and it operates in a variable temperature range from 50K to 650K. The STM is housed in a dedicated Omicron UHV chamber, which is mounted to our preparation chamber.
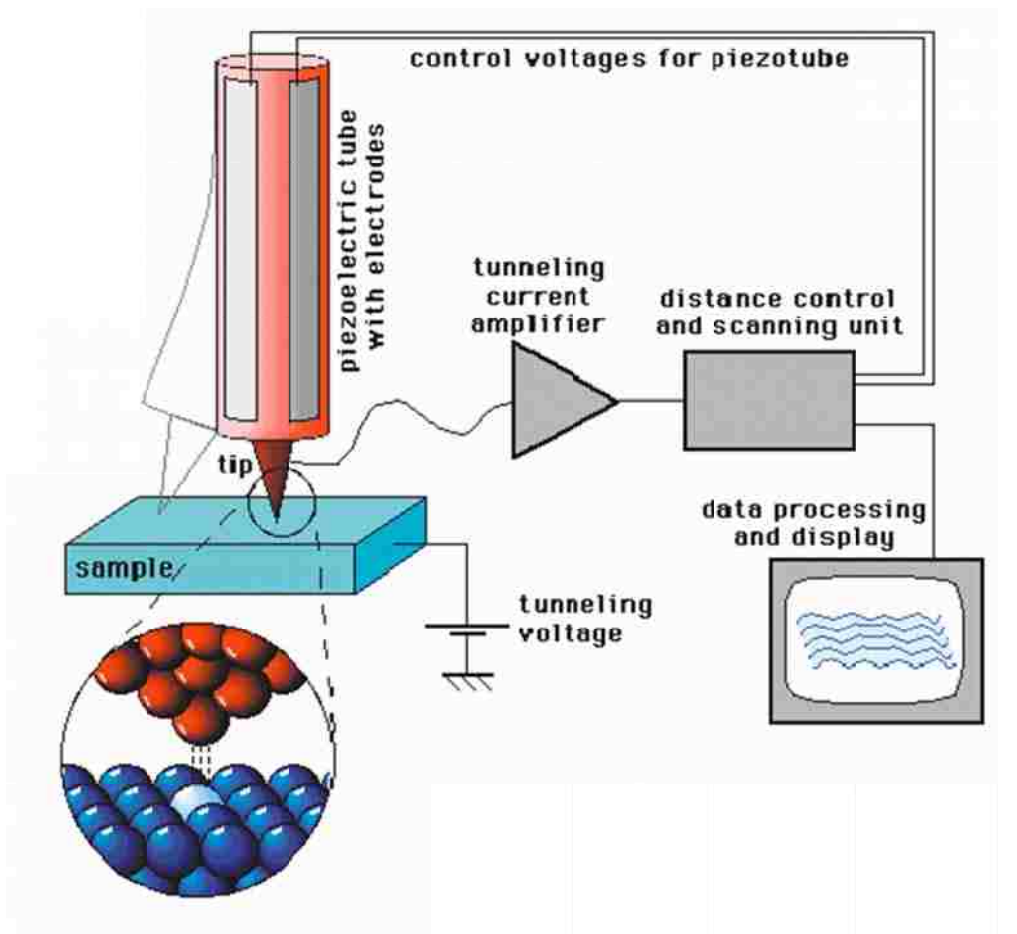

Fig. 2.2 Schematic of a typical STM setup [43]

A sample carousel with twelve slots can be mounted in the dedicated STM chamber allowing storage of up to twelve samples/tips. A side view of the Omicron VT STM XA is shown in Fig. 2.3. The STM scanner, damping stage, cooling feedthrough, and electronic feedthroughs are integrated on a 10 inch OD Conflat flange, which is bolted onto the STM chamber. The STM base plate is suspended by four soft springs with resonance frequency of 2Hz. Vibrations of the suspension system are damped using a magnetic eddy current damping mechanism.
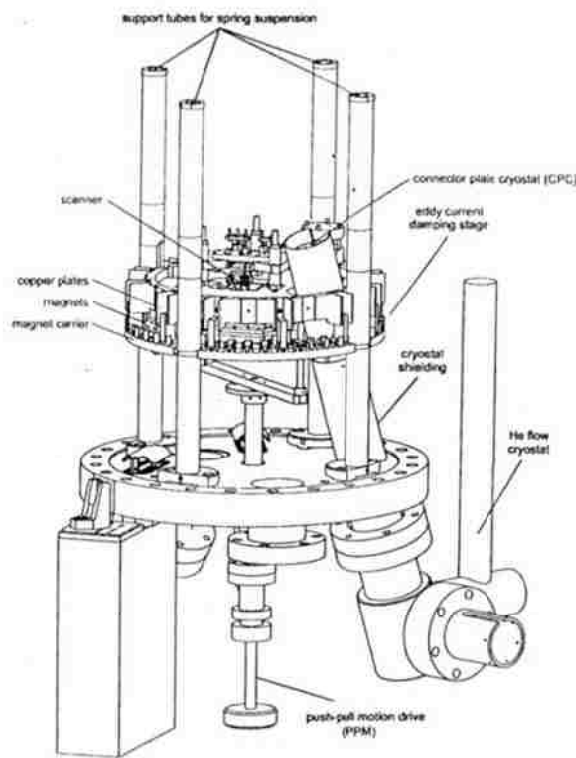

Fig. 2.3 Side view of the Omicron VT STM [44]

The eddy current damping mechanism of the STM plate is accomplished by a series of copper plates which sit between permanent magnets as shown in Fig. 2.3. A push-pull motion drive installed right under the STM plate is used to lock the damping stage, which allows tip/sample transfer. Tip/sample transfer in the chamber is performed with a pincer grip wobble stick. For tip transfer, the

STM tip is mounted onto a tip holder and the tip holder is loaded into the vacuum chamber. In the chamber, tip holder is placed on the sample stage of the STM, where the tip is mounted onto the top of the piezo tube. Then the empty tip holder is moved to the sample carousel for later tip transfer use.
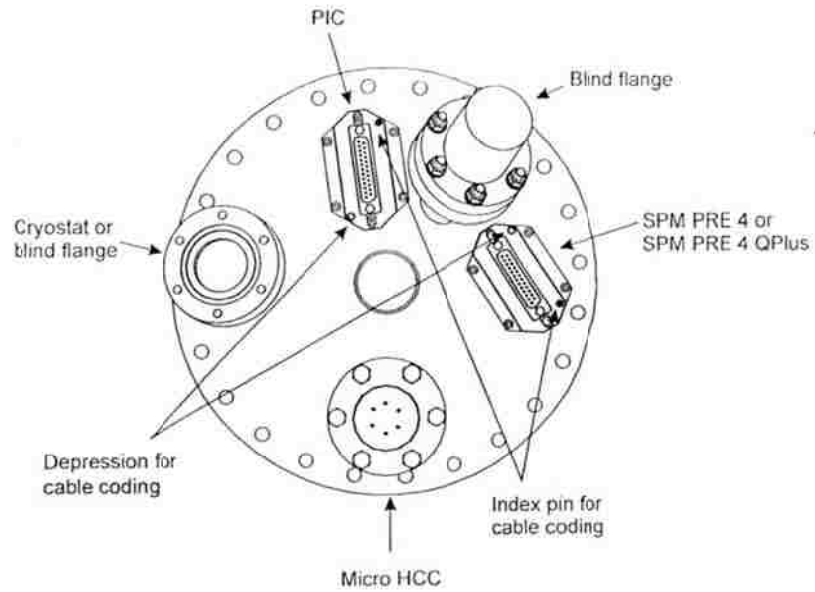

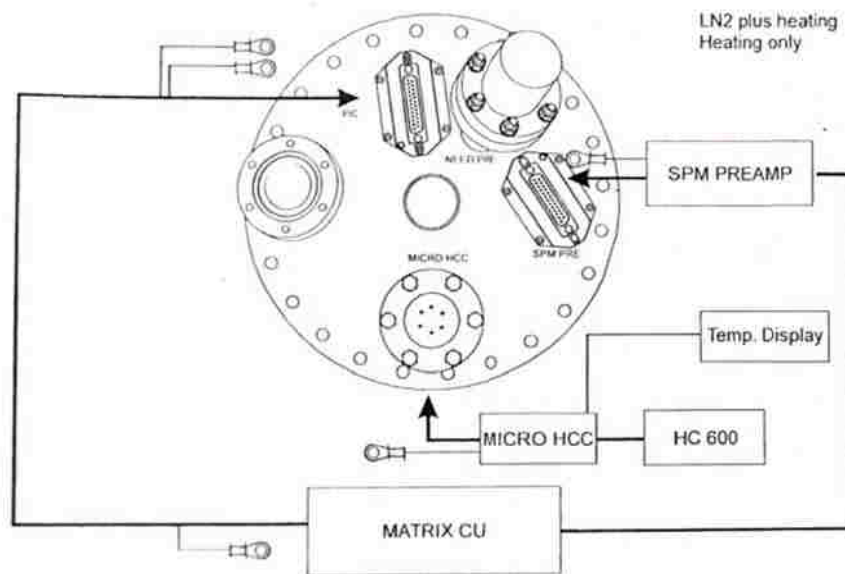Fig. 2.4 Layout of the base flange [44]

Fig. 2.5 Wiring diagram [44]

The layout of the base Conflat flange on the atmospheric side and the diagram of wiring from base flange to the matrix electronics control unit (CU) are shown in Fig. 2.4 and Fig. 2.5 respectively. The tunnel-current signal is amplified using a preamp box, which is directly mounted to the atmospheric side of the base flange through the 25-pin D-sub connector SPM PRE 4, and by doing this, electronic noise can be minimized. The 25-pin D-sub PIC connector is used for connection of the piezo scanner tube and coarse approach motors to the electronics. Fig. 2.6 shows the scanner tube with a tip mounted. A magnet on top of the scanner tube is used to mount STM tip. In this STM, the sample is placed with surface facing down, and the tip is advanced upward to reach the surface. The tip approach is accomplished in two steps. In the first step, the coarse approach brings the tip very close to the surface, and this process is monitored with a CCD camera mounted on a 2 ¾ inch window. When the tip gets close to the surface, for most samples, we will be able to see the real tip and the reflected image of the tip from the surface of the sample. These two tip ends meet when the tip reaches the surface, and we stop the manual coarse approach before that happens. In the tip approach process, one must be very careful and reduce the approaching speed when the tip is close to surface in order to avoid a tip crash. After the coarse approach, an automatic fine approach is used to bring the tip to the surface for scanning and stops automatically when a tunnel current is detected. The scanner tube allows a maximum scan range of about 12µm×12 µm and z-direction movement of about 1.5µm.

As stated above, the VT STM XA can be operated at either elevated temperature or reduced temperature. The sample is heated through a heater element integrated in the sample stage, which is shown in Fig. 2.7. Samples are heated using a low noise power supply HC600, which is connected to the Micro HCC connector on the base flange as shown in Fig. 2.5. Cooling of the sample can be realized by either a LN_2 bath cryostat or a LHe flow cryostat. For cooling with the LN_2 bath, additional pumping can be added to further lower the sample temperature by freezing the LN_2. The sample temperature is measured with either K-type NiCr/Ni thermocouple (for LN_2) or PT-100 sensor (for LHe).
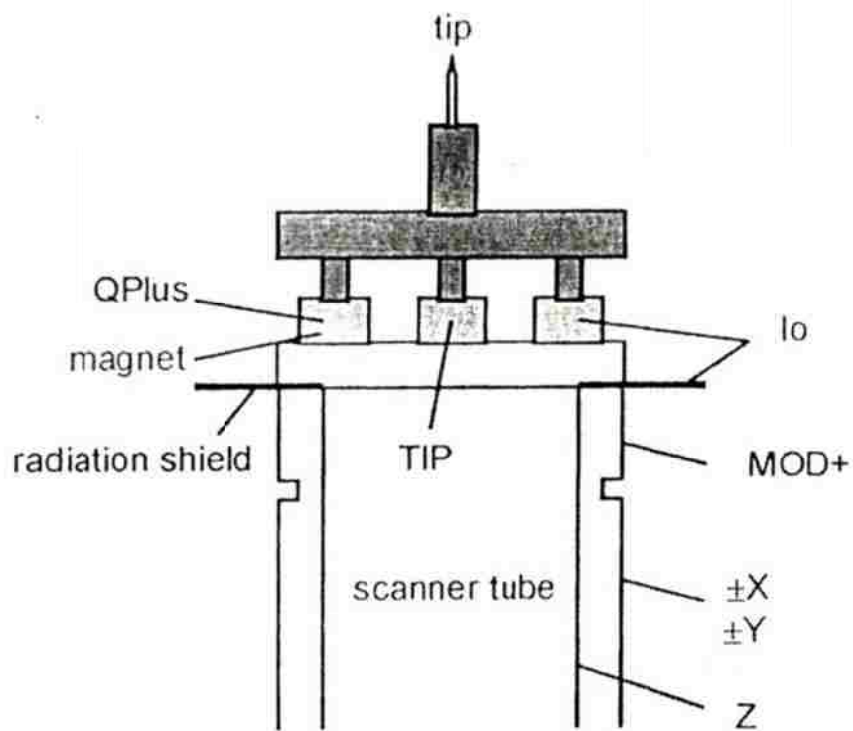
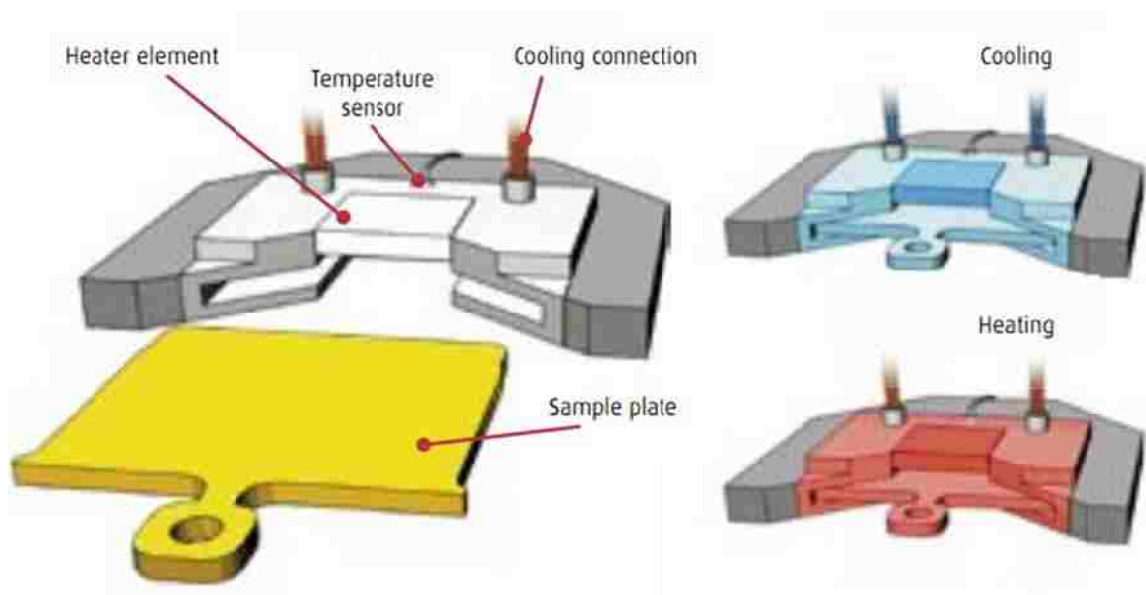Fig. 2.6 Scanner tube with STM tip mounted [44]

Fig. 2.7 Illustration of sample heating and cooling [45]

2.4 High Resolution Electron Energy Loss Spectroscopy (HREELS)

2.4.1 Introduction to HREELS

High Resolution Electron Energy Loss Spectroscopy (HREELS) is one of the most useful tools in surface analysis. It has the ability to study a variety of physical and chemical properties of surface and adsorbates, such as surface phonons, electronic transitions, bonding sites of adsorbates, and adsorbate vibrational modes. When a monochromatic electron beam is incident on the sample, the electrons will undergo elastic and inelastic scattering within the sample. The loss energy due to inelastic scattering will excite vibrational modes or electronic transitions, and the kinetic energy of the scattered electrons will be measured at a given direction. The primary electron beam energy used in HREELS ranges from a few eV to a few tens of eV, and the inelastic mean free path of electrons within this energy range is in the order of a few Å, which implies that HREELS is an extreme surface sensitive analysis tool. The energy loss measured in HREELS is from a few meV to a few eV, allowing us to obtain information about the excitation of vibrational modes, electronic transitions or plasmon resonances.

2.4.2 LK2000 High Resolution Electron Energy Loss Spectrometer

In this work, EELS spectra were measured using an LK2000 High Resolution Electron Energy Loss Spectrometer. This spectrometer provides a primary electron beam with energies ranging from 1 to 240eV, and a resolution below 5meV. The EELS spectrometer is housed in a UHV chamber and operated under UHV conditions. The structure of LK2000 EELS spectrometer is shown in Fig. 2.8. The spectrometer consists of an electron gun, two monochomators, an analyzer with a channeltron, and a lens system. The sample position shown in the figure is the "standard position" in our experiment. At this position, the incident angle θ_{inc} is 30˚. The sample can be rotated to change θ_{inc}. The analyzer can also be rotated, and the rotation range for θ_{an} is 13˚ -68˚. In this way, either specular or off specular scattered electrons can be measured.
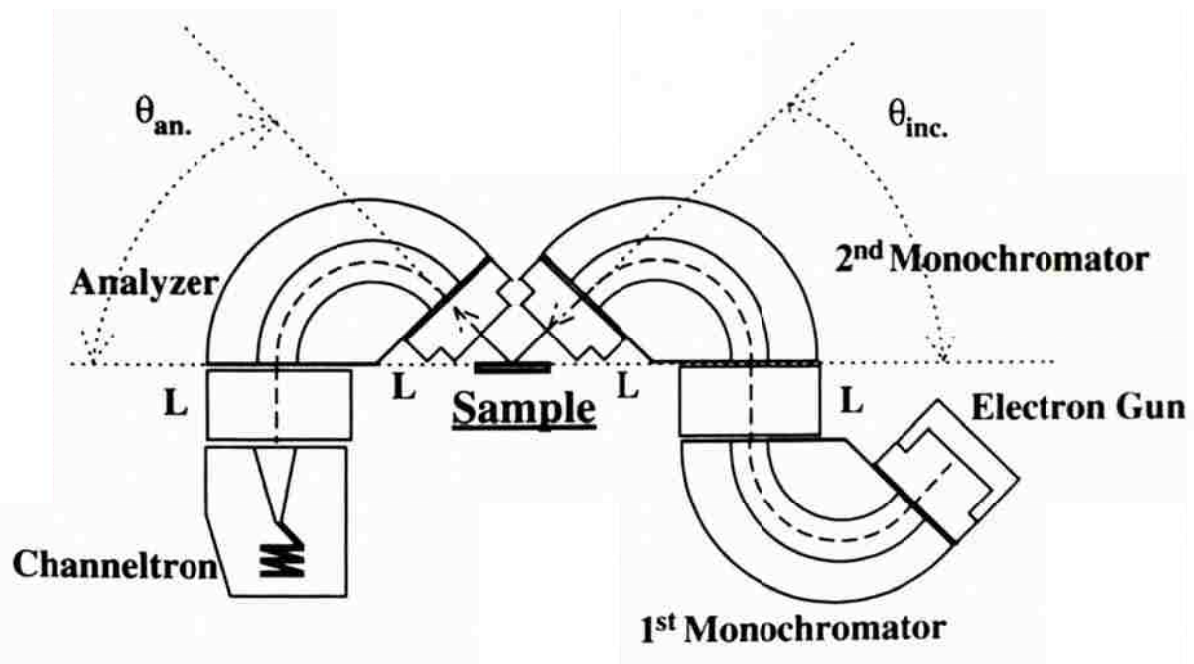
Fig. 2.8 Schematic diagram of LK2000 spectrometer [46]

The incident electron beam is produced from the electron gun. The beam exhibits a Maxwellian energy distribution with FWHM given by:

$$\Delta E_k = 2.54\ k_B\,T \tag{2.2}$$

where k_B is Boltzmann constant (11600^{-1} eV·K^{-1}) and T is the filament temperature in K. From this equation, the energy resolution for the electron beam is on the order of a few tenths of eV. To achieve energy resolution of a few meV, two stages of 127˚-sector monochromators are employed to produce a collimated and highly monoenergetic electron beam. The scattered electrons from the surface enter into focusing lens system and then are guided to the analyzer. The analyzer used in LK2000 is the Electrostatic Cylinder Sector Energy Analyzer type (Fig. 2.9). The lens system following the analyzer focuses the electron beam into a channeltron electron multiplier working at 2900V, and the count rate is recorded. A complete pathway of electron beam travelling in LK2000 spectrometer is shown in Fig. 2.10.
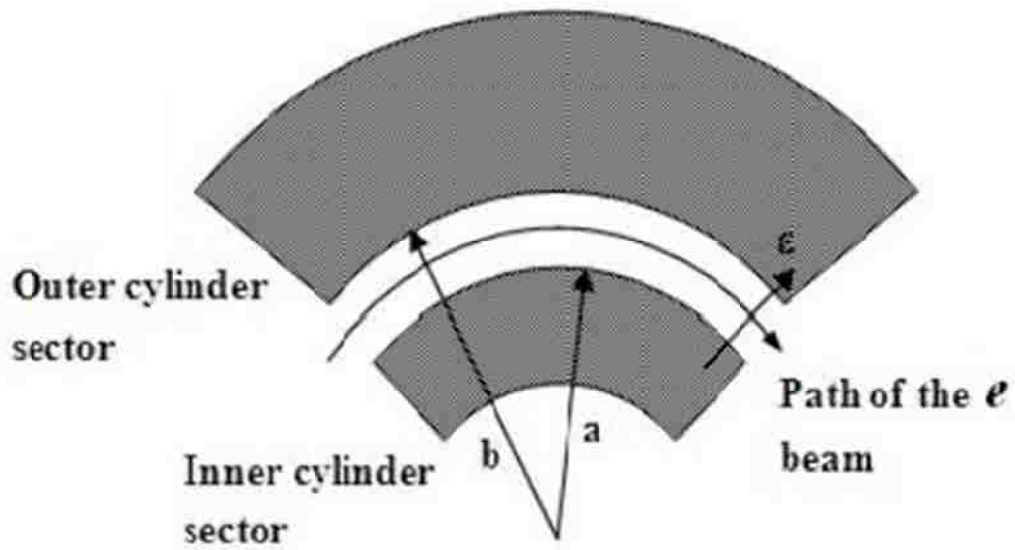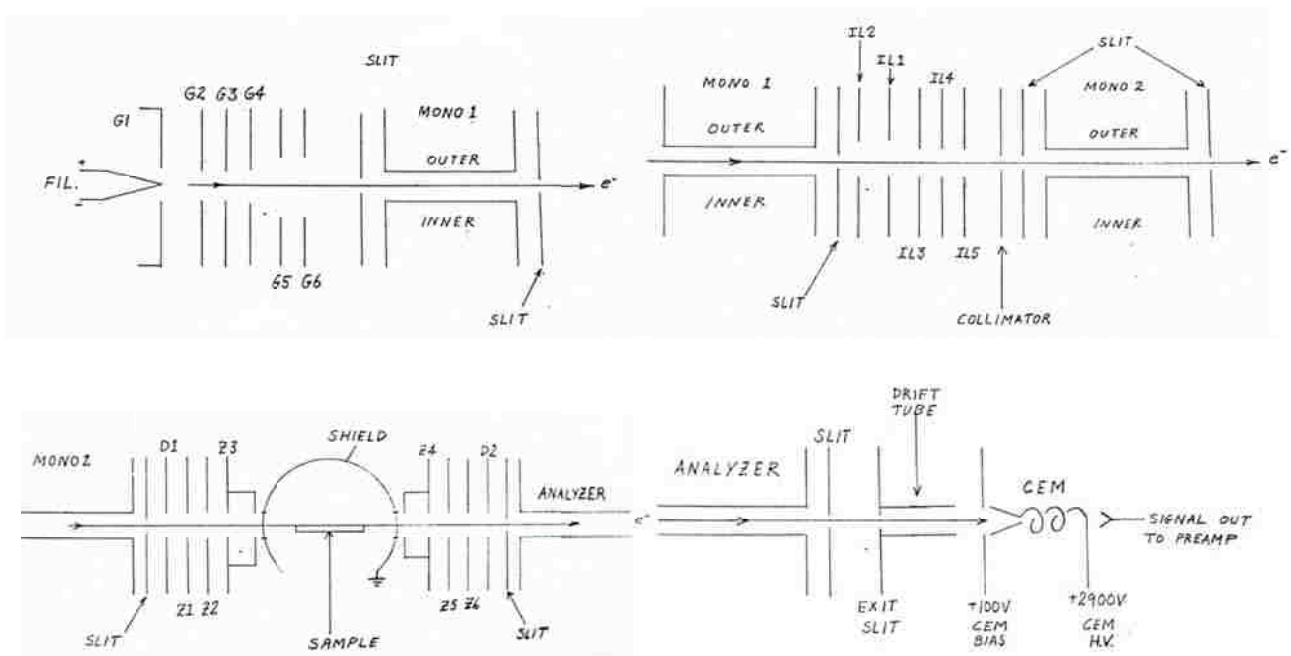
19

Fig. 2.9 Cylindrical Energy Analyzer [46]

Fig. 2.10 Complete pathway of electrons in LK2000 EELS spectrometer [46]

20

2.5 Photoelectron Spectroscopy (PES)

2.5.1 Principle of Photoelectron Spectroscopy

Photoelectron Spectroscopy (PES) techniques are based on the photoelectric effect, first discovered by Henrich Hertz in 1887 [47], and later explained by Albert Einstein in 1905 [48]. Einstein utilized Plank's quantum energy concept to explain that frequency, not the intensity is the key for light to eject electrons from a metal. PES has the ability to measure both the kinetic energy and the momentum distributions of the ejected electrons, and is an invaluable tool to reveal the electronic, magnetic and chemical structures of materials.

According to Einstein's explanation, when a quantum of light with certain energy $h\nu$ is incident onto a material, an electron can escape from the material's surface. The maximum kinetic energy of the electron can be written as:

$$E_{kin} = h\nu - \Phi \tag{2.3}$$

where Φ is the work function of the surface which is the energy needed to remove an electron from Fermi level (E_F) to vacuum, h is Plank's constant, and ν is the frequency of the incident light. Fig. 2.11 illustrates the photoemission process and how the energy levels of the sample can be explained by the measured photoemission spectrum. The absorbed incident photon of energy $h\nu$ excites an electron from either valence bands or core-levels at energy level E_B below E_F to unoccupied energy levels above E_F. The binding energy of the electron can be calculated by:

$$E_{kin} = h\nu - \Phi - |E_B| \tag{2.4}$$

The energy of the incident photon and the work function of the material are known, the kinetic energy of the electron is measured, and so the binding energy $|E_B|$ of the electron can be obtained. In this work, all the photoemission spectra are taken from normal emission, so only energy measurement is involved. However, PES is especially powerful in mapping the electronic structures of the material in k space, which is called angle resolved photoemission spectroscopy (ARPES). A schematic of the ARPES

21

experiment setup is shown in Fig. 2.12. The photons coming out from the light source shines on the

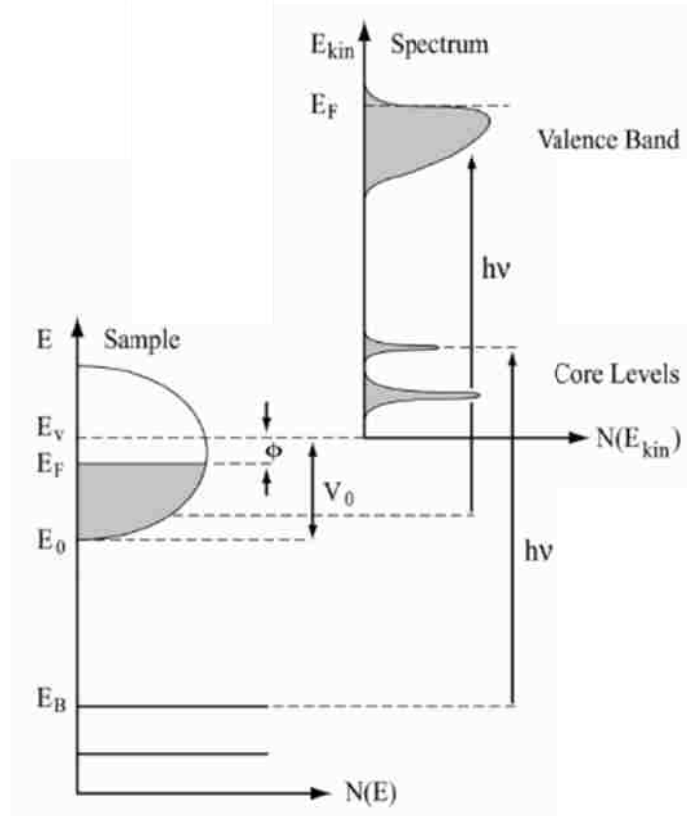sample, then electrons are kicked out and collected by the electron analyzer.

Fig. 2.11 Energy diagram of photoemission process, relationship between electron density of states of the material (left) and energy distribution of the measured photoemission spectrum (right) [49]
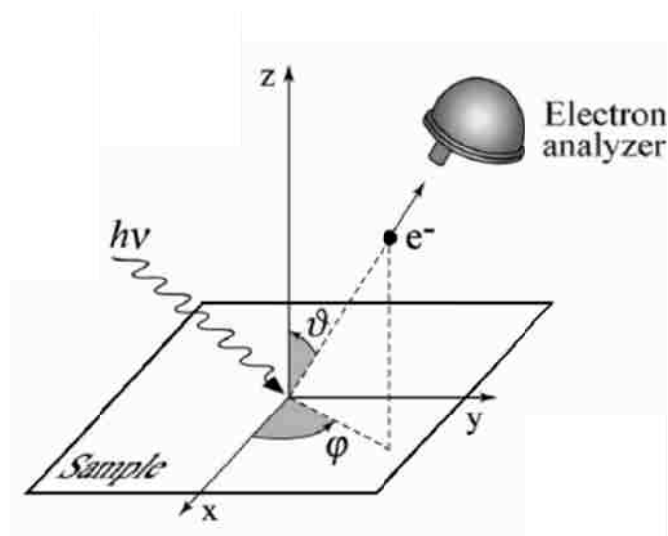

Fig. 2.12 Schematic of geometry of ARPES experiment [50]

We already have the energy conservation relation in (2.4). The photoemitted electron's momentum component parallel to the surface is conserved, while the momentum component perpendicular to the surface is not conserved due to the surface potential barrier. The momentum of the photon is typically negligible, so the momentum of photo-excited electron roughly represents the crystal momentum. The wave vector of the electron is determined by:

$$k = \frac{p}{\hbar} = \frac{1}{\hbar}\sqrt{2mE_{kin}} \tag{2.5}$$

$$k_{\parallel} = \frac{1}{\hbar}\sqrt{2mE_{kin}}\sin\vartheta \tag{2.6}$$

$$k_x = \frac{1}{\hbar}\sqrt{2mE_{kin}}\sin\vartheta \cdot \cos\varphi, \quad k_y = \frac{1}{\hbar}\sqrt{2mE_{kin}}\sin\vartheta \cdot \sin\varphi \tag{2.7}$$

and
$$\Delta k_{\parallel} = \frac{1}{\hbar}\sqrt{2mE_{kin}}\cos\vartheta \cdot \Delta\vartheta \tag{2.8}$$

One has to be aware that the ARPES typically applies to ultraviolet light with photon energies less than 100eV, which in part determines the k resolution of the photoelectrons. From (2.8), we can estimate the value of $\Delta k_{\parallel}$ for electrons excited near the Fermi level. The angular acceptance $\Delta\vartheta$ is usually ~2°, if X-ray source with energy of ~1000eV is chose, then $\Delta k_{\parallel}$ is calculated to be ~0.5Å^{-1}, which is comparable to the Brillouin zone wave vector for many single crystals. Because of this, low photon energy (below 100eV) is crucial to ARPES measurements. For different materials, the electron escape depth follows a "universal" curve (Fig. 2.13). For photon energies between 20-200eV, the electron escape depth is less than 10Å, indicating that the PES data carries information from the top few atomic layers on the surface.

The three-step model is usually used to describe the photoemission process [49, 51-54], which is illustrated in Fig. 2.14. According to the three-step model, the photoemission process is separated into three independent parts: 1) Optical excitation of an electron from the initial state i to a final state f

within the crystal. Because of the momentum conservation, only direct transitions are allowed in the reduced zone scheme.
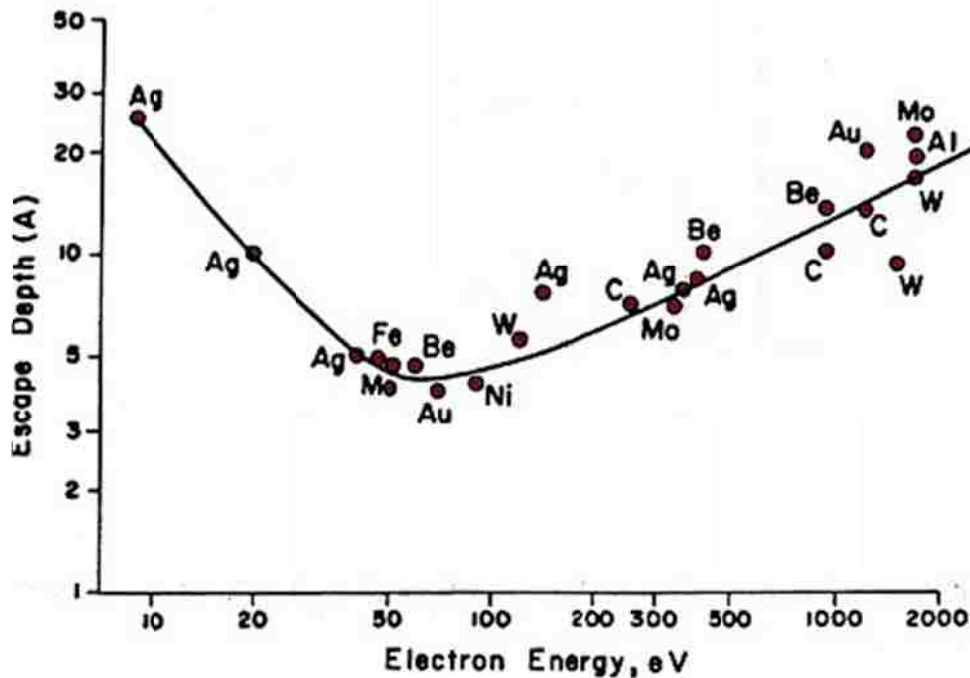
Fig. 2.13 "Universal curve" of electron escape depth as a function of kinetic energy [55, 56]

The transition probability can be described by Fermi's golden rule. 2) Propagation of the excited electron from the excitation site to the surface. In this process, the transport probability is governed by the mean free path of the excited electrons. Photons with energy of a few hundred eV can penetrate as deep as several hundred Å into the crystal. But as mentioned above, the escape depth of photoelectrons is only a few Å, which implies that only the photoelectrons near the surface region can propagate to the surface without suffering inelastic losses due to electron-electron interactions. 3) Escape of the electron into vacuum. The escape probability here is dependent on the electron kinetic energy and work function of the sample. In this process, momentum parallel to the surface is conserved, so the internal wave vector parallel to the surface can be obtained.
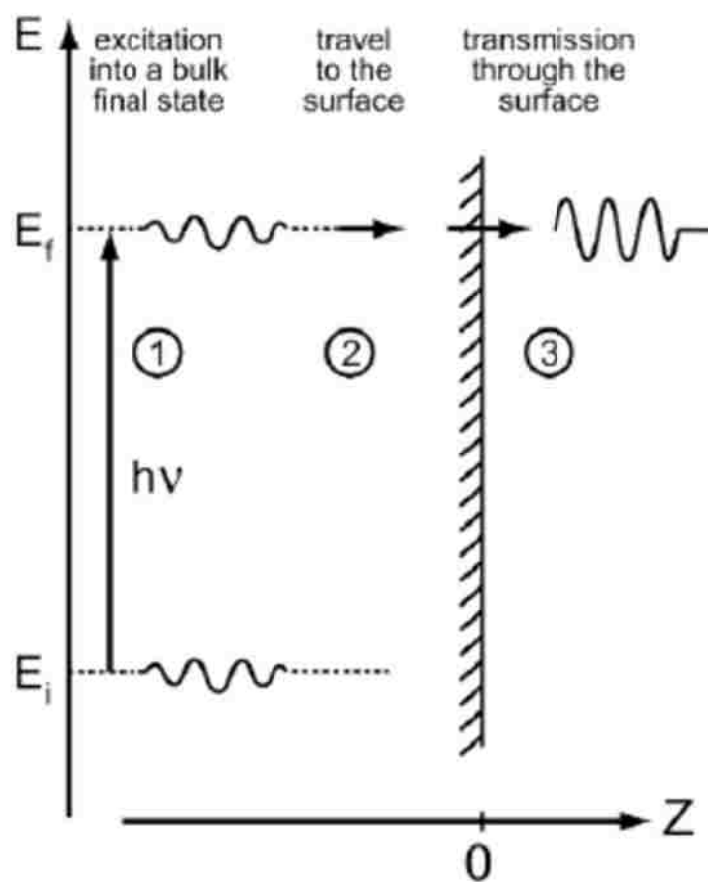
Fig. 2.14 Three-step model of photoemission process [49]

2.5.2 6m-TGM Beamline in CAMD

The photoemission data in this work were all taken on an endstation at the 6-meter Toroidal Grating Monochromator (6m-TGM) beamline of CAMD. CAMD is the acronym for Center for Advanced Microstructures and Devices, which is a synchrotron radiation based research center owned by Louisiana State University.

The top view of the CAMD storage ring, beamlines, and clean rooms arrangement is illustrated in Fig. 2.15. Both bending magnets (1.48Tesla) and a superconducting wiggler (7Tesla) are employed to create synchrotron radiation using electron beam energy of 1.3GeV and beam currents of typically 200mA (Fig. 2.16).
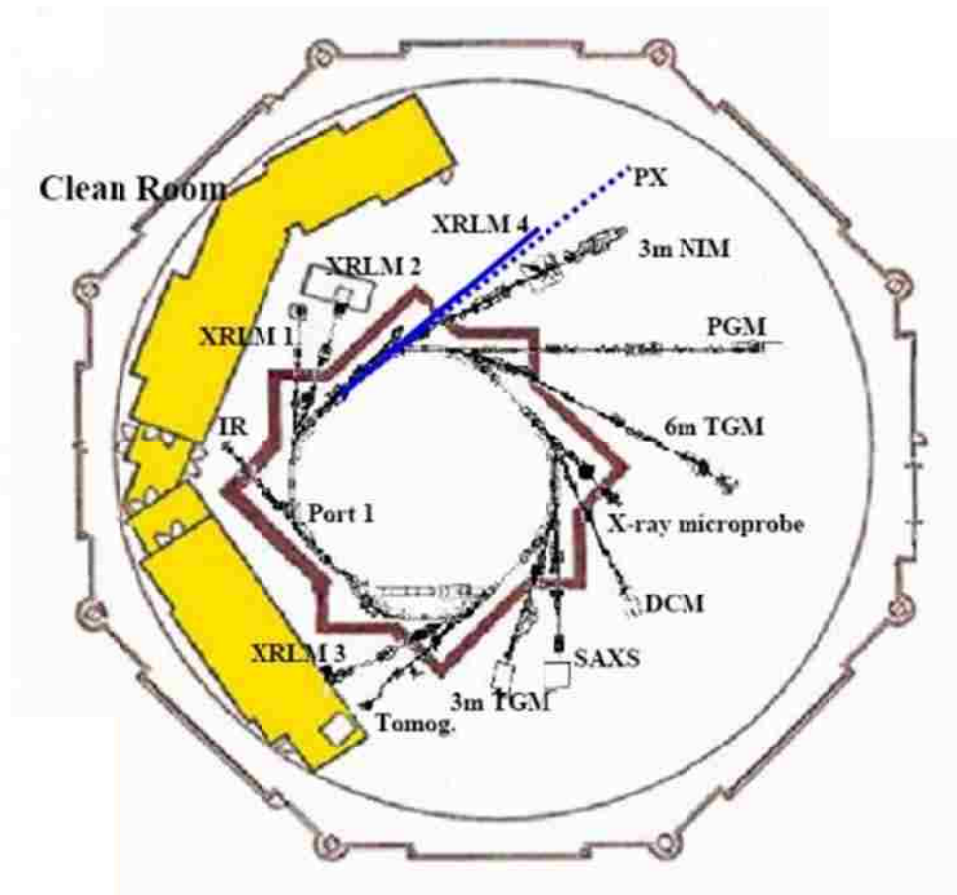
Fig. 2.15 Top view of CAMD storage ring and beamlines [57]

Compared to lab based UV lamps or X-ray sources, the major advantages of synchrotron radiation are the high flux and continuous light spectrum from infrared, to ultraviolet, to soft X-rays, and to hard X-rays. The 6m-TGM beamline we worked on provides photon energy of 15-200eV with resolving power (E/ΔE) better than 2000. As shown in Fig. 2.17, there are three optional gratings (LEG, MEG, HEG) in 6m-TGM beamline. By switching between those gratings, we can obtain different photon energy range for experiments. The 6m-TGM was equipped with a Specs Phoibos 150mm hemispherical analyzer and a side chamber used for sample preparation and evaluation using low energy electron diffraction (LEED).

26

Fig. 2.16 Flux curve for bending magnets and superconducting wiggler [57]

Fig. 2.17 Measured photon flux curves vs. photon energy for 6m-TGM [57]

27

2.6 Other Surface Analysis Techniques

Although STM, EELS, and PES are the main tools for taking data in this work, other surface analysis techniques are frequently used during the course of experiments. The most important ones are Auger Electron Spectroscopy (AES) and Low Electron Energy Diffraction (LEED).

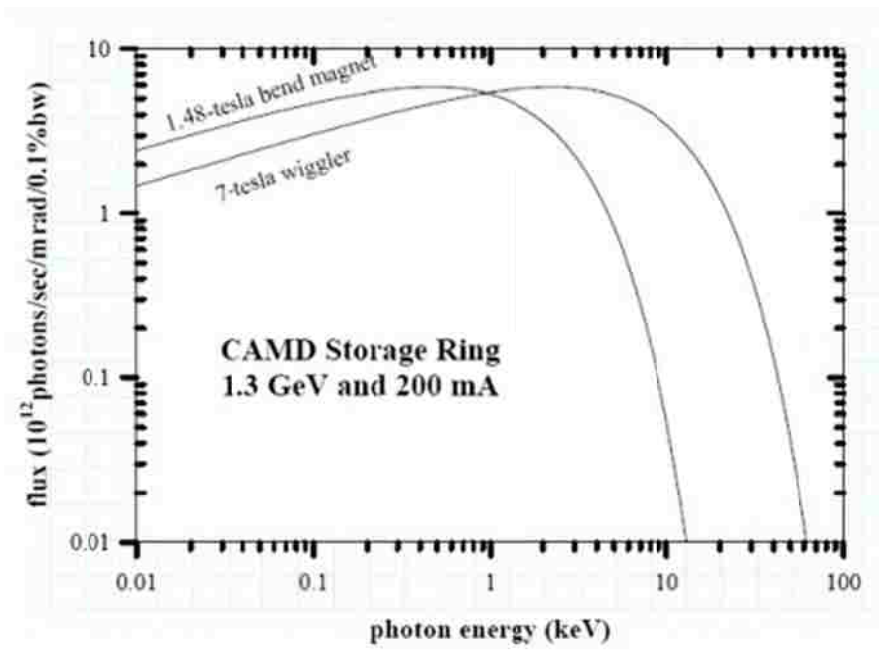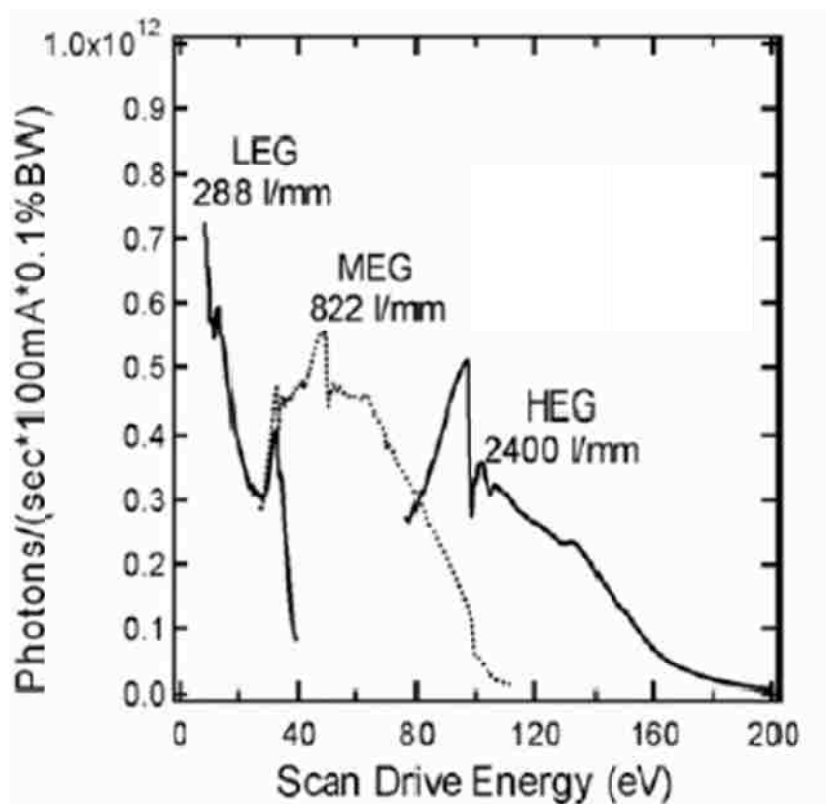### 2.6.1 Auger Electron Spectroscopy (AES)

Auger electron spectroscopy can be used to study the chemical composition of sample surfaces under UHV conditions in a very similar way to X-ray photoemission. AES is based on the Auger effect, which was discovered by Pierre Auger in 1923. In X-ray photoemission experiments, there are found to be some electrons emitted whose kinetic energy is independent of the incident photon energy, and they are Auger electrons.

When a high energy electron beam impinges on a sample, an electron in a core level (K or L shell) can be removed with a hole left at that level. An electron at a higher energy level (first outer shell) may fall into that core hole but to do so it must release some energy. Sometimes the energy may be released in the form of photon emission, but it may also be transferred to another electron (second outer shell) which then is ejected from the atom, leaving the atom with two holes in a shallower state. The emitted electron is an Auger electron. Both emitted X-ray photons and Auger electrons carry characteristic energy of this atom, and can be used for chemical composition analysis. The X-ray emission is the basis of Energy Dispersive X-ray Spectroscopy (EDX or EDS), which is a widely used chemical composition analysis technique. Compared to the photon, electron has a much smaller mean free path, so Auger electron spectroscopy is more surface sensitive, and is commonly used for chemical analysis in surface science. The kinetic energy of Auger electron is determined as follows:

$$E_{Auger} = E_A - E_B - E_C \tag{2.9}$$

where the E_A, E_B, E_C are the energy levels of core shell, first outer shell and second outer shell respectively, measured from vacuum level. Because Auger transitions involve three electrons, AES can

be applied to all the elements except H and He. There are a variety of transition pathways for filling the core hole, and some of them are shown in Fig. 2.18. Of all those transitions, KLL and LMM transitions are the most observed in AES experiments. Fig. 2.19 plots the position of Auger lines versus the atomic number of element.

The Auger electron spectroscopy system consists of an ultra-high vacuum system, an electron gun for excitation and an energy analyzer for detection. A typical AES experiment setup is shown in Fig. 2.20. The Auger peaks are usually measured by differentiating the energy distribution function N(E) because of the large continuous background, thus the Auger spectrum is the function $\dfrac{dN(E)}{dE}$. The peak-to-peak magnitude of an Auger peak in the spectrum is related to the surface concentration of each element, so AES can also be used in quantitative analysis.
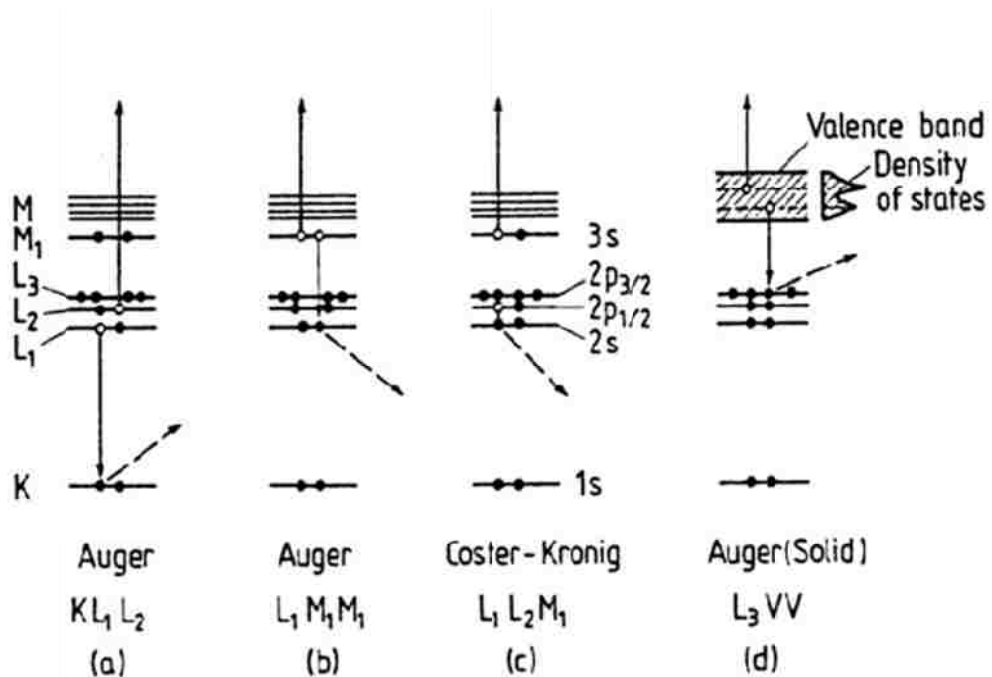

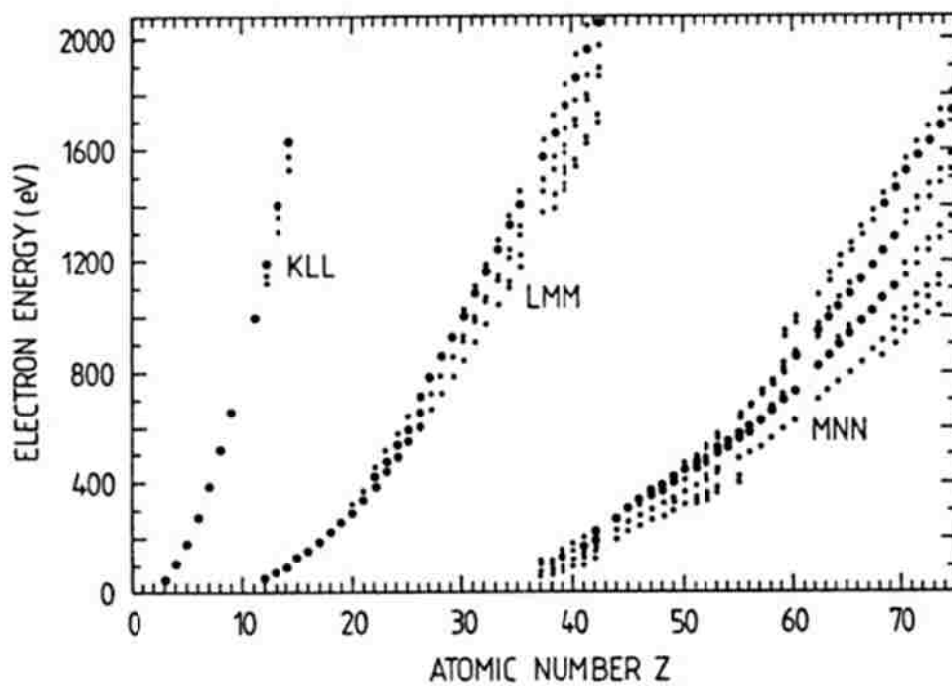Fig. 2.18 Examples of Auger transition [58]

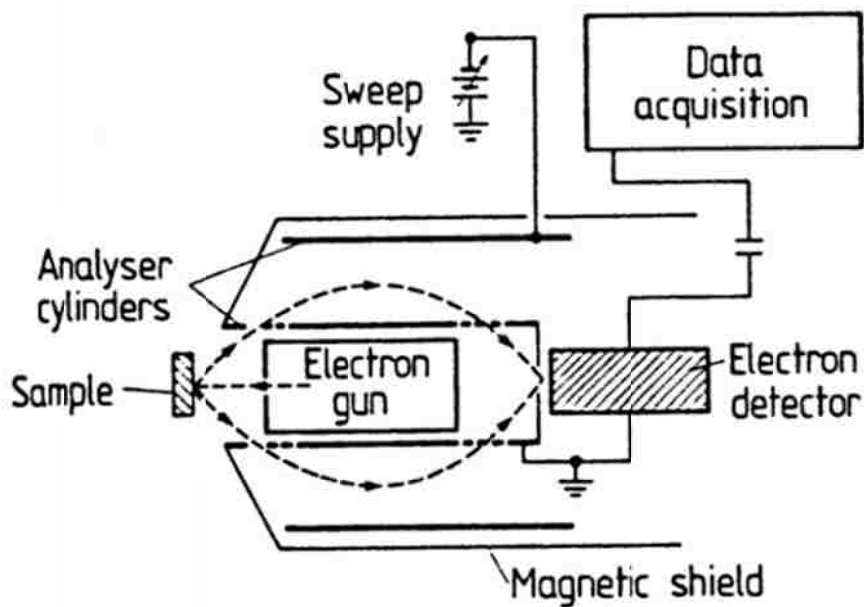Fig. 2.19 Position of Auger lines vs. atomic number [58]

Fig. 2.20 AES experiment setup [58]

The sensitivity of AES is determined by the transition probability of the Auger transition, the electron beam energy and current, and the analyzer collection efficiency. In this work, the electron gun can provide an electron beam at 3kV energy and 50μA current. A high sensitivity cylindrical mirror analyzer (CMA) is used to collect electrons.

2.6.2 Low Energy Electron Diffraction (LEED)

Low Energy Electron Diffraction (LEED) and X-Ray Diffraction (XRD) are commonly used techniques to determine the crystal structures. Due to the short mean free path of electron within the crystal, LEED is surface sensitive and can be used to obtain long range surface structure information. The basis of LEED is the wave nature of electrons. The de Broglie wavelength of electron can be determined by:

$$\lambda = h / p = h / \sqrt{2mE} \tag{2.10}$$

where λ is the electron wavelength, h is Planck's constant, p is electron momentum, m is electron mass, E is electron kinetic energy. By plugging in the constant h and m, we will obtain:

$$\lambda = \sqrt{150.4 / E} \tag{2.11}$$

In (2.11), the units of E and λ are eV and Å respectively. The electron energy typically used in LEED experiment is in the range of ~30-500eV, so the wavelength is on the same scale of typical interatomic distance in crystals and thus diffraction is expected.

There are two major applications for LEED. The basic function of LEED is to check the long range surface structure and crystalline quality. The LEED pattern will directly show the symmetry and periodicity of the surface or the reconstructed surface. Fig. 2.21 gives an example of a LEED pattern. The image on the left is the $TiO_2(110)$ (1×1) pattern, while image on the right shows the (1×2) reconstruction of the $TiO_2(110)$ surface. LEED pattern of a clean and flat surface should consist of very sharp spots and dark background. Comparing the two LEED patterns, the left one has a much brighter background, which means the surface is not as perfect as the right one. In LEED experiments,

the pattern will "shrink" as we increase the incident beam energy, so the pattern on the left was taken at higher beam energy than the one on right one. The most important information obtained here is that the periodicity of the (1×2) surface pattern doubles compared to the (1×1) pattern. One has to note that the spots on LEED pattern represent k space reciprocal lattice rather than the real space lattice.
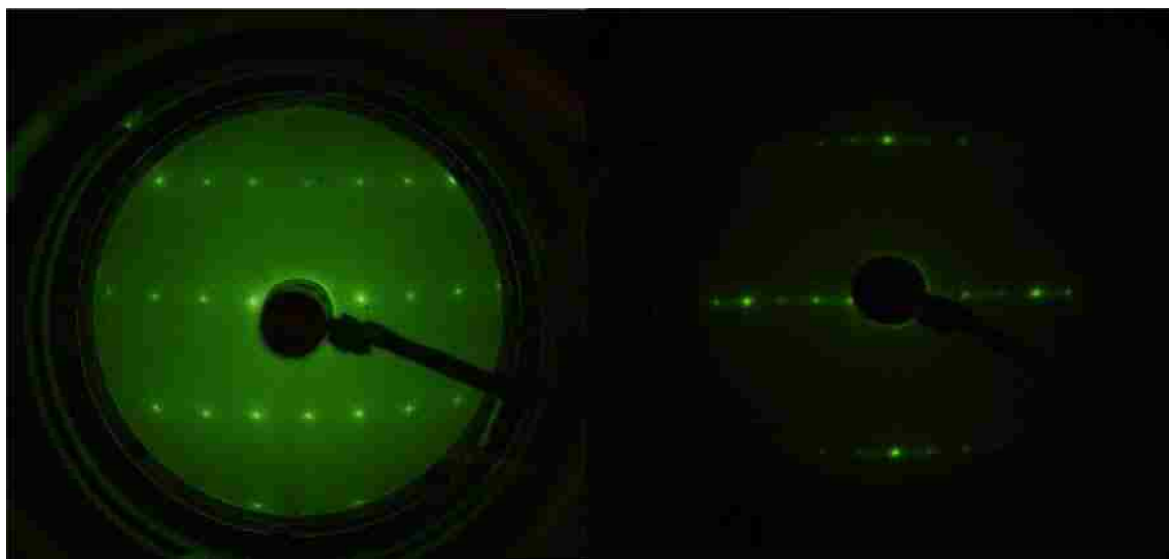
Fig. 2.21 LEED pattern of TiO_2(110) (1×1) (left) and (1×2) (right)

The other application of LEED is quantitative surface structure determination, which is more difficult. The brightness of every diffraction spot changes with incident electron beam energy. The intensities of the spots can be measured as a function of beam energy, providing LEED I-V curves. These curves can be predicted and they are highly sensitive to the chosen model of the surface structure and atomic spacings and the calculated model has to be adjusted to match the experiment results.

A typical LEED apparatus is shown in Fig. 2.22. The electrons produced from electron gun are accelerated and focused before they hit the surface. The scattered electrons from the sample will pass four grids and reach the fluorescent screen. The outer two grids (first and fourth) are grounded as is the

sample, which provides a field free region between sample and grids. The inner two grids (second and third) are negatively biased at a potential called retarding voltage slightly lower than the kinetic energy of the electrons. This retarding voltage repels all the inelastically scattered electrons. The elastically scattered electrons pass all the grids and are accelerated to the screen which is positively biased at ~5keV. The electrons arriving at the screen will stimulate fluorescence and can be directly seen through a window.

In this work, a Specs reverse view LEED system (Fig. 2.23) has been used. This LEED system consists of ErLEED 150 reverse view LEED optics and ErLEED 1000A power supply. The LEED optics is mounted onto the vacuum chamber through an 8 inch conflat flange. The whole optics can be extended or retracted up to 100mm in the chamber. The e-beam power supply provides electron beams with energies up to 1000eV.
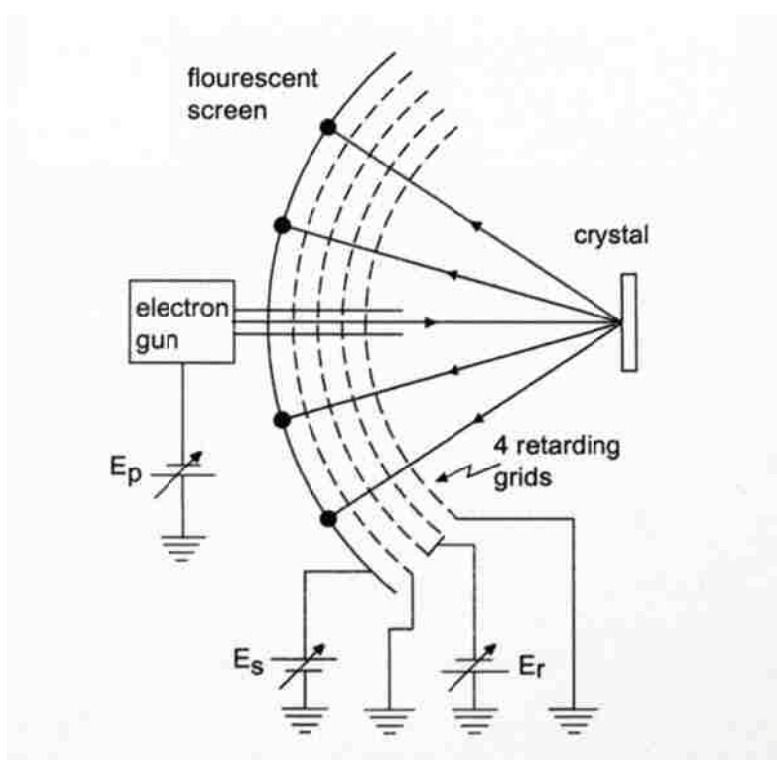
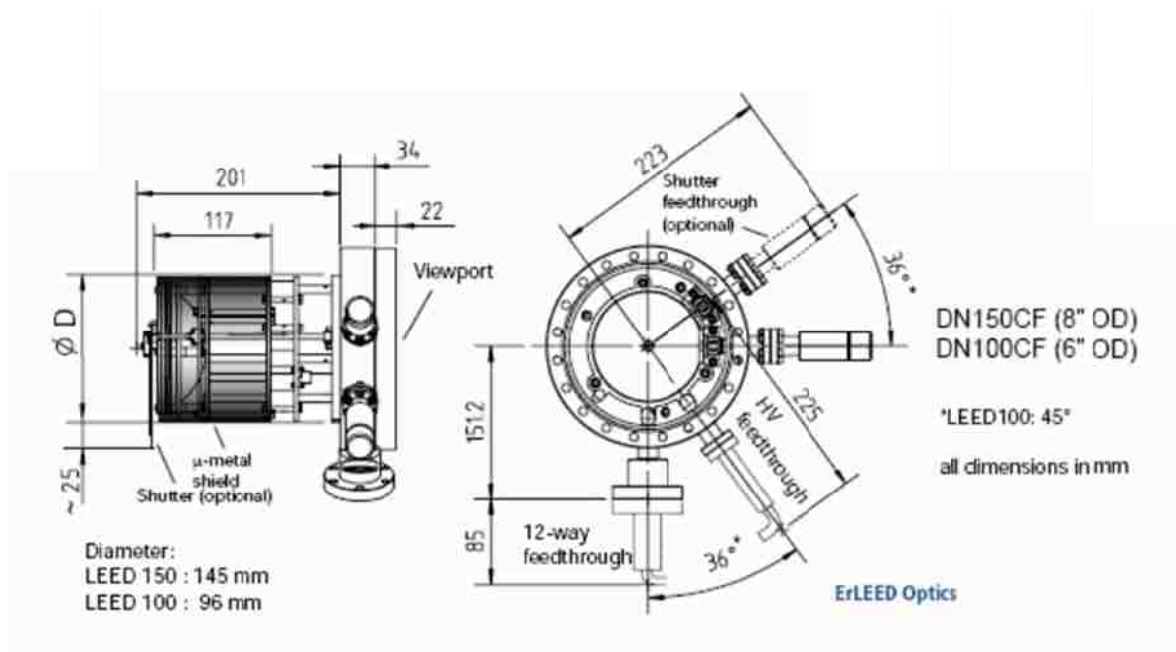Fig. 2.22 Schematic of LEED system [58]

33

Fig. 2.23 Schematic of Specs reverse view LEED optics (From ErLEED 100/150 Brochure)

Chapter 3: Silver Growth on r- and o- TiO$_2$(110) Surface

3.1 Introduction

Supported metal nanoclusters on oxides have received substantial attention recently because of their important applications in various areas, such as photovoltaic devices, photocatalysis, heterogeneous catalysis, and solar cells [8, 59-61]. Due to its much lower cost than other noble metals such as Au, Pt, Pd and Rh, Ag is a potentially active candidate for new industrial based catalytic applications. Although a noble metal like Au, it has been shown over the last decade that these metal-monolayer, -bilayer, and -cluster based supported systems demonstrate enhanced reactivity and selectivity of various reaction [62-64]. In the case of Ag for example, it has been shown that supported clusters on metal oxides are efficient epoxidation catalysts [65, 66], and clusters on titania are promising photocatalysts for self-cleaning, water splitting and water purification. Motivated in part by the unique structure which is responsible for the surprising catalytic activity of Au on TiO$_2$ [6], probing and understanding of the Ag growth mode on TiO$_2$ surface and corresponding interaction between these clusters and the substrate are important for both a basic science and industry application perspectives.

Moreover, a key element in understanding the catalytic properties of noble-metal/titania (TiO$_2$) systems is elucidating the role that that surface Ti*3d* defects play. Although a wide band bap insulator, bulk reduction (TiO$_{2-x}$) leads the formation of defects and, in the case of rutile TiO$_2$(110), these defects in the surface and selvage region modify the noble metal growth mechanisms or dictate the consequent surface chemistry [12, 67, 68]. Electronically, understanding the origin and role of the induced Ti*3d* derived state at (~ 0.85eV) *at the surface* is of fundamental importance, and in particular, how this state is modified by surface oxidation and, subsequently, Ag adsorption and growth.

In this study, all the measurements were performed on two different $TiO_2(110)$ surfaces, namely r- and o-$TiO_2(110)$. Whereas the former, prepared by sputtering and vacuum annealing to create a clean r-$TiO_2(110)$ surface, is characterized by a large amount of oxygen vacancy defects, subsequent oxygen exposure on the r-$TiO_2(110)$ surface provides an oxygen rich o-$TiO_2(110)$ surface. However, in addition to surface oxygen vacancies and adatoms, subsurface Ti^{3+} interstitial defects occur in both systems. In an effort to understand the role that these defects play and to identify the properties of the nucleation and growth of Ag on these two surfaces, we have used STM, UPS and EELS to probe the atomic, electronic, and optical (plasmonic) properties from submonolayer through monolayer/cluster (> 5ML) coverages. Using STM, the growth on the two different $TiO_2(110)$ are very different low coverages. Employing ultraviolet photoemission spectroscopy (UPS), valence band spectra of the Ag/titania systems were used to extract information regarding charge transfer and cluster growth at initial Ag coverage. Additionally, electron energy loss spectroscopy (EELS) experiments on both Ag on r- and o-$TiO_2(110)$ reveals information regarding both the perturbation of the surface titania defects and cluster size effects on Ag plasmon excitation on $TiO_2(110)$. Overall, electronic properties obtained from EELS and UPS studies confirmed the Ag growth modes observed with STM.

3.2 Experiment

All the experiment in this work was performed in ultra-high vacuum (UHV) chambers with base pressure of 2×10^{-10} Torr. $TiO_2(110)$ single crystals, purchased from different vendors (Commercial Crystal Laboratories, Princeton Scientific Corp., MTI Corp), were cleaned by cycles of Ne^+ sputtering (1.5keV, $I_{sample} \sim 10\mu A$, 30min) and vacuum annealing (900K, 20min). Electron bombardment from back of the sample was employed for annealing. Sample temperature was monitored with type-K chromel/alumel thermocouple welded onto the tantalum sample holder. This treatment results in a reduced bulk $TiO_2(110)$ crystal with n-type conductivity. The color of the crystal changes from transparent to yellow, green, blue and black finally, as the degree of reduction increases. A clear (1×1)

pattern with sharp spots was observed with low energy electron diffraction (LEED), indicating a clean flat surface obtained for further experiment. There are two types of $TiO_2(110)$ surfaces discussed in this paper, reduced (r-TiO_2) and oxidized (o-TiO_2): the r-TiO_2 surface is the sputtered and annealed clean surface mentioned above; and the o-TiO_2 surface is obtained by exposing the r-TiO_2 to O_2. The dosage of O_2 is measured in Langmuir (L) ($1L=1\times10^{-6}$ Torr·sec). Ag was deposited at room temperature on the prepared surfaces, respectively, using a thermal evaporator with clean high purity Ag wire wrapped in a tungsten filament. The coverage of Ag was determined from the STM images.

There are two UHV systems involved in this work. The first UHV system is equipped with LEED, STM and High Resolution Electron Energy Loss Spectroscopy (HREELS) spectrometer. The STM was designed and built by the Aarhus Scanning Probe group at Aarhus University in Denmark [69]. STM measurements were performed at room temperature in constant current mode. Etched tungsten tip was used. The LK2000 HREELS spectrometer made by LK Technologies provides us spectra with resolution of ~ 5 meV. EELS pectra were taken in a spectular geometry with an incident beam of 30eV. The second UHV system is the endstation at the 6m-TGM beam-line, delivering light with energy range from 15eV to 200eV, and has a resolving power better than 2000, at the CAMD synchrotron radiation facility. In addition to other surface science preparation/characterization tools, this endstation is equipped with Phoibos-100 electron analyzer used to acquire UPS spectra.

3.3 Results and Discussion

3.3.1 STM Results

Fig. 3.1 shows the STM images of the clean reduced $TiO_2(110)$ surface. Alternating bright and dark rows along the [001] direction can be seen on the terraces. In the case of $TiO_2(110)$, it is commonly agreed that the STM contrast is determined by the electronic structures of the surface, not the geometric structures [12, 70]. The dark rows are ascribed to bridge oxygen rows, which protrude out of the surface plane, while the in-plane 5-fold coordinated Ti (Ti_{5c}) rows are imaged as bright rows.

The sputtering and vacuum annealing process introduces varies kinds of defects on the $TiO_2(110)$ surface. This has been thoroughly reviewed by U. Diebold [12]. Fig. 3.1 also shows some of these surface defects. In Fig. 3.1(b), bright spots, indicated by circles, on darks rows are ascribed to bridging oxygen (O_{br}) vacancies on the O_{br} rows. O_{br} vacancies are the most observed defects on $TiO_2(110)$ surface, and, as described in the introduction, play an important role in the catalytic activities of $TiO_2(110)$. In Fig. 3.1(a), there are many strands growing out of the step edges with a bright dot at the end. These are the precursors of (1×2) reconstruction. However, on a lightly reduced $TiO_2(110)$ surface, these (1×2) strands are not seen.

STM images (Fig. 3.1(c) and (d)) show 0.1ML and 2ML Ag growth on r-$TiO_2(110)$ at room temperature. In metal growth, basic modes have to be mentioned [71]: layer-by-layer growth (FM mode), monolayer growth followed by three dimensional (3D) cluster growth (SK mode) and 3D cluster growth (VW mode). Previous studies of Au on $TiO_2(110)$ at room temperature reveal a two dimensional, thin-layer (bilayer) growth morphology forms at submonolayer coverages. When the Au coverage increases to $\sim$ 1ML, the growth morphology changes to three dimensional clusters [72, 73]. In stark contrast, Fig. 3.2 clearly shows that at very small coverage (0.1ML) Ag grows only in 3D cluster morphology on r-$TiO_2(110)$ at room temperature deposition. An important observation is that the 3D Ag clusters in Fig. 3.1(c) and (d) preferentially nucleate on step edges of the terraces. This finding has also been observed previously by other groups [74-77]. Line profiles (not shown) showed a narrow distribution of cluster size, which is about 5nm in diameter by 1nm in height in the submonolayer region. As the coverage increases above a monolayer, 3D Ag clusters nucleate and grow across terraces, the cluster size increases only slightly to about 7nm in diameter by 2nm in height [77]. Finally, at deposition at 125K, Ag was found to form two dimensional thin films at coverage below 0.8ML, but the thin films tends to form 3D clusters upon annealing very similar to the room temperature morphology [78]. The 3D clustering at step edges at submonolayer Ag coverages indicate a small diffusion barrier due to a weak adatom-substrate interaction.

As opposed to this growth on r-TiO$_2$(110), a different growth mode is observed when Ag was deposited on the o-TiO$_2$(110) surface at room temperature. Fig. 3.2(b) and (c) show STM image of 0.1ML Ag on o-TiO$_2$(110) surface, which was prepared prior by dosing 10L and 20L O$_2$ on the r-TiO$_2$(110) surface. As seen in the image, Ag clusters are uniformly dispersed on terraces at low coverage (0.3ML), and there is a substantially decreased density of 3D clusters nucleating on step edges. Line profiles indicate an average cluster size of about ~3nm across and ~0.5nm high, which is significantly smaller than that of the Ag/r-TiO$_2$(110) surface, especially with respect to the height. Moreover, as compared with the clean r-TiO$_2$(110) surface, the clean o-TiO$_2$(110) surface is appears atomically rougher due to the oxygen adatom on the surface (Fig. 3.2(a)). From the observed Ag nucleation and growth, it is apparent that the excess oxygen adatoms increase the diffusion barrier for Ag, resulting in a more uniformly dispersion of smaller Ag clusters. The present results are in close agreement with more detailed STM studies of the o-TiO$_2$(110) and Ag/o-TiO$_2$(110) surface [22, 67, 79, 80]. In these previous STM studies, it was shown that only small O$_2$ exposures on clean r-TiO$_2$(110) surface results in nearly perfect O$_{br}$ rows and with bright adatom spots on Ti$_{5c}$ rows [22, 67, 79, 80]. The healing mechanism of the r-TiO$_2$(110) surface results primarily from one O$_2$ molecule dissociating into two O atoms, one filling an O$_{br}$ vacancy, while the other one is adsorbed on the surface, probably the Ti$_{5c}$ site, forming a O adatom [81, 82]. This O$_2$ dissociation mechanism is also supported by theoretical calculations [83, 84]. As we observe in this study, on this o-TiO$_2$(110) surface, Ag clusters are much smaller and more dispersed than on r-TiO$_2$(110) surface [22] at submonolayer coverages. At 0.04ML Ag, the majority of the Ag clusters are Ag monomers trapped on O adatom sites. These Ag monomers are very stable upon annealing, indicating enhanced bonding between Ag clusters and the o-TiO$_2$(110) surface [22].

In summary, our large-scale STM images reveal a very similar trend observed in previous studies. Specifically, deposition of submonolayer Ag on the o-TiO$_2$(110) surface at room temperature results in nucleation and growth of smaller cluster evenly distributed across terraces. This is in contrast to Ag
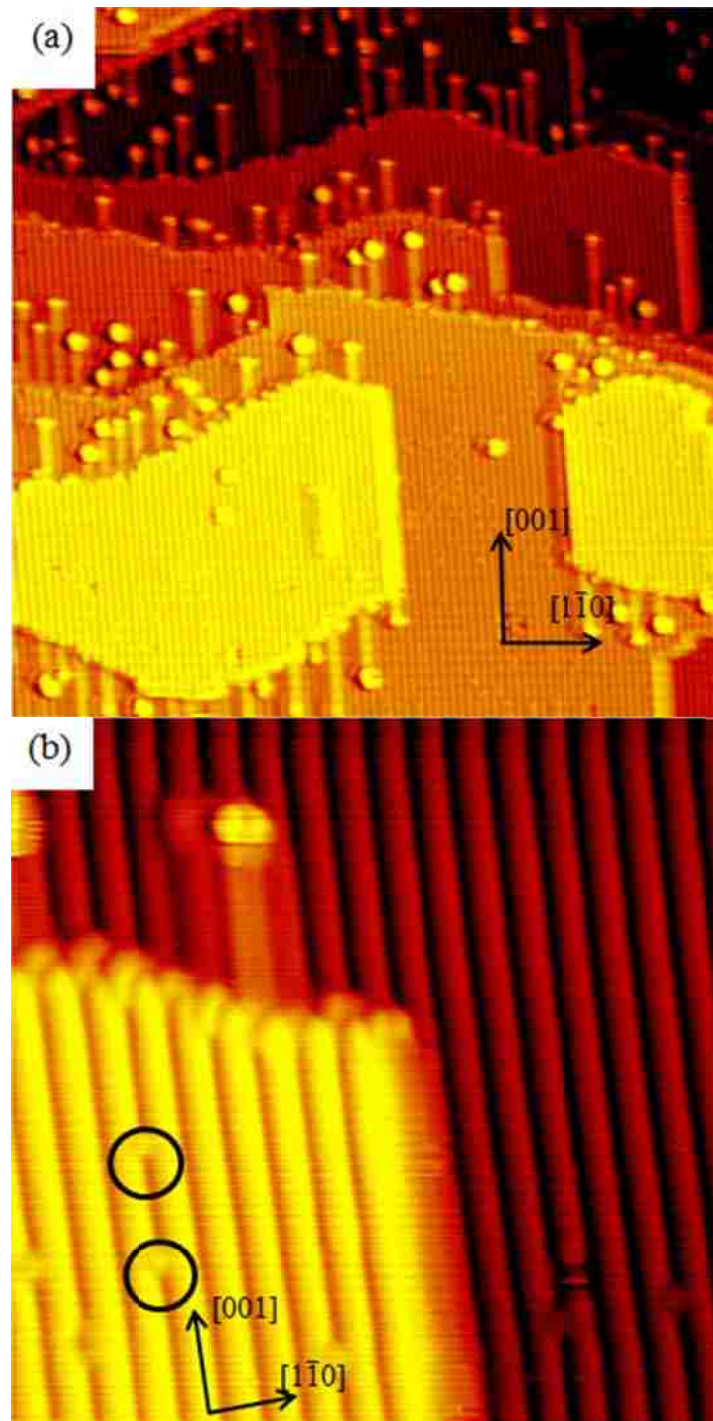
Fig. 3.1 STM images at room temperature of (a) 300Å×300 Å (b) 100Å×100Å clean r-TiO$_2$(110) showing terraces, bright and dark rows are Ti$_{5c}$ and O$_{br}$ rows, features marked with black circles are oxygen vacancies (c) 1000Å×1000Å 0.1ML Ag on r-TiO$_2$(110) at room temperature, cluster size ~5nm across × 1nm high (d) 1000Å×1000Å 2ML Ag on r-TiO$_2$(110) at room temperature, cluster size ~7nm across × 2nm high

(Fig. 3.1 continued)
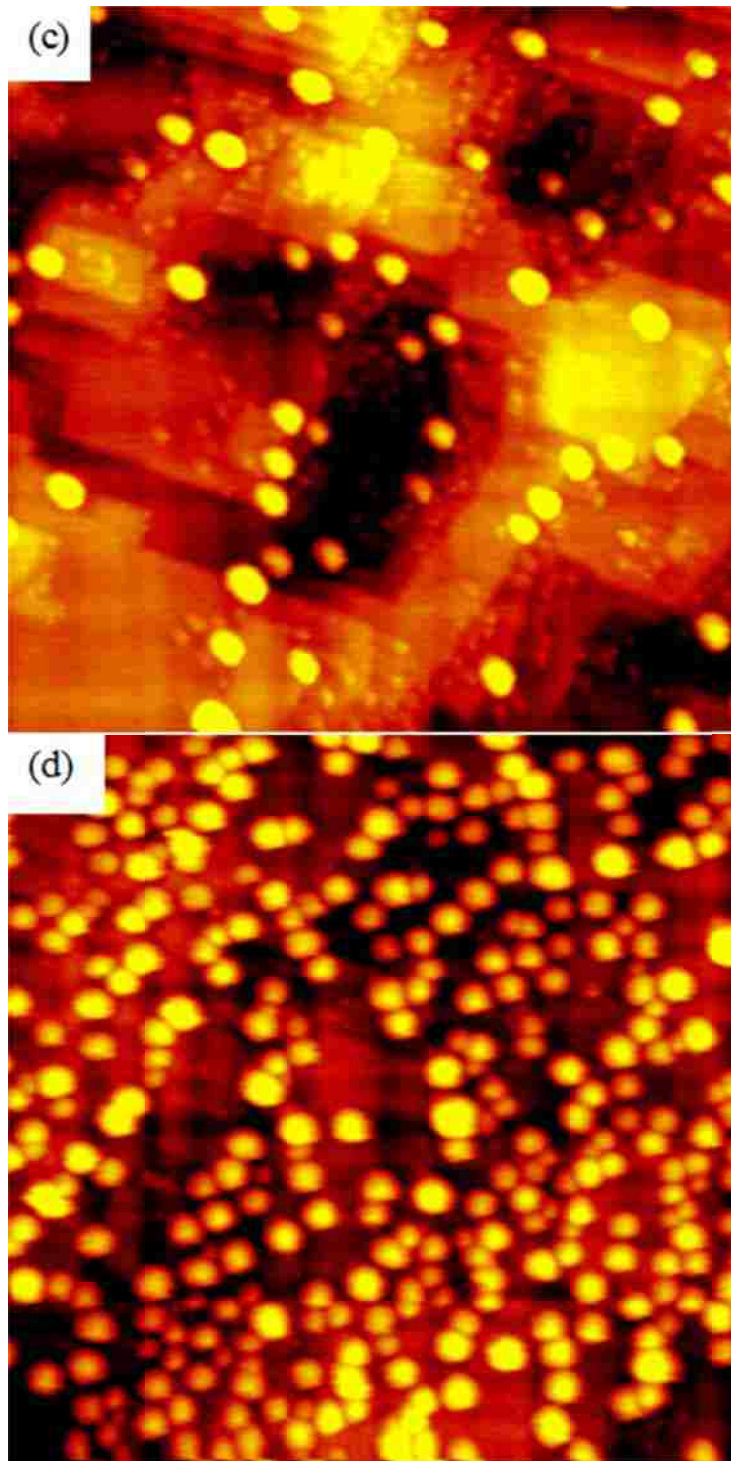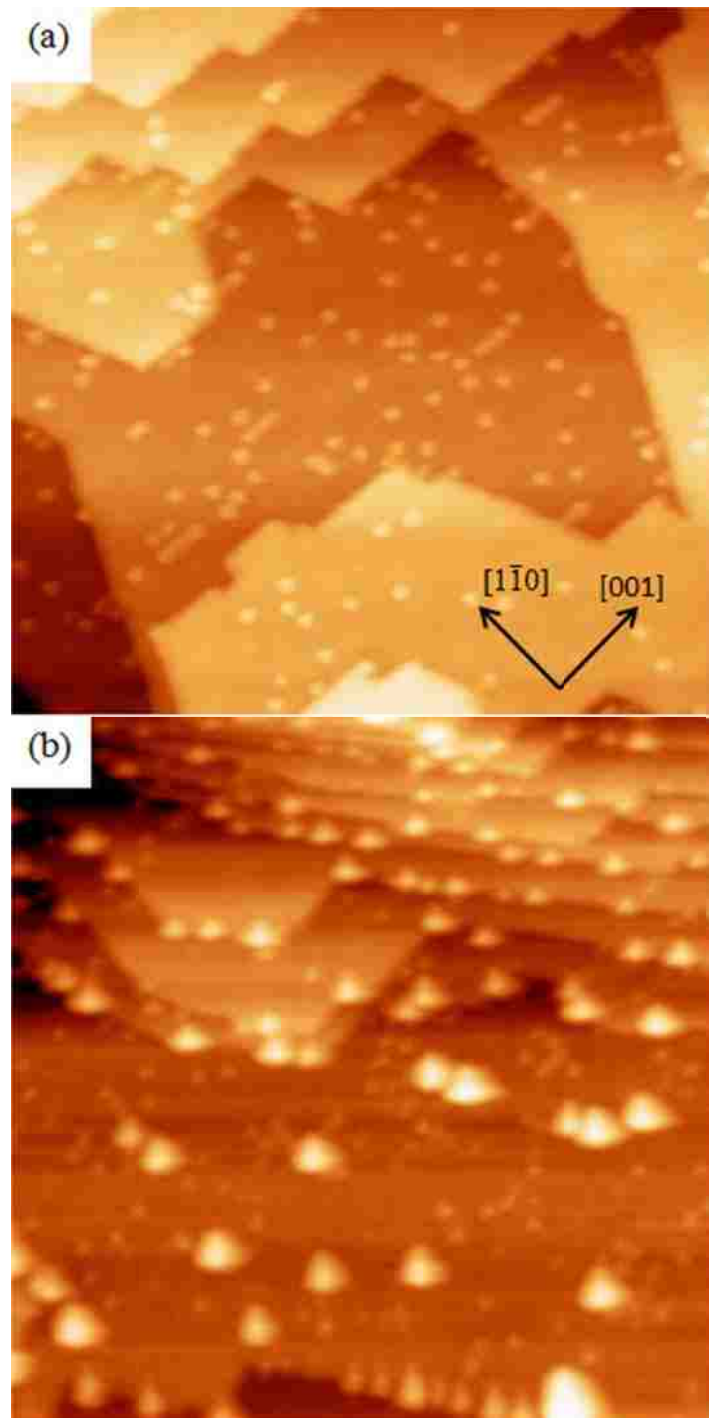
Fig. 3.2 STM images at room temperature of (a) 1000Å×1000Å 10L o-TiO$_2$(110) surface, prepared by exposing the clean r-TiO$_2$(110) to 10L O$_2$ at ~250°C, oxygen clustering (~3nm across × 0.2nm high) is seen on the surface (b) 1000Å×1000Å 0.1ML Ag on 10L o-TiO$_2$(110) surface, bigger clusters of ~5nm across × 0.8nm high on terraces, smaller clusters of ~3nm across × 0.4nm high on steps (c) 1000Å×1000Å 0.1ML Ag on 20L o-TiO$_2$(110) surface, cluster size is about the same as in (b)

42

(Fig. 3.2 continued)
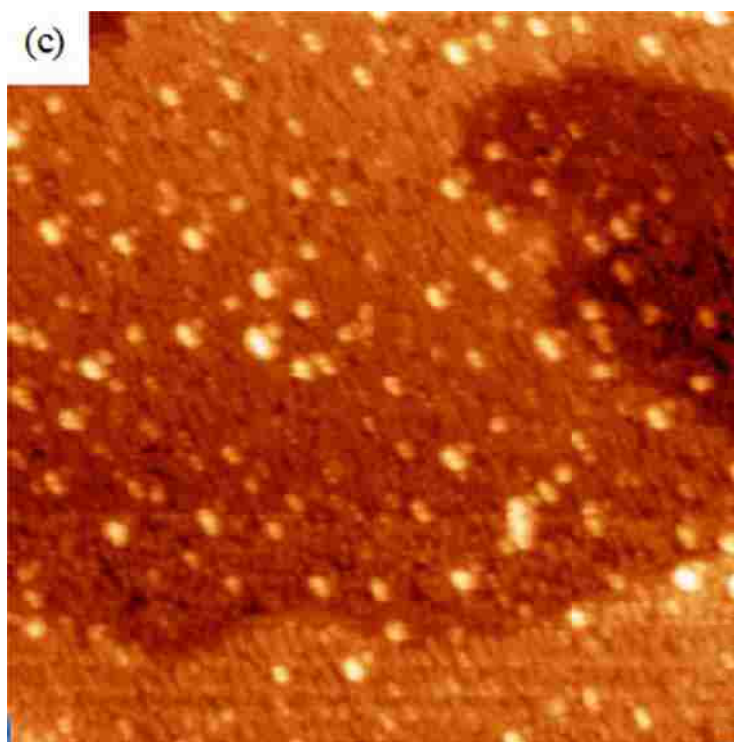
deposition the r-TiO$_2$(110) surface wherein 3D clusters are observed to nucleate at step edges even at lowest coverages. At coverages at multi-monlayers (> 5 ML), both systems reveal a 3D clustering morphology which covers the surface.

3.3.2 Photoemission Results

Valence band spectra (UPS) as a function of coverage of Ag on both r-TiO$_2$(110) and o-TiO$_2$(110) surfaces (photon energy of 48eV) are shown in Fig. 3.3. All the spectra are properly normalized. In Fig. 3.3(a), the broad feature between 3eV and 10eV binding energy (BE) in the clean r-TiO$_2$(110) spectrum is due to O 2p band, which consists of contributions from different oxygen molecular orbitals [85, 86]. Moreover, a pronounced Ti*3d* defect state at a BE of 0.85eV. As Ag is deposited the clean, slightly reduced surface, a number effects are clearly observed in the UPS spectra.

The largest changes correspond to the O 2p band being gradually attenuated, while Ag 4d band starts to evolve in the same energy range as coverage increases.

Spectra of Ag/o-TiO$_2$(110) in Fig. 3.3(b) show the same trend as the Ag/r-TiO$_2$(110). The O 2p band and Ag 4d band are largely overlapped in the spectra, because of this overlap it is very difficult to obtain the energetics from these photoemission spectra, such as charge transfer between Ag clusters and substrate. A curve fitting procedure was employed here to help elucidate the evolution of O 2p band and Ag 4d band as the Ag coverage increases. Namely, the curves of intermediate Ag coverage were fitted as a linear combination of two basic curves: 1) clean curve (0 ML Ag) and 2) bulk Ag curve (thick Ag; >7ML). Here we assumed the thickest Ag/TiO$_2$(110) curve represents bulk Ag curve. An example of this fitting procedure is shown in Fig. 3.4(a) for a coverage of 1.6 ML Ag on the r-TiO$_2$(110) surface. Four parameters were introduced in this fitting: two intensity scaling factors and two BE shifts. From this procedure, the BE shifts of clean and bulk Ag curves indicate that the O 2p band and Ag 4d bands are shifted, and intensity scaling factors imply the relative amount of each are on the surface.

As shown in Fig. 3.4 (a) for the 1.6ML example, this procedure results in good fit, that is, the fitted spectrum is nearly identical to the experimental spectrum (small residual is indicated as shown at the bottom). Fittings for other Ag coverage spectra are not shown here are nearly as perfect as the "1.6ML Ag" curve fitting, except for the lowest Ag coverage due to decreased intensity component. From this fitting procedure there was no overall shift in the O 2p band (clean BE shift), but there was a prominent shift of the Ag 4d band on both surfaces. The shift amount of Ag valence band obtained from the fitting is plotted in Fig. 3.4 (b).

On the r-TiO$_2$(110) surface, the Ag valence band shifted 0.8eV to higher BE at 0.2ML Ag coverage compared to the bulk Ag spectra. As the coverage increases, the BE shift amount decreases rapidly, and goes to almost zero at coverage of about 2.5ML. A similar behavior was observed for the
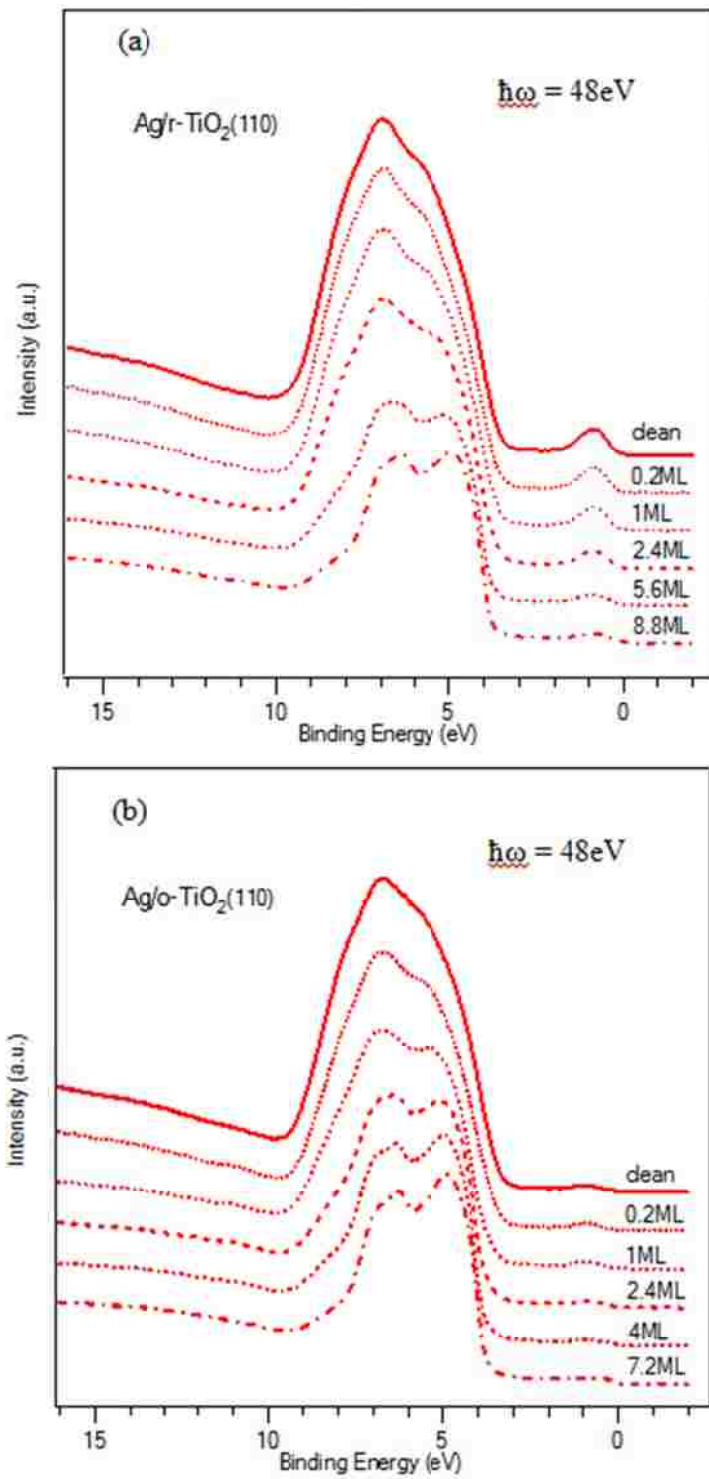
Fig. 3.3 Valence band photoemission spectra of Ag on (a) r-TiO$_2$(110) (b) 600L o-TiO$_2$(110) at normal emission
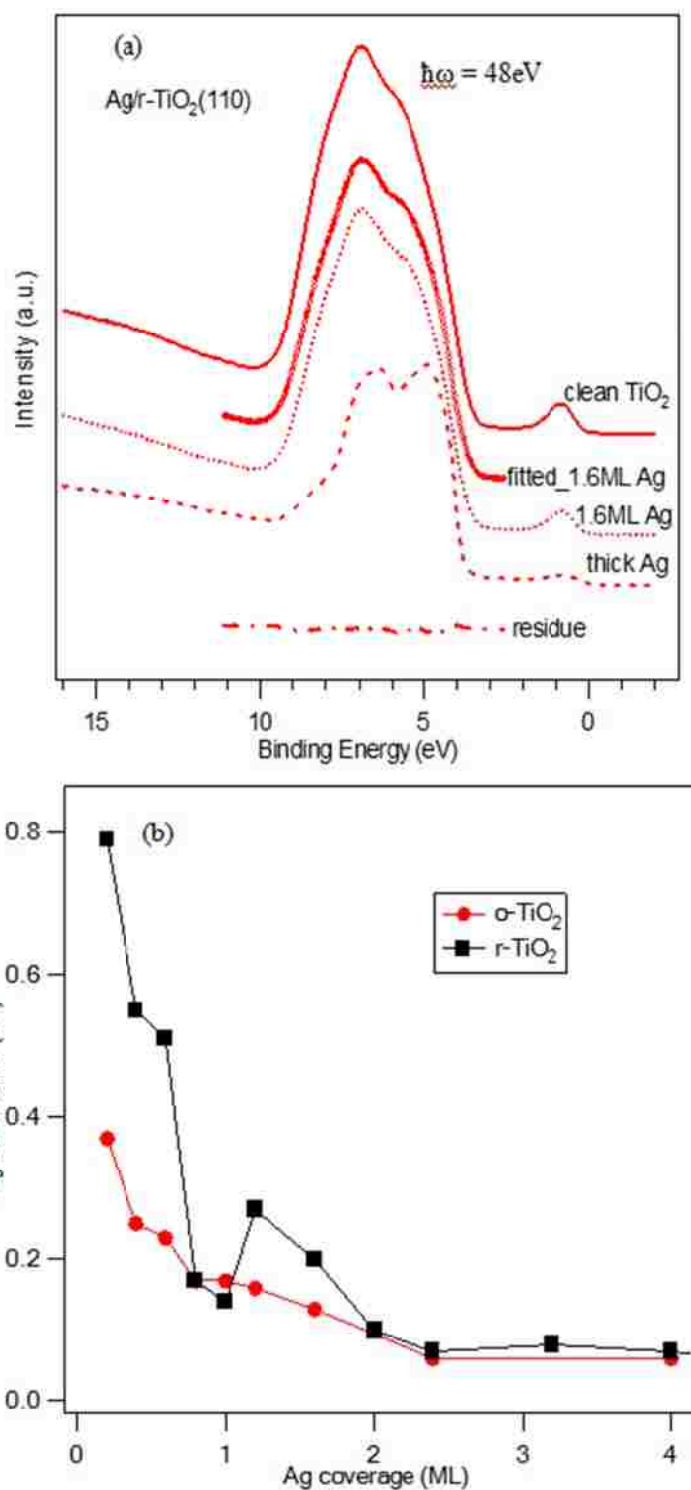
Fig. 3.4 Fitting of valence band as linear combination of O 2p and Ag 4d band (a) sample fitting of 1.6ML Ag/r-TiO_2(110) spectrum (a) sample fitting of 1.6ML Ag on r-TiO_2(110), residue is almost zero, meaning the fitting is very successful (b) Ag band shift vs Ag coverage for both r- and o- TiO_2(110) surface (c) relative weight (O/Ag) vs. Ag coverage

(Fig. 3.4 continued)
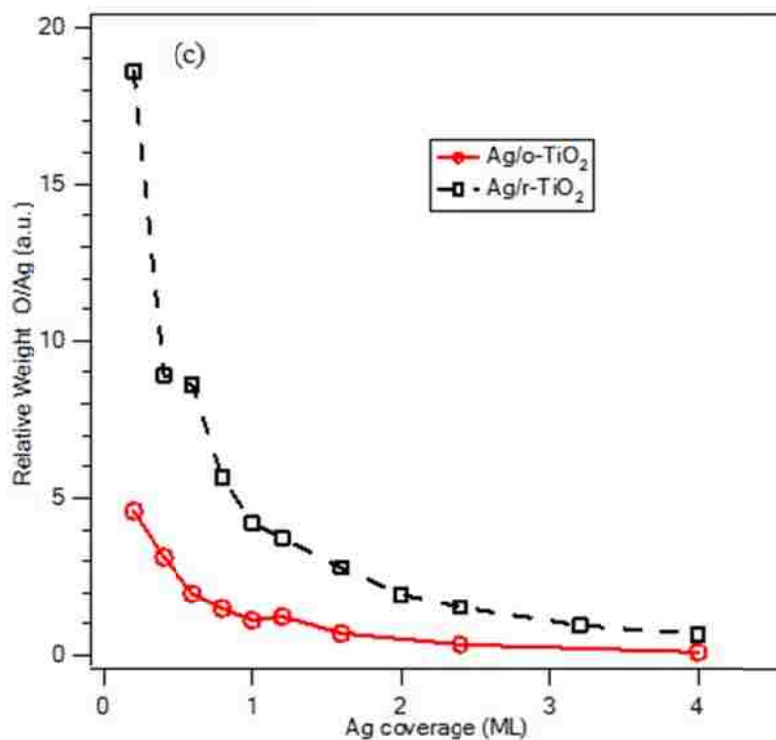
Ag/o-TiO$_2$(110) surface, but the shift amount at 0.2ML coverage is about 0.38eV, which is somewhat smaller than Ag/r-TiO$_2$(110) surface. The critical coverage for the BE shift to vanish is also about 2.5ML. The same critical coverage of 2.5ML on both surfaces is reasonable. At this high coverage, STM reveals that Ag clusters finish ripening and reach approximately uniform size. The large clusters are homogeneously spread and nearly cover the whole surface, thus show bulk 4d Ag behavior in the photoemission spectra. To explain the band shifts submonolayer Ag coverages, both initial and final state effects have to be considered [76, 87-91]. After the photoemission process, there is less screening of the positive hole left on small particles because of reduced electrons, thus lead to a spectra shift to higher BE (lower kinetic energy). This final state effect will cause the same shift towards higher BE for small Ag nanoclusters on both r- and o- TiO$_2$(110) surfaces at initial coverage. As stated before, we observed a larger Ag 4d valence band shift on r-TiO$_2$(110) surface than on o-TiO$_2$(110) surface, this

47

may indicate different interactions between Ag nanoclusters and substrates. A previous study showed that thin Ag oxide layer will be formed at the Ag-TiO$_2$ interface with excess oxygen present at room temperature [92]. In our photoemission measurement, o-TiO$_2$(110) was prepared by exposing r-TiO$_2$(110) to 600L O$_2$, which should lead to an oxygen rich surface. When Ag was evaporated on this surface, the strong affinity between Ag nanoclusters and oxygen will results in a large charge transfer from Ag to oxygen atoms. For most transition metals, a shift towards higher BE will be seen upon oxidation due to the reduced screening of electrons from the nucleus. However, silver is one of the exceptions which show a shift towards lower BE in the oxidation state [92-95]. The oxidation of Ag caused a negative BE shift, which canceled out part of the positive BE shift from the final state effects. This may be an explanation of why we observed a larger positive BE shift for the Ag valence band on r-TiO$_2$(110) (0.8eV) than on o-TiO$_2$(110) (0.38eV) surface at 0.2ML Ag coverage. A different result was reported in Hansen's paper [22], where they found a shift of 0.7eV at 0.35ML Ag on o-TiO$_2$(110) surface, and a smaller shift for Ag on r-TiO$_2$(110) surface. This contradiction may result from the sample preparation process.

Important information about the Ag growth mode could also be obtained from the fitting of the valence band. There are four parameters involved in this fitting process, apart from the BE shift amount of O and Ag valence band, the weight of each component contributed to the fitted curve was also calculated. In Fig. 3.4(c), the ratio of O weight over Ag weight versus Ag coverage is plotted. At coverage of 0.2ML Ag, this ratio is 19 for r-TiO$_2$(110) surface compared to 5 for o-TiO$_2$(110) surface. This result is consistent with the STM results presented above. At initial coverage, Ag clusters nucleate at step edges on r-TiO$_2$(110) surface, thus cover a very low surface area. In photoemission spectra, the valence band is largely contributed from O 2p band with only a little portion from Ag 4d band. On o-TiO$_2$(110) surface, smaller Ag clusters spread all over the terraces on the surface even at initial
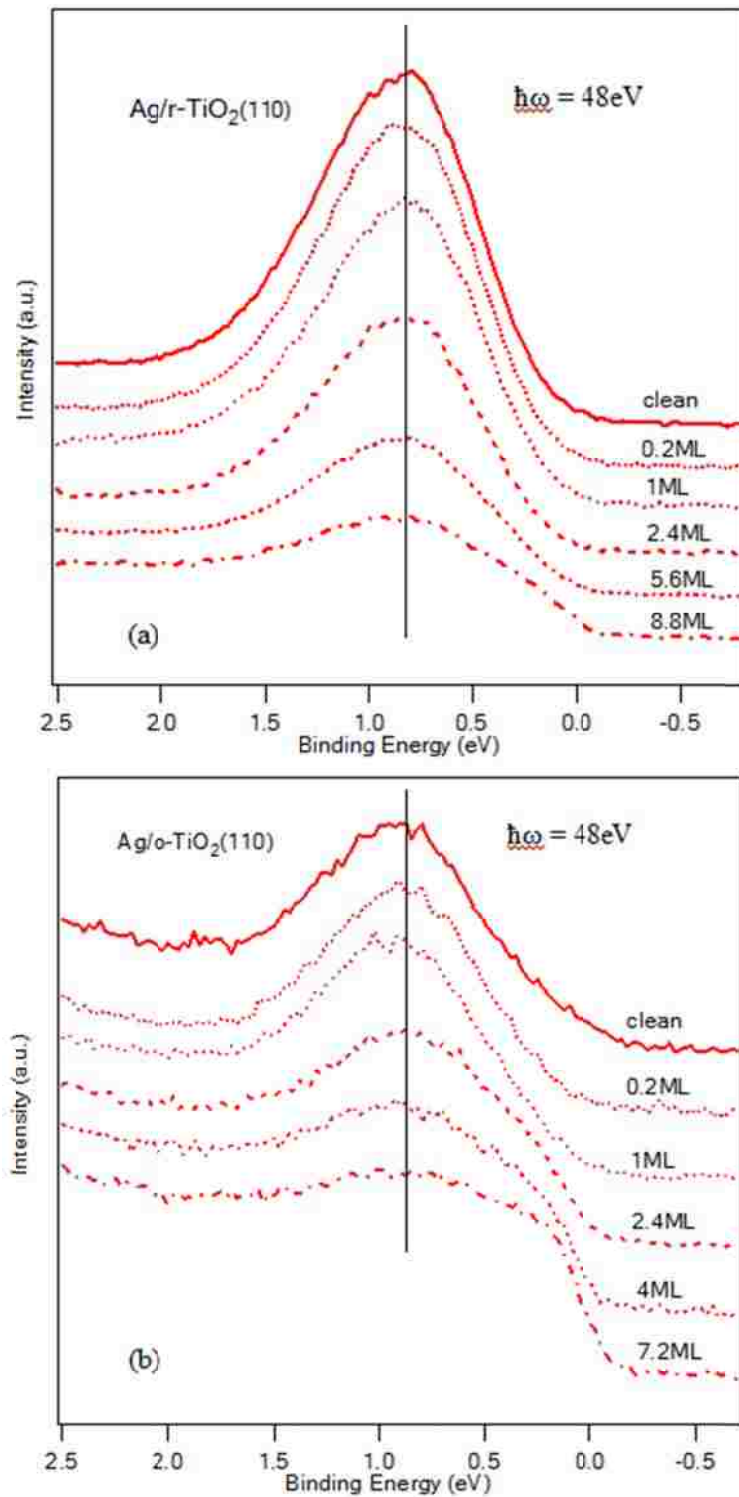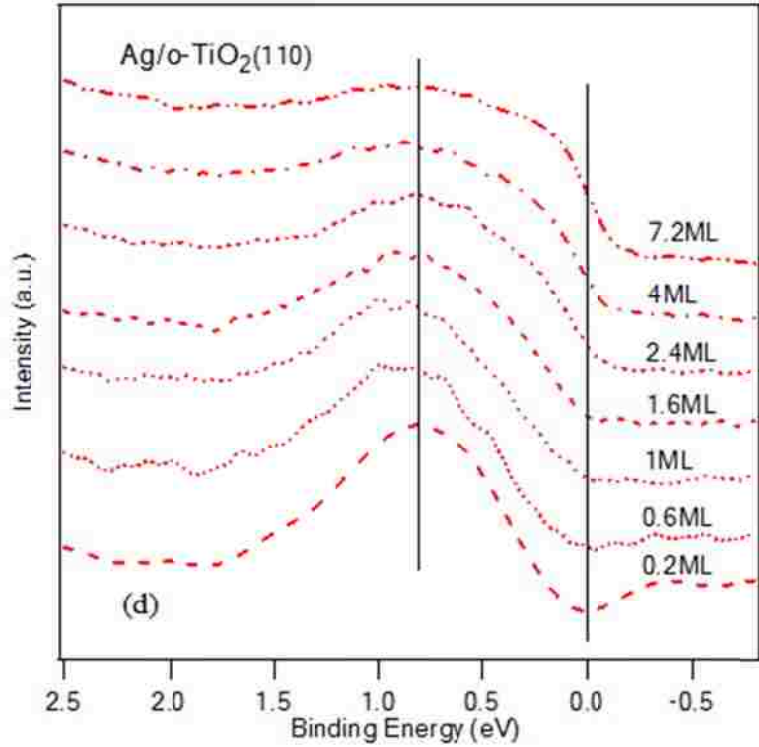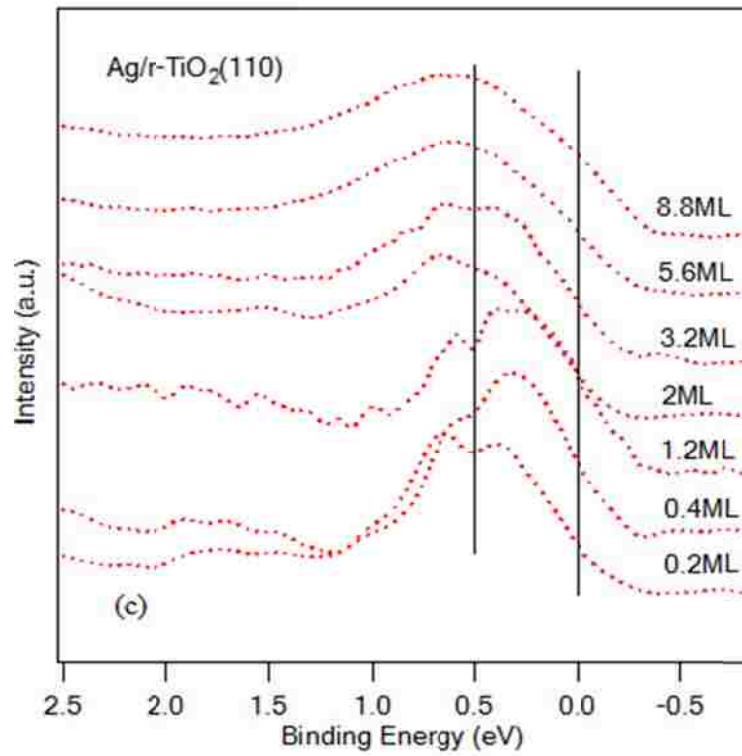
Fig. 3.5 Photoemission spectra showing the defect state of Ag on (a) r-TiO$_2$(110) (b)600L o-TiO$_2$(110), difference spectra of defect state of Ag on (c) r-TiO$_2$(110) (d) 600L o-TiO$_2$(110), showing the evolution of Ag 5sp state

49

(Fig. 3.5 continued)

50

coverage, results in a lower surface area of TiO_2 exposed in photoemission measurement. In the case, Fig. 3.4(c) shows less O 2p band contributed to the valence band, As Ag coverage increases, the ratio decreases for both surfaces, and nearly converges to the same quantity at high coverage (> 3ML).

Apart from the O 2p and Ag 4d states, information related to the growth mode and electronic interaction of the Ag/titania system can be extracted from a careful analysis of the intensity and BE of the defect state. As shown in Fig. 3.5(a), on r-TiO_2(110) surface, a prominent feature peaking at 0.8eV below Fermi level is ascribed to Ti 3d states, which is due to, in part, by O_{br} vacancies. As a function of increasing Ag coverage, the intensity of the defect peak (BE at 0.8eV) gradually decreases, and a concomitant Fermi edge evolves at high Ag coverage. Comparing the intensity of the defect state on the clean r-TiO_2(110) surface in Fig. 3.3(a) to the clean o-TiO_2(110) surface in Fig. 3.3(b), one can clearly see that the intensity of defect state was greatly suppressed upon exposure of 600L of O_2. Quantitatively, the intensity (area) is decreased by factor of 4. However, as shown in Fig. 3.5(b), the defect state is not totally absent. This is because the defect state shown in photoemission spectrum is not completely caused by O_{br} vacancies, but partially originated from Ti interstitials in the near surface region [96]. To better elucidate Ag 5sp band behavior in the same energy region, scaled clean TiO_2 spectrum were subtracted from each of the respective Ag coverage spectrum, thus yielding the Ag 5sp band behavior, which are shown in Fig. 3.5(c) and (d). At small initial coverage (~ 0.2ML), the difference spectra showed atomic behavior with prominent peaks located at 0.5eV and 0.8eV below Fermi level for r-TiO_2(110) and o-TiO_2(110) respectively. From STM results above, it is known that Ag forms smaller clusters on o-TiO_2 surface, resulting in a larger BE (0.8eV) compared to that (0.5eV) on r-TiO_2 surface. Larger coverage results in a shifting of the Ag band towards lower BE, and the peak was broadened, because of the increased Ag cluster size. On both Ag r-TiO_2(110) and o-TiO_2(110) surfaces, the 5sp band continued to broaden and finally crossed the Fermi edge at ~2ML coverage, showing metallic behavior. This result is in close agreement to both STM and O 2p/Ag 4d UPS results and thus further confirms the growth modes of Ag on r- and o- TiO_2(110) surfaces discussed above.

51

3.3.3 EELS Results

The oxidation of r-TiO$_2$(110) and Ag growth on both r- and o- TiO$_2$(110) surfaces were also studied with EELS. Fig. 3.6(a) shows a series of spectra of r-TiO$_2$(110) upon gradually oxidation. On the clean r-TiO$_2$ spectrum, a broad band starting at ~3.2eV is due to the interband transition of TiO$_2$, the onset energy of 3.2eV corresponds to the bandgap of TiO$_2$. A broad shoulder between 0.6eV and 2eV is ascribed to defect excitations in TiO$_2$, and this shoulder was attenuated upon O$_2$ exposure as shown. Integrated areas of the shoulder were calculated and plotted versus O$_2$ dosage in Fig. 3.6(b). The area of the defect states went down to about 1/4 of the value of clean TiO$_2$ at initial 5L O$_2$ dosage. Upon further oxidation, the value gradually decreases and approaches to zero after 200L O$_2$ dosage. The change of defect state intensity upon O$_2$ exposure is different from what was observed in photoemission measurements. In UPS, the amount of O$_2$ needed to completely annihilate the defect state is far more than 200L (see Fig. 3.5(b) for comparison), but in EELS a sharp decrease of the defect state intensity is observed at relatively low O$_2$ exposure (< 50L). Due to extreme surface sensitivity of EELS versus UPS, the defect excitations observed in EELS are almost exclusively from the surface O$_{br}$ vacancies, which are easily healed by O$_2$ exposure. However in photoemission studies, Ti interstitials in the subsurface region also contributes to the defect state intensity, which will be largely affected upon oxidation. This EELS - UPS comparison of the defect state intensity is a direct confirmation that the defect state observed in UPS does not exclusively originate from surface O$_{br}$ vacancies, rather it is partially due to subsurface Ti 3d interstitials. Consequently, this implies that surface chemistry on both the clean r- and o-TiO$_2$(110) surfaces may be strongly influenced by the defect state originating from the Ti interstitials in the selvage region.

Two different Ag coverages on both surfaces were studied with EELS, here the o-TiO$_2$(110) surface was obtained by dosing 5L O$_2$ on r-TiO$_2$(110) surface. In Fig. 3.7(a) and (b), EELS spectra of clean r- and o- TiO$_2$(110) surfaces, 0.3ML and 1.5ML Ag on top of both surfaces are shown. For reference, the clean r- and o- TiO$_2$(110) EELS spectra are similar to those found in Fig. 3.6(a).
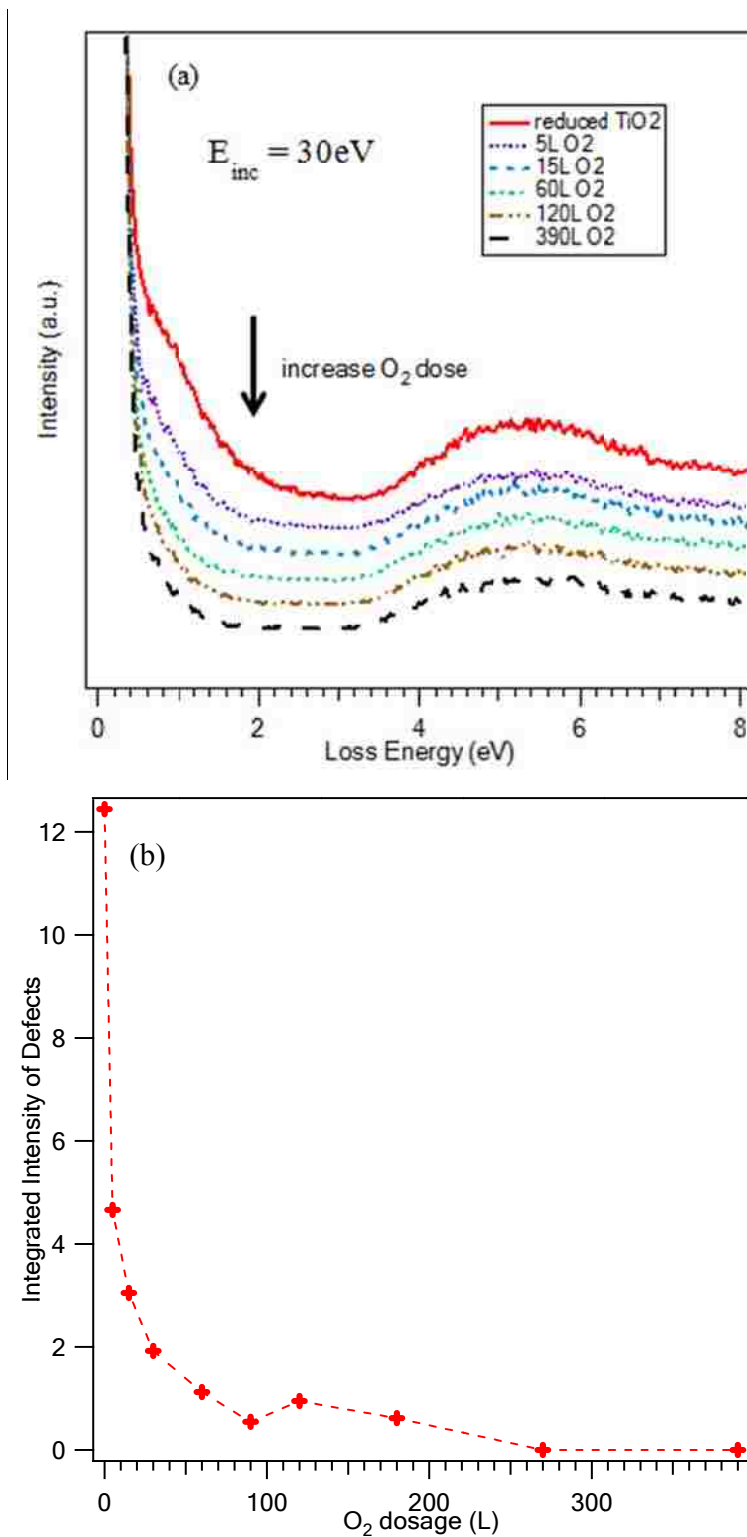
Fig. 3.6 (a) EELS spectra of r-TiO$_2$(110) upon O$_2$ exposure, broad feature between 0.5eV and 2eV loss energy is the defect state (b) Integrated intensity of defect state vs. O$_2$ dosage, defect state is quenched by a little O$_2$ dosage, while in photoemission, after 600L O2 dosage, defect state drops to about 25% of original value, but in EELS, 15L O$_2$ leads to the same drop

At coverage of 1.5ML, according to our STM and PES studies, Ag forms almost ripened clusters on both r- and o- $TiO_2(110)$, which results in very similar surface morphology. Because of that, the EELS spectra for 1.5ML Ag coverage on both surfaces are quite similar. They both show a sharp peak at 3.6eV with a weak shoulder at lower loss energy. The sharp loss peak at 3.6eV is identified as the plasmon excitations of Ag nanoclusters, this loss energy is very close to the Mie plasmon of free Ag clusters and the surface plasmon of Ag single crystal. However, at 0.3ML Ag coverage, EELS spectra did show distinct behavior for the two different substrates. Subtracting the scaled clean spectra from both the 0.3 and 1.5 ML spectra shown in Fig. 3.7(c) and (d) clearly reveal that new loss mechanism has to be introduced for very low coverage. Specifically, for o-$TiO_2(110)$ surface, 0.3ML Ag on top shows a prominent peak at 3.2eV with a shoulder at higher energy (3.6 eV). While a broad loss feature with two almost equally weighted peaks located at 3.2eV and 3.6eV were seen for r-$TiO_2(110)$. At low coverage of 0.3ML, the size distribution of Ag nanoclusters varies drastically on r- and o- $TiO_2(110)$ surfaces, and it is believed that the cluster size effects caused the energetic difference in interband/plasmonic behavior observed in the EELS spectra. For 0.3ML Ag on o-$TiO_2(110)$ surface, sharp loss peak at 3.2eV is tentatively ascribed to a more atomic-like interband transition from Ag 4d to Ag 5sp band. At this coverage, STM shows that very small Ag nanoclusters ($\sim 2\times0.4$ nm) homogeneously dispersed across the surface. The clusters are so small that collective excitation such as plasmon is not applicable, and thus the corresponding intensity of the plasmon loss at 3.6eV, due to the screening, is attenuated at this low Ag coverage. On the hand, the r-$TiO_2(110)$ surface, STM revealed larger Ag nanoclusters nucleating at step edges even at the lowest coverage and these larger Ag nanoclusters contributed to the stronger plasmon loss at 3.6eV on 0.3ML Ag/r-$TiO_2(110)$ spectrum compared to Ag/o-$TiO_2(110)$ spectrum.
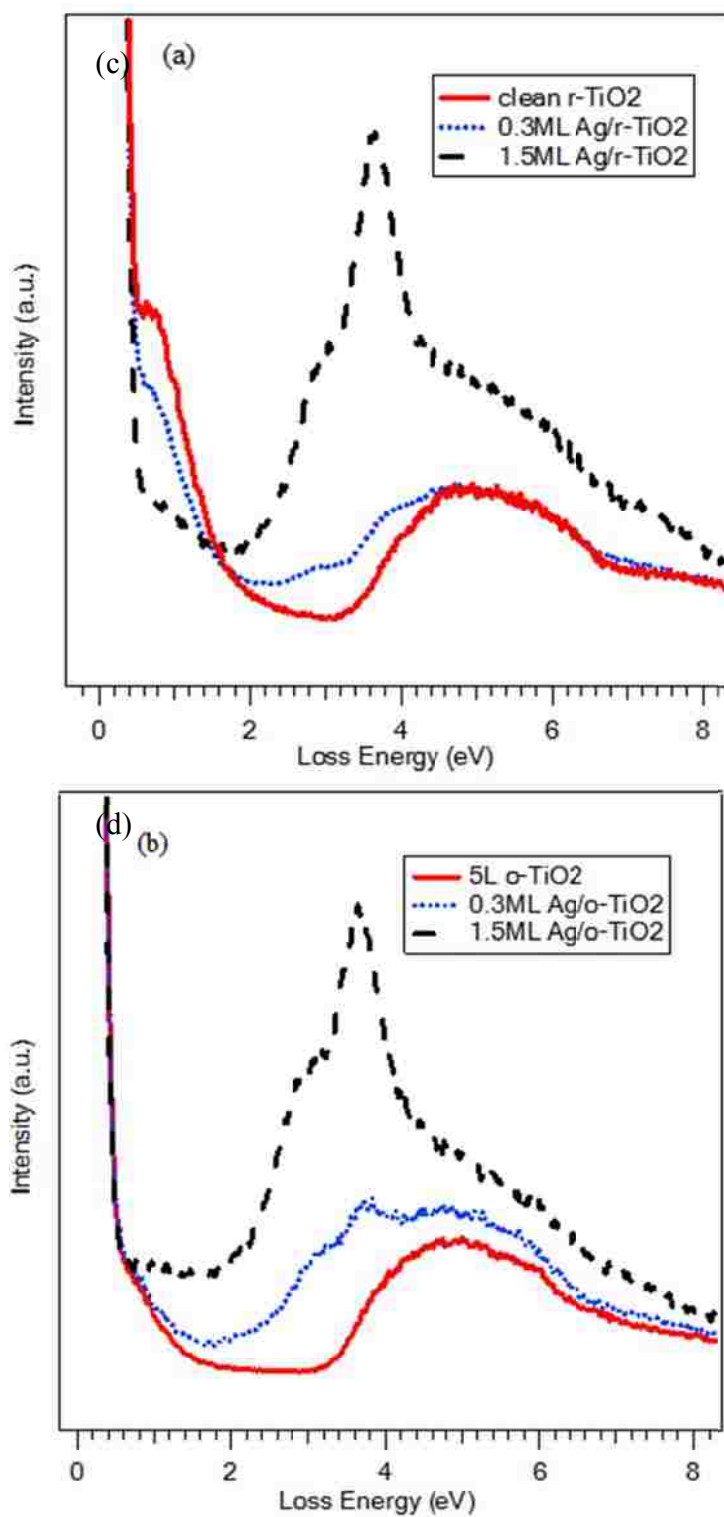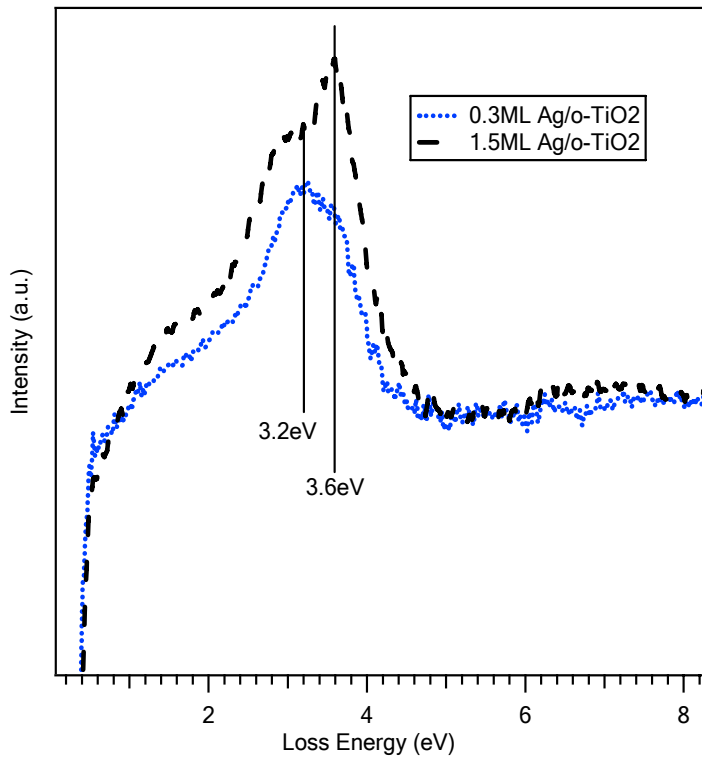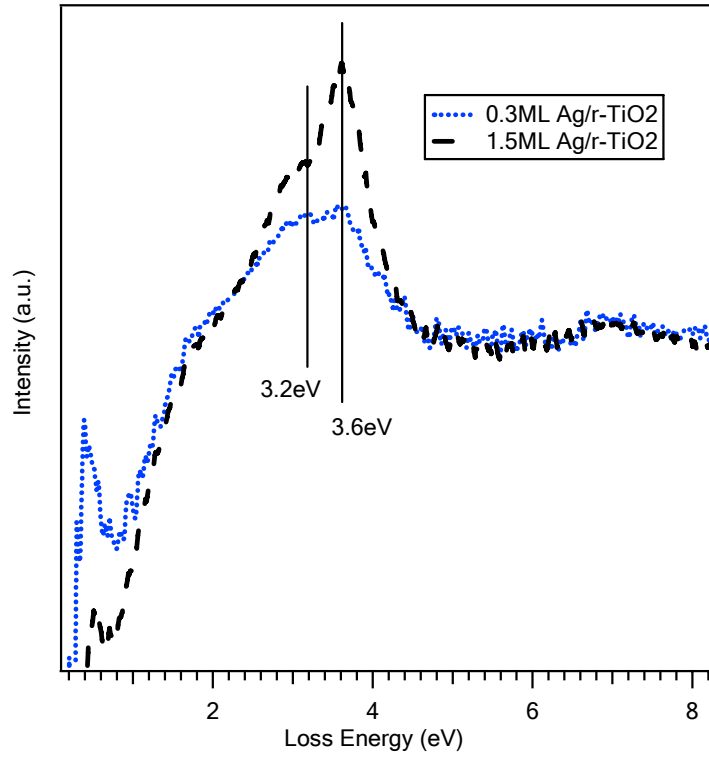
Fig. 3.7 EELS spectra of 0.3ML and 1.5ML Ag on (a) r-TiO$_2$(110) (b) 5L o-TiO$_2$(110) surfaces, Difference spectra of 0.3ML and 1.5ML Ag on (c) r-TiO$_2$(110) (d) 5L o-TiO$_2$(110) surfaces

55

(Fig. 3.7 continued)

3.4 Conclusions

Ag growth mode and electronic structures on both r- and o-TiO$_2$(110) surfaces have been carefully studied with STM, PES and EELS at room temperature. At initial coverage, STM revealed that while preferential nucleation and growth of Ag 3D nanoclusters at step edges on r-TiO$_2$(110) surface, the growth of homogeneously dispersed, much smaller nanoclusters of Ag was deposited on o-TiO$_2$(110). This implies a stronger Ag-substrate bonding mechanism, and lowered diffusion barrier, on the o-TiO$_2$(110) surface. In both cases, UPS shows a charge transfer in the submonolayer region. It is believed that on the o-TiO2(110) surface, a larger charge transfer from Ag nanoclusters to substrate (oxidation of Ag) will probably happen when excess oxygen is present. However, the Ag 5sp state shifts to lower BE and broadens as the coverage is increased from the lowest submonolayer coverages, again consistent with the minimized cluster size. In EELS spectra, plasmon excitation at 3.6V loss energy was not seen for very small nanoclusters on o-TiO$_2$(110) surface. Instead, a peak located at 3.2eV dominated the loss feature, which is consistent with a less screened interband transition from Ag 4d to 5sp band. Further deposition of Ag leads to the ripening of Ag nanoclusters. At about 2ML coverage, large Ag nanoclusters covered almost the whole surface for both r- and o- TiO$_2$(110) substrates, and showed metallic behavior in photoemission spectra. These large Ag nanoclusters exhibited strong plasmon excitations in EELS spectra. Finally, a close comparison between the UPS and EELS determined Ti 3d defect state intensity indicates that the origin of the defect state is not limited to surface oxygen vacancies, but also include a strong contribution from subsurface Ti 3d interstitials.

Chapter 4: Optical Excitations of Metallic Ag Nanoclusters Buried in TiO$_2$ for Solar Photochemistry

4.1 Introduction

Water interactions with TiO$_2$ and other oxide surfaces have been thoroughly studied since Fujishima and Honda reported on its ability to split water by photolysis [11]. The promise of using photolysis as a means of producing hydrogen fuel is a particularly attractive goal but there are significant challenges to enhancing the efficiency to the point where it can be a competitive process. As noted in recent DOE publications, the three major roadblocks to solar photoelectrolysis of water to produce hydrogen are the need for an efficient semiconducting absorber of light, a requirement of long-term stability of the semiconductor in the electrolytic environment, and suitable energetics in band matching so that photoexcited carriers efficiently react with the water.

TiO$_2$ itself is a weak absorber of solar spectrum (Fig. 4.1) with bandgap of 3.2eV. In this work, we are investigating the means that metallic nanoclusters can be incorporated within our semiconductor to enhance the absorption of the solar spectrum by utilizing their plasmon resonances. One challenge is that the plasmon resonances of metallic nanoclusters often absorb in the ultraviolet, falling outside of much of the solar spectrum [97] and are also only weakly dependent on cluster size. Secondly, metallic clusters adsorbed on an oxide surface are likely to be unstable within an oxidizing electrolyte.

Although the size distribution of the clusters on rutile can control the resonant absorption energy somewhat, studies showed that placing the metal nanoclusters in a dielectric matrix causes broadening and red-shift of their surface plasmon resonance, allowing the photoabsorption to be modified to fit the solar spectrum [98]. Several theories have been proposed to explain the observed redshift of surface plasmon resonance [99-101], among which the Maxwell-Garnett theory is widely adopted because of its simplicity and validity [100, 102]. A natural dielectric to consider is to encapsulate these metal

clusters supported on TiO$_2$ with an overlayer of TiO$_2$. Buried metallic nanoclusters (~5-50nm) within nanometers of the TiO$_2$ surface are a highly promising approach. Noble-metal clusters (Cu, Ag, Au) are known to be stable on TiO$_2$, and we will show that they can be encapsulated intact within TiO$_2$.

In this work, the proposed dielectric matrix structure is shown schematically in Fig. 4.2. Ag nanoclusters supported on TiO$_2$ substrate are covered with a thin layer of rutile, and this provides a valuable system to test the enhanced efficiency of photocatalytic reactions. When nanoclusters are located within the titania dielectric, their absorption bands shift and broaden due to the dielectric response of the matrix, matching a wider range of the solar spectrum, and this is key to enhancing efficiency. As efficient photoabsorbers in the near surface region, they can generate photoexcited e$^-$ h$^+$ pairs near the active surface sites and more efficiently deliver charge to the reaction. This provides a competitive advantage over bulk doped titania where e$^-$ h$^+$ pair production within the bulk can be quenched through recombination before the carriers can reach the surface. Another advantage of this structure is to prolong the lifetime of catalysts. Unprotected, however, these nanoclusters would quickly degrade in an electrochemical environment. By coating with a nanometer thin layer of TiO$_2$, which is stable in an electrolyte, we can protect these nanoclusters from oxidizing radicals and produce a functionalized titania surface that incorporates these nanoscale "antennas" to absorb solar radiation. The excited carriers produced by the strong fields near these clusters[103] are generated in close proximity to the sites for water cleavage, enhancing the efficiency of the photoelectrochemical cell.

H. Freund recently reviewed the structure and optical properties of clusters adsorbed on insulating surfaces [104]. It is well-known that the optical properties of metal clusters, such as those in stained glass, arise from plasmon excitations, giving rise to characteristic colors. Although plasmon energies of many bulk metals are not necessarily well-defined due to interband transitions that quickly damp them, they are well defined in nanoclusters. In nanoclusters, the classical Mie resonance [105] gives way to quantized behavior due to quantum confinement within the cluster. The plasmon
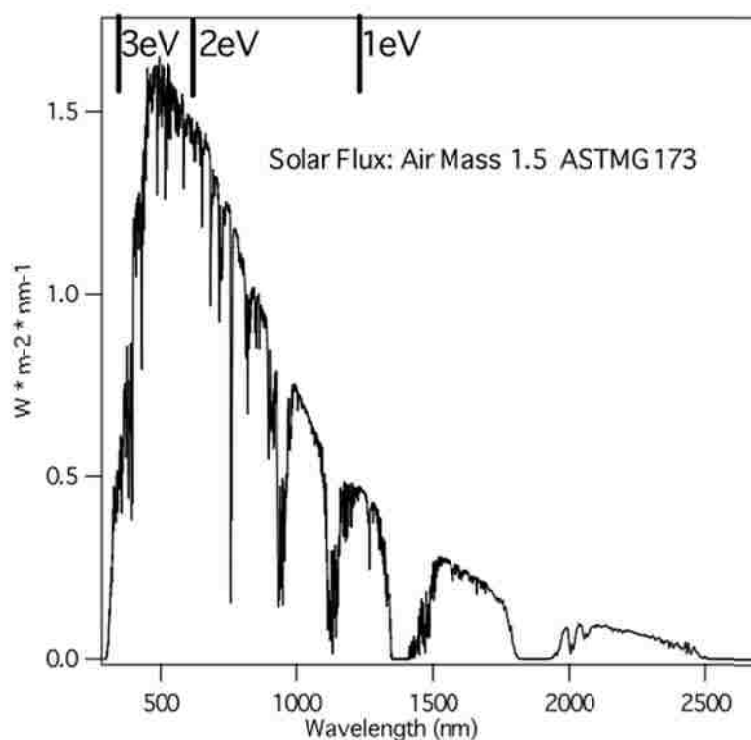
Fig. 4.1 Reference solar spectral irradiance at Air Mass 1.5 [97] Since the bandgap of TiO_2 is 3.2eV it will only absorb the fraction of spectrum that is above 3.2eV
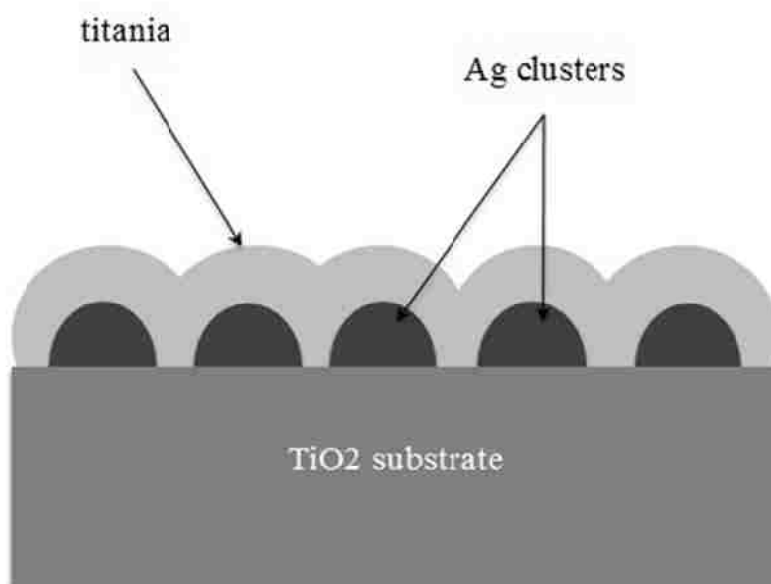

Fig. 4.2 Structure studied in this work: Ag nanoclusters grown on a $TiO_2(110)$ substrate buried beneath a nm-thick coating of titania

resonance of individual oxide-supported metal clusters has been systematically studied by Freund using electron-stimulated photon emission [104, 106-108]. Ag clusters on Al_2O_3, excited with tunneling electrons from an STM show light emission at bulk plasmon energy of ~3.75 eV with cluster size of ~3nm. The photon energy shows a redshift to ~3.5eV when cluster size increases to ~10nm. On TiO_2 surface, the photon emission spectra of Ag clusters have very similar behaviors, although the photon energy is slighter lower than that on Al_2O_3. The relatively small dependence of plasmon resonance energy on cluster size, however, has motivated our investigation to study the potential of tuning the resonance by embedding within the dielectric, semiconducting matrix of defective titania.

As a byproduct of encapsulation, we anticipate that defect densities will be strongly enhanced nearby the clusters, and we investigate the impact of this on potential band-bending and charge separation. The nature of the defect sites near these nanoclusters are key to band-bending and efficient charge transfer, and they play a significant role in establishing the band-matching conditions required to match the electrolyte couple [109, 110]. We control and study the nature of these defects by varying the growth techniques applied as well as the associated kinetics. The first approach involves physical deposition using vacuum-based techniques for film growth (MBE, magnetron sputter-deposition, PLD) and the second is electrochemical. Both methods have proven to be able to produce co-deposited metallic and oxide components and we are working to refine methods for the current application. A better fundamental understanding of physical, chemical, and catalytic properties of the buried nanoclusters will be elucidated using surface and materials-analysis, synchrotron-based spectroscopies, and electrochemical techniques.

In this work we focus on the noble-metal Ag, which does not easily oxidize and readily forms clusters on TiO_2 [12]. In this model study, we will use single-crystal $TiO_2(110)$ as the substrate for arrays of Ag nanoclusters [111]. A thin rutile layer will be grown on top of Ag nanoclusters via evaporation of Ti in oxygen ambient and annealed under conditions that leave the noble-metal clusters intact. This allows us to separate the direct catalytic activity of the noble metal cluster from the effects

due to the photoexcited carriers that are generated near the surface. The thickness of coating and defect sites within it will be active areas of our investigation as we progress from the limit of nearly bare nanoclusters to thicker rutile coatings.

4.2 Experiment

Ag nanoclusters were grown on $TiO_2(110)$ in an ultra-high vacuum (UHV) chamber with a base pressure of 1×10^{-10} Torr. The $TiO_2(110)$ crystal was cleaned by successive cycles of sputtering at 5×10^{-5} Torr with 1.5 keV Ne followed by vacuum annealing to 600°C. This treatment resulted in a surface with varies kinds of defects such as bridging oxygen (O_{br}) vacancies and sub-stoichiometric TiO_2 strands. Oxygen exposure is effective for healing the surface O_{br} vacancies but subsurface Ti interstitials were not removed by room-temperature O_2 exposure [23]. Ag was deposited at ~1×10^{-9} Torr at room-temperature on $TiO_2(110)$ surface using a simple thermal evaporator consisting of a W filament wrapped with Ag wire. The W filament was kept at 500°C when not evaporating to maintain cleanliness and minimize outgassing. Ti was deposited from an e-beam heated rod evaporator with an integral flux monitor. The chemical composition and long range structure of the surface were checked with Auger electron spectroscopy (AES) and Low energy electron diffraction (LEED) respectively, before we went on with further measurements.

Scanning-tunneling microscopy (STM) was performed using an Aarhus-type STM [112] and an Omicron VT STM using W tips. Atomic force microscopy (AFM) was performed in Dr. Sunggook Park's lab at Louisiana State University. By using STM and AFM, we tried to investigate the morphology of the nanoclusters and verify that the clusters retain their identity following encapsulation. High-resolution electron energy loss spectroscopy (EELS) was performed in an electron spectrometer manufactured by LK Technology [113]. Primary electron beam energies varied from ~6-30 eV and spectra were taken with energy resolution of 5-15 meV as determined from the full width at half

maximum (FWHW) of the primary elastically-scattered peak. EELS measurements have been used to characterize vibrational excitations, as well as to extract electronic excitations.

4.3 STM and AFM Results

Fig. 4.3 shows STM images of a clean $TiO_2(110)$ surface. These images were obtained in constant-current mode from surfaces that have been prepared as indicated above. In Fig. 4.3(a) we show a 50×50 nm^2 scan showing terraces of $TiO_2(110)$ with a variety of defects. As indicated near the center of Fig. 4.3(a) with a circle, the terraces are decorated with a number of chains of a TiO_x (x<2) sub-oxide that terminates in an oxide cluster. Note that these surfaces are clean as determined by Auger spectroscopy, containing only Ti and O so that the chains and clusters are titania [114]. Fig. 4.3(b) shows a 7×7 nm^2 scan giving much better details and atomically resolving several types of defects. The bright rows in this image are 5-fold coordinated Ti atoms and the dark rows are the bridging-O atoms on top of 6-fold coordinated Ti atoms. The chain of TiO_x sub-oxide extending from the upper terrace ends in a cluster. A recent combination of STM and density-functional theoretical calculations indicate that the nominal composition of the cluster is TiO_2 [115]. Fig. 4.3(b) also shows two other recognizable defects indicated by the arrows. The black arrow shows a bright spot on the dark row, identified as an O_{br} vacancy. This leaves two of the underlying Ti under-coordinated and the charge localized in this area gives a larger tunneling current. Several others of these point defects are visible. The white arrow shows a dark region in the bright row and the origin of it is still not clear. The dark feature is less common on the surface, and was tentatively ascribed to sub-surface oxygen vacancy [116], but theoretical studies indicated that it is less likely the case [12]. Another potential candidate is an adsorbed hydroxyl radical, OH$^-$. Ultimately our interest is to understand the role that these and other defects play in the interaction of H_2O with the surface.
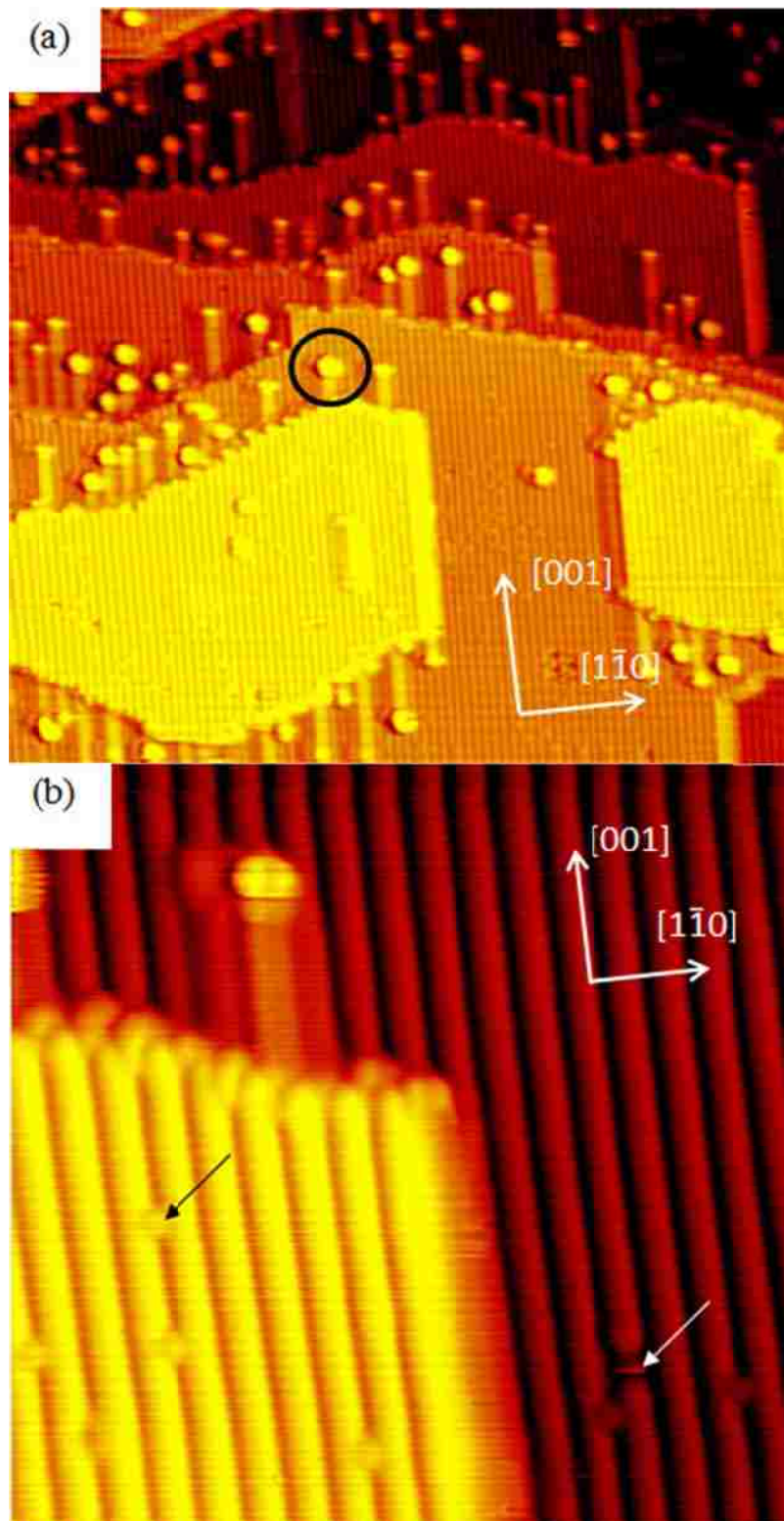
Fig. 4.3 STM images of TiO$_2$(110) that has been sputtered and annealed showing several different kinds of defects (a) 50nm×50nm (b) 7nm×7nm
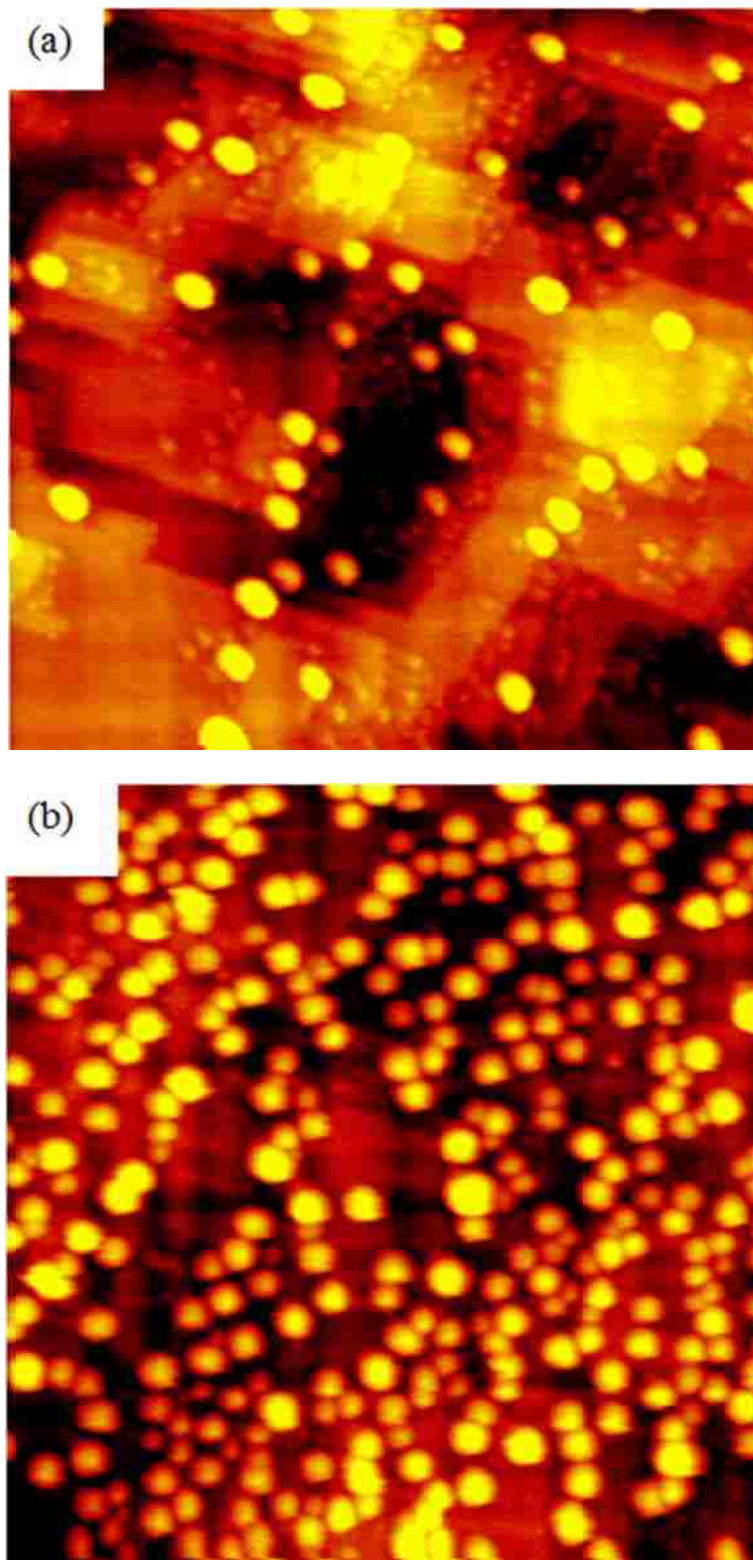
Fig. 4.4 (a) ~0.3ML Ag on TiO$_2$(110) produces nanoclusters that are ~5.5 nm wide by ~2 nm high and (b) ~3 ML Ag on TiO$_2$(110) produces a distribution of clusters that do not coalesce. Both images are 100nm×100nm
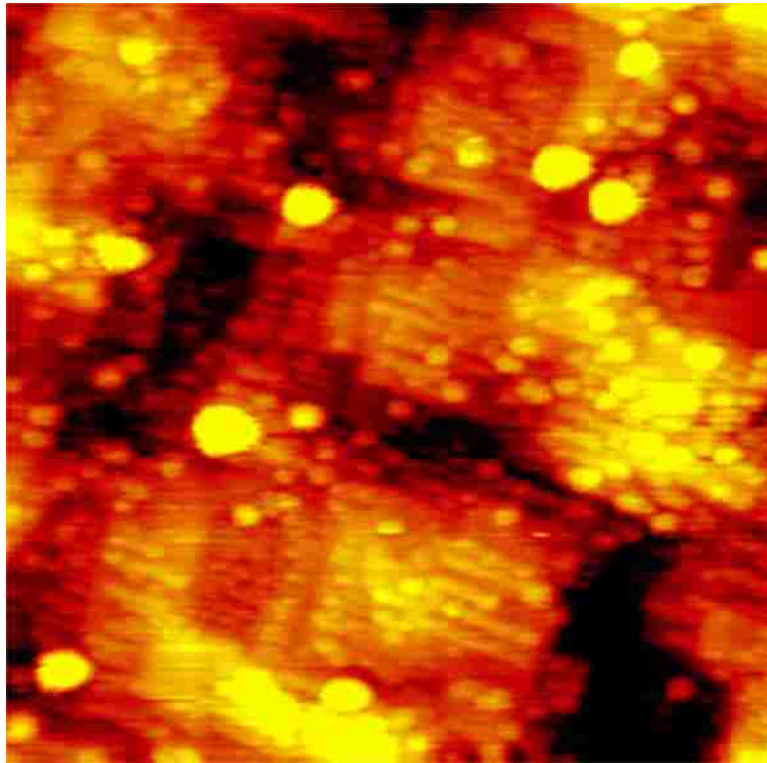
Fig. 4.5 STM image of Ti/~0.3ML Ag/TiO$_2$(110), 100nm×100nm

In Fig. 4.4(a) we present a 100×100 nm scan following deposition of ~0.3 monolayer (ML) of Ag on TiO$_2$(110) in UHV chamber at room temperature. We note that the Ag spontaneously forms clusters of ~5nm across and ~2nm high, minimizing its surface free energy. The nanoclusters appear to preferentially decorate step edges and kink sites. Additional deposition of Ag giving ~3ML equivalent coverage results in the array of nanoclusters shown in Fig. 4.4(b). The clusters are not significantly bigger than that at low coverage, but spread over the flat terraces. Close inspection of the images between the nanoclusters show that the characteristic rows in TiO$_2$(110), such as those in Fig. 4.3(b), remain unperturbed by the addition of Ag clusters. This indicates very weak interaction between Ag clusters and TiO$_2$(110) substrate.

As stated above, our goal is to cover the Ag nanoclusters with a thin layer of titania on top, and we tried two different ways to grow this titania layer. The first method is Ti deposition followed by

oxygen annealing. The second method is to deposit Ti in oxygen atmosphere at elevated temperature. These two methods gave us very similar surface structure, but the degree of Ti oxidation might be different, so the sample preparation process is likely to be crucial in determining the density of surface defects. Fig. 4.5 shows the STM image of Ti deposition on ~0.3ML Ag on TiO_2(110). Compared to the Ag clusters in Fig. 4.4(a), the Ag clusters seem a little bigger, which might be due to the Ti coating on top. Apart from the Ag clusters, the whole surface is covered with bright strands, which we believe are TiO_x(x<2) sub-oxide species.

The chemical composition of the surface was determined with Auger electron spectroscopy. Auger data in Fig. 4.6 shows that there is some alloying of the Ti and Ag. Fig. 4.6(a) shows the Auger data for ~3ML Ag on the surface giving isolated nanoclusters. The Ti:O:Ag intensity ratio is 1:1.9:1.87, which is normalized to the Ti peak at 387eV. Following a dose of ~3ML Ti, the ratio changes to 1:0.83:1.62 shown in Fig. 4.6(b). This shows that the O in the substrate is attenuated by 56% while the Ag is only attenuated by 13% after Ti deposition. If the Ti were to evenly coat the clusters and the substrate, the O and Ag should be attenuated by almost the same percentage. Since this is not the case, either the Ti is deposited only between clusters, which we believe is unlikely, or Ti and Ag are alloying, keeping a larger amount of Ag at the surface than would be expected without alloying. The two are known to alloy in the bulk but at the surface we expect that the much higher heat of formation of Ti oxides compared to Ag oxides will allow us to preferentially oxidize the Ti. This will be more likely if we start with a thin Ti film, and oxidize it to form a thin TiO_x layer that passivates the surface of the Ag clusters. Successive depositions of thin layer of Ti with subsequent oxidation allow us to grow thicker TiO_2 films. In this process, we tried to keep each deposition amount of Ti very low, in order to oxidize the Ti to a larger extent.

The TiO_x/Ag/TiO_2 sample obtained as described above has a rough and less conducting surface, and we did not have success using STM to image the surface, so we used atomic force microscopy (AFM) for imaging.
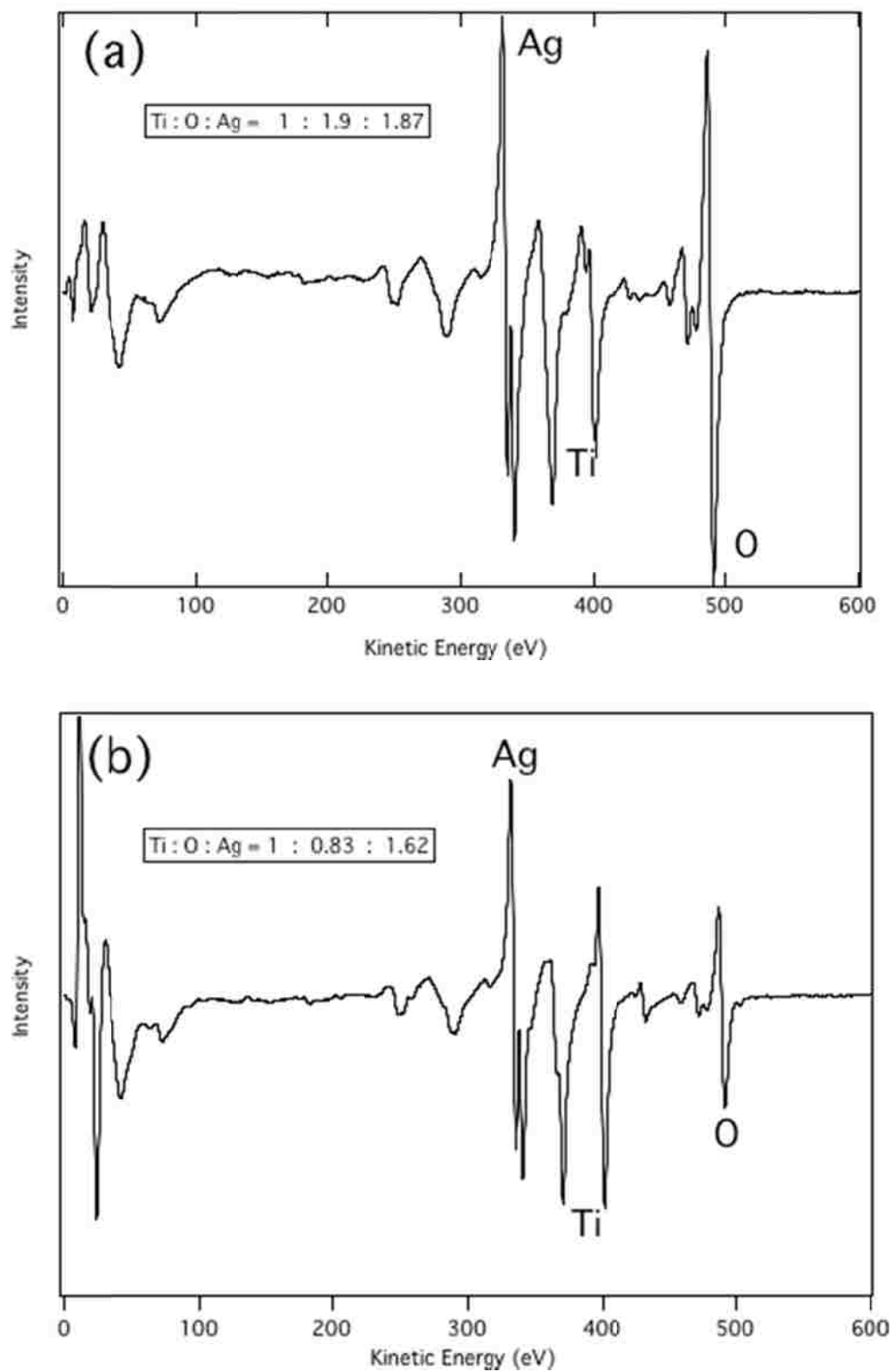
Fig. 4.6 Auger data from (a) $TiO_2(110)$ with 3 ML Ag producing a surface with nanoclusters and (b) following deposition of 3ML Ti
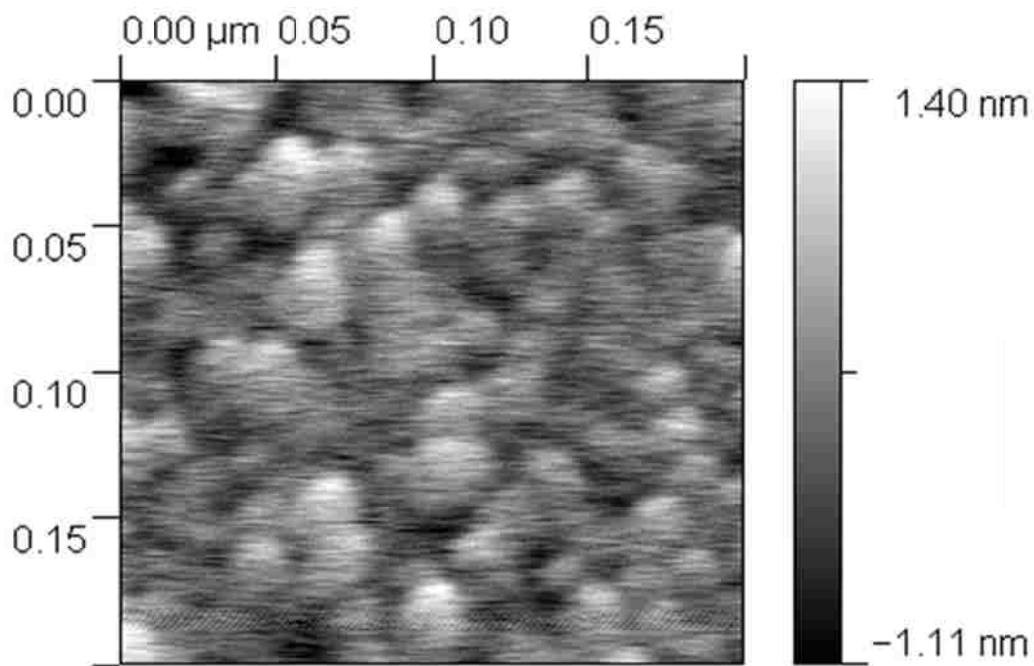
Fig. 4.7 Atomic force microscopy (AFM) image of $TiO_2(110)$ with Ag nanoclusters coated with TiO_x. This data suggests that the Ag nanoclusters retain their morphology following coating with a TiO_x overlayer. Height scale is in nm
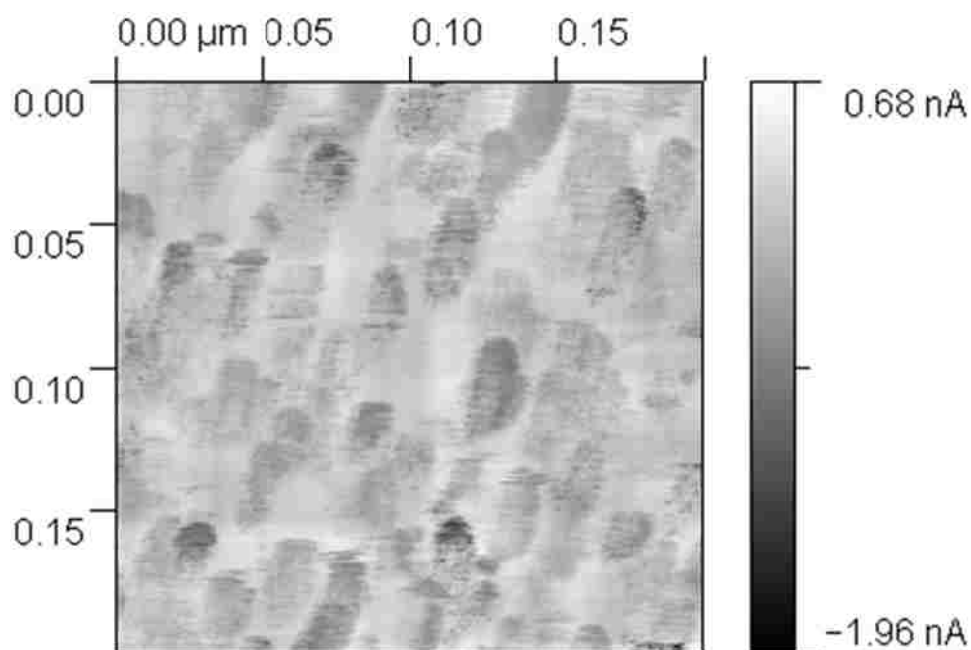
Fig. 4.8 Conductive-probe AFM image of $TiO_2(110)$ with Ag nanoclusters coated with TiO_x. The conductivity is larger in the regions near the clusters, consistent with metallic clusters surrounded by defective TiO_x, also more conductive than TiO_2. Current scale is in nm

Fig. 4.7 shows an AFM image acquired in air of a surface with ~3ML Ag nanoclusters that have been coated with TiO_x. The surface is very rough due to the exposure to air, and consistent with clusters that have been coated with an oxide layer. The size of the clusters ranges from ~5-20 nm indicating that either some cluster agglomeration occurred or that the overlayer of TiO_x spanned over multiple clusters forming an overcoat that filled in between clusters. The corrugation of clusters in the AFM image is ~2-3nm, which is about the same as that in STM studies. In Fig. 4.8 we present a conductive-probe image of the same surface. This measurement uses the AFM to acquire a constant-height measurement while at the same time measuring the conductivity of the surface through the tunneling current to the tip. From this image it is clearly evident that a larger negative conductivity is observed in the regions of the clusters and a significantly reduced current in the regions between clusters. This is consistent with the notion that the Ag clusters retain their metallic nature following coating. Furthermore, we expect that the oxide coating at the cluster surface is highly defective, resulting in states within the bandgap and enhancing the conductivity of the oxide. At regions between the clusters, the oxide is more likely to approach stoichiometry and therefore is more insulating.

4.4 EELS and Optical Measurements Results

Fig. 4.9 presents high-resolution electron energy loss spectroscopy (EELS) spectra from clean $TiO_2(110)$ and from a $TiO_2(110)$ surface that has ~3ML equivalent of Ag on top, producing adsorbed nanoclusters. The energy loss range is from 0-350meV and probes the Fuchs-Kliewer phonon modes of the oxide lattice [113]. The primary energy is 30eV and a resolution of ±20meV is obtained. The spectra are normalized to the specular inelastic peak to give simple comparison of shapes.

The key observation of this data set is that although there is an overall reduction in intensity with the addition of Ag clusters, as seen by the reduced signal to noise, the shape of the phonon losses remains unchanged by the addition of the clusters. This is another means that suggests that the bonding of Ag clusters to the surface is weak and the perturbation of the underlying $TiO_2(110)$ is minimal. Note

that the reduction in signal to noise is due to the reduced amount of $TiO_2(110)$ surface area exposed

after the adsorption of Ag and increased scattering from the clusters, reducing the overall intensity.
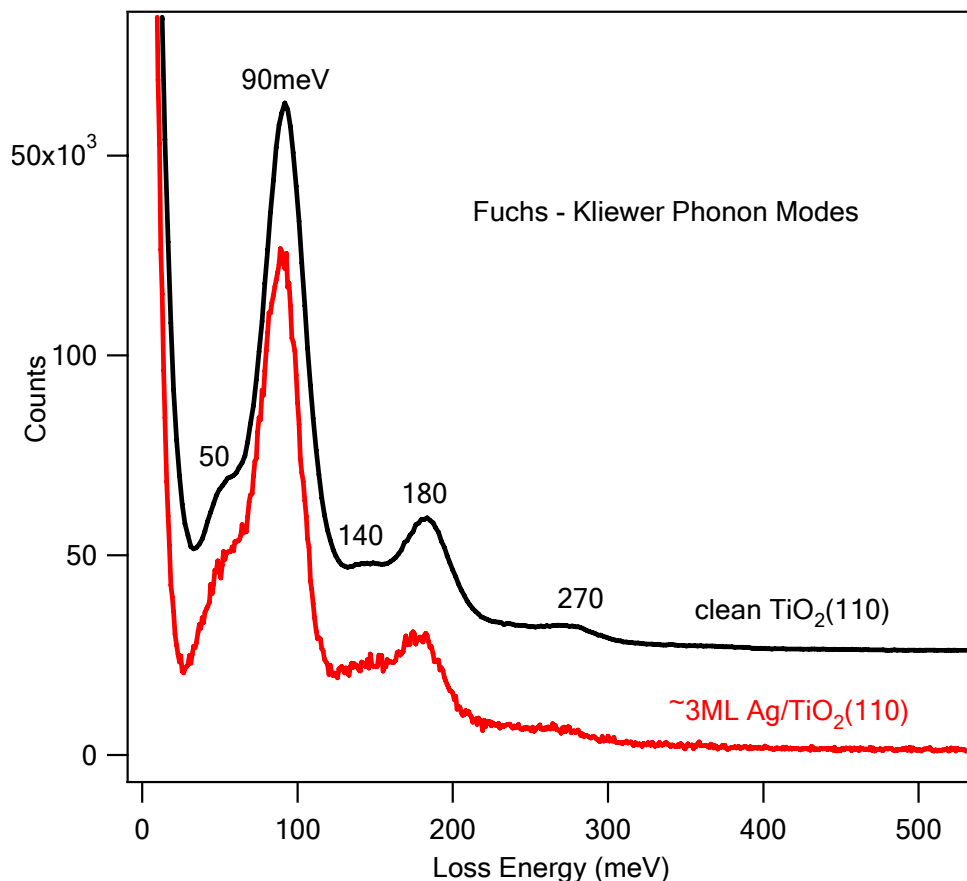
Fig. 4.9 High-resolution electron energy loss (EELS) showing vibrational modes from $TiO_2(110)$, top curve, and $TiO_2(110)$ with 3 ML Ag producing a surface with nanoclusters. The red curve has been scaled up in order to better visualize the loss features

Fig. 4.10 presents a series of spectra of relevant EELS experiments on burying Ag nanoclusters

within a TiO_x matrix on $TiO_2(110)$ substrate, with an emphasis on the electronic transitions. We call

the TiO_x matrix, for $x \leq 2$, titania to include potential sub-oxides of Ti. Taken in specular scattering

from the surface, EELS essentially measures the optical absorption and is sensitive to the first several

monolayers of the surface. The bottom curve, Fig. 4.10(a) shows the EELS spectrum from clean

$TiO_2(110)$ in specular scattering. For energy losses above 3eV, we can see that there is enhanced loss

intensity, indicative of interband transitions within TiO_2, and the 3eV onset energy corresponds to the bandgap of TiO_2. At energies below ~1.5eV, we also see strong loss features that are associated with the defects indicated in Fig. 4.10(a). These defects which include sub-oxides of TiO_2 are known to involve a new state appearing at a binding energy of 0.85 eV within the bandgap in photoemission spectroscopy measurements. There are multiple origins of this state, including an electron trapped in an O^{2-} surface vacancy point defect, interstitial Ti located near the subsurface region, and the sub-oxide strands mentioned above.

When ~3ML Ag is deposited onto the $TiO_2(110)$ surface, the EELS spectrum changes dramatically as shown in Fig. 4.10(b). The loss due to interband transitions starting at ~3eV is still present but there is a strong new loss feature which clearly peaks at 3.7eV. Concurrent with the growth of this new feature, there is a dramatic loss of intensity in the region below 1.5eV, indicating that the defect state losses are quenched by the addition of Ag nanoclusters to the surface. This is most easily explained if the defect losses are primarily due to surface O point vacancy defects.

In this case Ag nanoclusters interact with the defects, pulling the excess charge to the cluster and quenching the losses. We have photoemission evidence, not shown here, that this is indeed the case as the electronic states of the first ML of Ag occur at a lower binding energy than they do for successive layers. The 3.7eV loss is identified as a plasmon excitation of the nanoclusters, very similar to the Mie resonance observed for free Ag clusters and the surface plasmon of single-crystal Ag. This is also close to the surface plasmon energy of Ag that occurs at 3.7eV at the zone center, on Ag(111) [117]. Since we are interested in investigating the behavior of these clusters when encapsulated in a layer of TiO_x (where x≤2), we have grown TiO_x/Ag clusters/$TiO_2(110)$ by depositing elemental Ti from an e-beam heated evaporator and subsequently oxidizing the Ti. Fig. 4.10(c) shows the EELS data acquired after depositing 2ML Ti on the surface of Fig. 4.10(b). The Ag plasmon intensity is clearly attenuated. In Fig. 4.10(d) the result of oxidizing the 2ML Ti with a dose of 50L O_2 is shown. Several important observations can be made from this spectrum. First, the broad interband absorption characteristic of

72

TiO$_2$ is seen to return for energy losses above 4eV, as seen in Fig. 4.10(a). This suggests that additional oxide layer is formed on the surface, and presumably on the surface of the clusters. Second, the 3.7eV Ag plasmon peak also returns, suggesting that some of the Ag clusters are providing excitations unchanged from the bare clusters in Fig. 4.10(b).
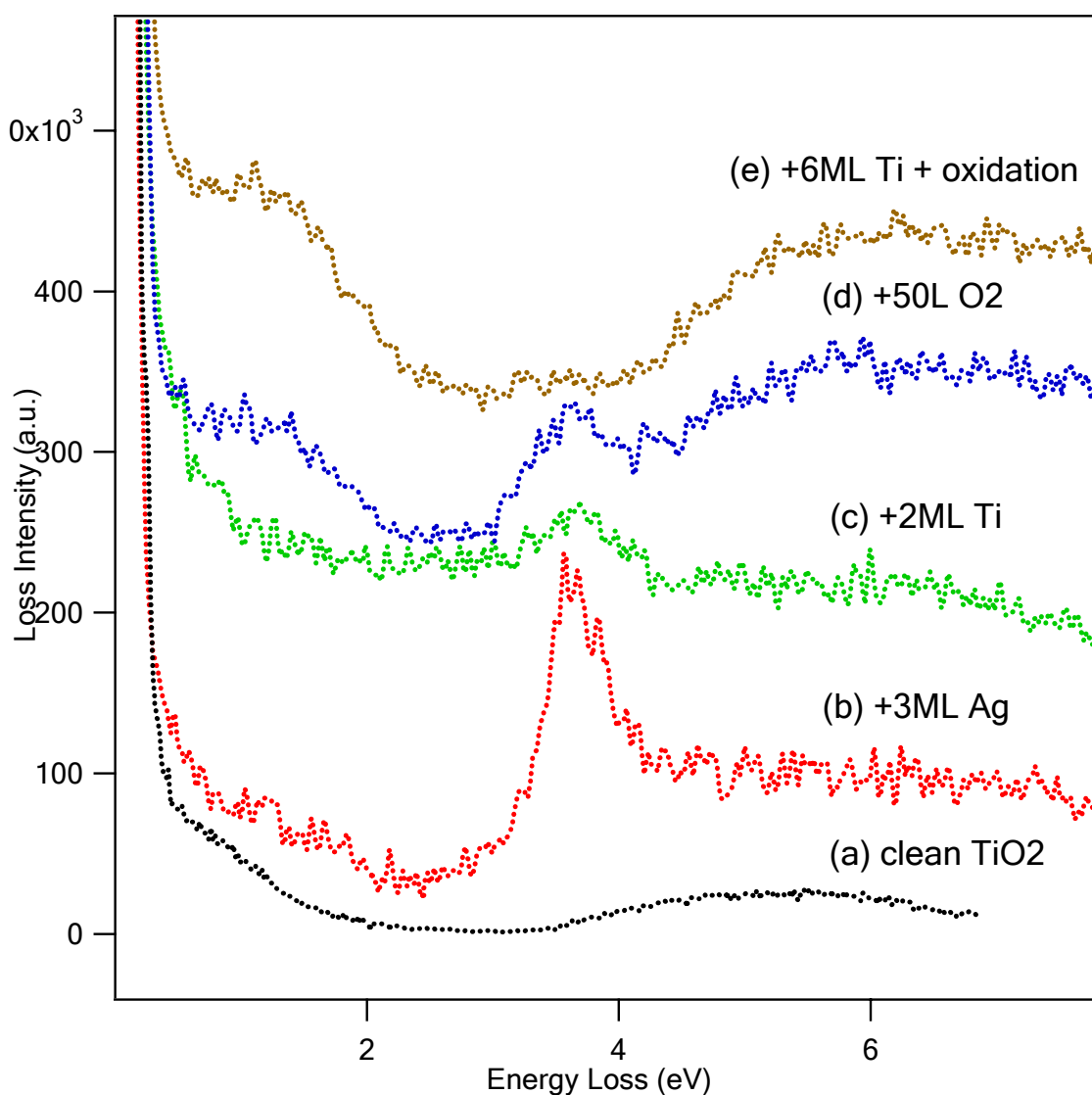

Fig. 4.10 Electron energy loss (EELS) showing electronic transitions from (a) TiO$_2$(110) (b) TiO$_2$(110) with 3ML Ag producing a surface with nanoclusters (c) the result of adding 2ML Ti on top of the Ag nanoclusters (d) subsequently partial oxidation of the Ti with 50L O$_2$ exposure at 450ºC and (e) addition of 4ML Ti and subsequent oxidation

This enhancement could arise from the de-alloying of Ti/Ag as the TiO_x oxide layer forms. Perhaps the most important observation of this spectrum is the enhanced intensity of losses producing a distinct, broad peak below 2eV. We propose that these losses are due to plasmon excitations of Ag clusters that are surrounded by a dielectric – the TiO_x matrix – but are also likely that some of these losses are due to excitations of defects within the TiO_x. Fig. 4.10(e) shows the spectrum that results following additional Ti dosing and oxidation. The 3.7eV plasmon is essentially removed from the spectrum and the losses between 1 and 2.5eV are substantially enhanced. The result of this surface treatment is an enhancement in optical excitations within the visible light region of the solar spectrum that provides the most intense radiation, accomplishing the first goal of this investigation.

Fig. 4.11 shows optical data taken in transmission measurements from $TiO_2(110)$, Ag nanoclusters on $TiO_2(110)$, and $TiO_x/Ag/TiO_2(110)$. Although we expect that transmission measurements will be insensitive to the very thin surface layers that we produce in this treatment, the films are visible by eye on the single crystal substrate. Fig. 4.11(a) shows the 3eV bandgap of bulk $TiO_2(110)$ with strong absorption of all light at energies exceeding 3eV. At energies below 3eV, optical interband excitations are not possible so that there is a significant transmission of light for 0–3eV. When Ag clusters are grown on the surface, shown in Fig. 4.11(b) with a 3ML Ag dose, the transmission is reduced and the region from 0–3eV shows a linear dependence on the transmission. Ag metal films have a nearly flat, 90-100% reflectivity in this region but this is not what we observe for these clusters in air [118]. In Fig. 4.11(c), we show the transmission following overcoating the Ag nanoclusters with TiO_x. The roughly flat transmission between 2 and 3eV returns, similar to the transmission of $TiO_2(110)$ but is a clear dip in the transmission, consistent with enhanced absorption in the region below 2eV, as shown in the difference spectrum in Fig. 4.11(d). This enhanced absorption is also consistent with the observations provided by the EELS data in Fig. 4.10. Since transmission measurements are sensitive to mostly bulk absorption properties, we have also made measurements in reflection for the nanoclusters encapsulated in TiO_x.
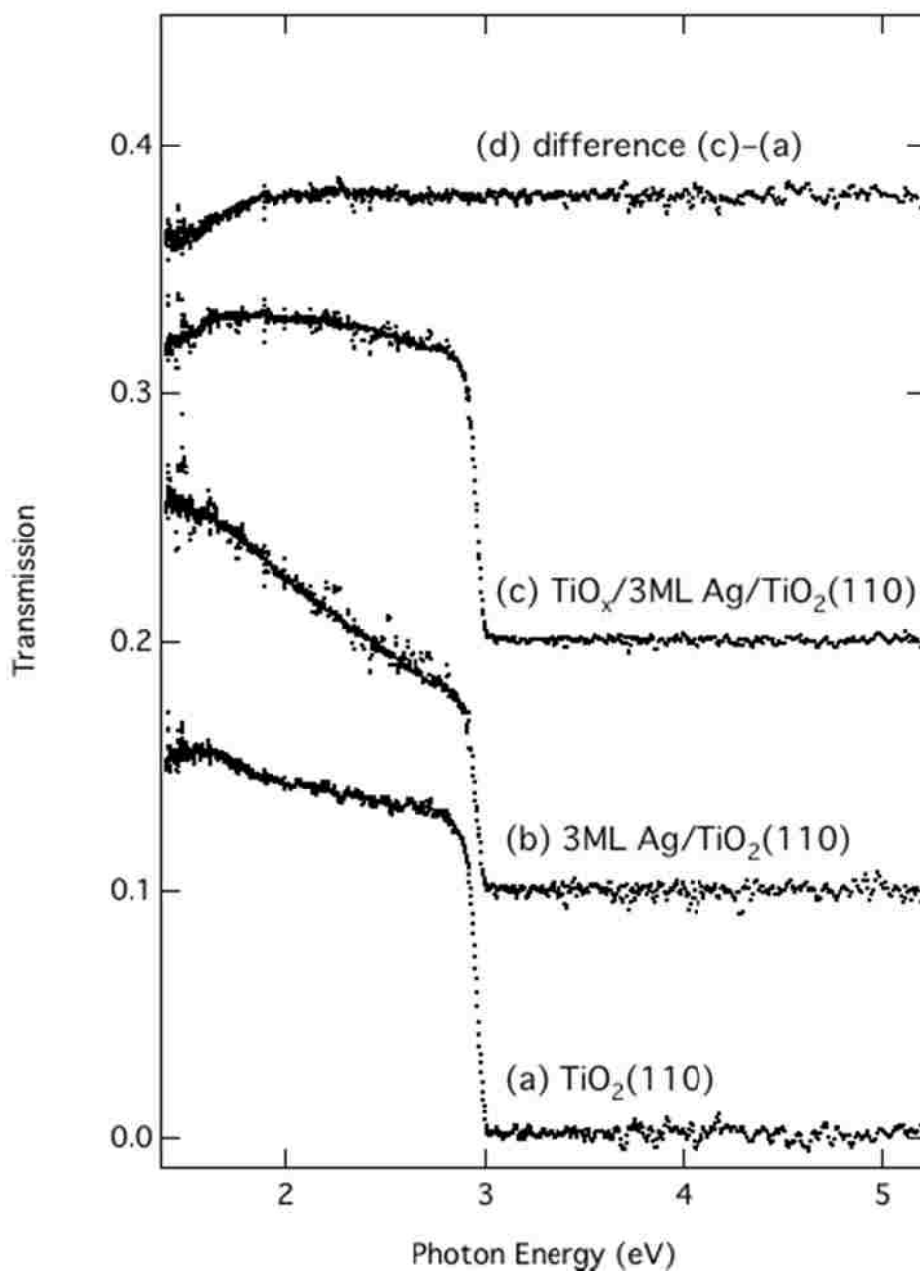
Fig. 4.11 Optical data taken in transmission from (a) $TiO_2(110)$ that was unreduced and transparent/yellow with the 3eV bandgap clearly evident. (b) 3ML Ag on $TiO_2(110)$ (c) $TiO_x/Ag/TiO_2(110)$. In (d) we present a difference spectrum highlighting the new absorption (decrease in transmission) that occurs between 1 and 2eV following TiO_x overcoating. Curves are offset for clarity
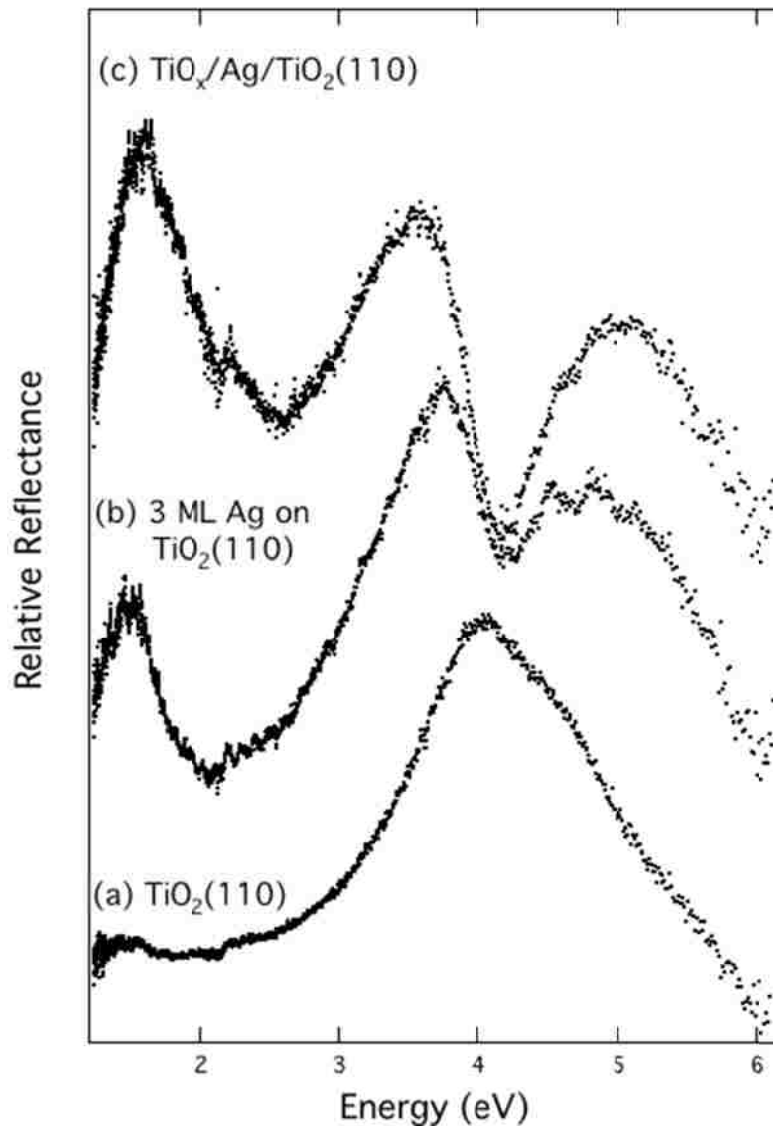
Fig. 4.12 Optical reflectivity from (a) TiO$_2$(110) (b) TiO$_2$(110) with 3ML Ag producing a surface with nanoclusters (c) the result of adding 5ML Ti on top of the Ag nanoclusters

Fig. 4.12 presents the data from these same surfaces, showing the effect on the reflectivity. Fig. 4.12(a) shows the reflectance of TiO$_2$(110) which exhibits a rise beginning at 2.5-3eV, a distinct maximum at 4eV and a decrease in reflectivity at higher photon energies. After Ag nanoclusters are deposited on the surface, the reflectivity changes dramatically as shown in Fig. 4.12(b). Two distinct peaks are found at 3.7eV and a second at 1.5eV. There is a very strong dip in reflectivity at 4.3eV, where the bare TiO$_2$ surface exhibited a maximum, and again rises at ~4.8eV. Following encapsulation

in TiO_x, the peak at 3.7eV shifts to ~3.6eV while the 1.5eV peak increases in intensity substantially and shifts slightly to ~1.6 eV. These data show that encapsulating the Ag nanoclusters within the TiO_x matrix has changed the optical response within the 1-3eV energy range relevant to solar-stimulated photochemistry. As mentioned previously, the reason for this change can be ascribed to several potential mechanisms and it is likely that more than one is in play. First, we expect that the response of the Ag nanoclusters to incident light will change when they are encapsulated in a dielectric medium such as titania [119]. Secondly, we expect that the oxide will have additional defects, particularly in the region surrounding the Ag nanoclusters and these defects will give rise to states within the 3eV bandgap of TiO_2, and give rise to additional optical excitation channels. Through the enhanced absorption, we have the potential for generating hot e^-–h^+ pairs to stimulate photochemistry with the added benefit that they are being created within nanometers of the surface.

In order for this material to be effective, band bending effects between the defective titania and the TiO_2 substrate will need to allow us to separate charges prior to recombination. It may be possible to tailor these properties through kinetic control of titania growth and subsequent defect densities and characters, or through layering different oxide films to induce band bending at the surface.

When light is incident on this buried Ag clusters/semiconductor matrix, some fraction will be reflected, some absorbed, and some transmitted. Neither the transmitted nor the bulk-absorbed light will be useful to stimulate surface chemistry. The reflected light is due to dielectric response of the electron gas within the nanoclusters, and at a particular frequency dependent on the charge density, a collective oscillation known as a plasmon can be excited. In general the reflectivity can be related to the electronic structure of the material [118]. In discussing the origin of the features in the optical data, we first note that bulk Ag exhibits an interband absorption spectrum with transitions beginning at about 4eV. This is associated with a very strong dip in the reflectivity at about the same energy [118]. The broadening of this peak, as seen in Fig. 4.12(c) has been anticipated previously [119] and is

thought to depend on the details of the chemical environment at the interface surrounding the cluster, and can depend on the polarization of the light [120].

The new peak that appears between 1-2eV is similar to the shifted plasmon that occurs for Ag nanoclusters embedded within a Si matrix [121, 122]. The details of the position of this peak, as well as the width, will depend on the local dielectric properties of the surrounding titania. Voids and defects will tend to decrease the dielectric response, giving a plasmon oscillation that is closer to the bare-surface value while improved encapsulation will tend to result in a larger red-shift into the solar spectrum. Since the surrounding oxide matrix is perturbed by the presence of the cluster, it will intrinsically be defective. The specifics of the densities of these defects will determine the details of the optical response.

Furthermore, these excitations have the potential for stimulating the production of e^-–h^+ pairs. The plasmon is essentially a collective electronic excitation of states near E_F, and this oscillation of charge can produce large local electric fields, particularly near regions of the cluster with a sharp radius of curvature [123-125]. These electric fields, in turn, can produce excitations of the substrate or within a surrounding matrix, and generate electron-hole pairs. Since the surrounding oxide is highly defective in the region of the clusters, the additional bandgap states associated with these defects are spatially localized in the region of these large electric fields.

Clearly the separation of these pairs within the semiconducting substrate will determine whether this mechanism can effectively drive surface chemistry. In principle, it may be possible to further tailor the optical absorption through thermal treatments during oxidation that result in specific interface configurations. This will be particularly important in determining the nature of the nearby semiconductor and whether the defects act more as sites for stimulating photochemistry or as traps for recombination and quenching.

4.5 Conclusions

We have undertaken a study to enhance photoelectrolysis of water using TiO_2 modified with buried metallic nanoclusters, a system that has the potential to address some of the roadblocks to solar photolysis. We have shown that by embedding Ag within a dielectric medium, we produce new excitations within the photon energy range relevant to solar photochemistry. Noble-metal clusters (Cu, Ag, Au) are known to be stable on TiO_2 and when nanoclusters are located within a dielectric, like titania, their absorption bands shift and broaden, matching a wide range of the solar spectrum. The morphology of the clusters has been studied with STM and their encapsulation has been observed with AFM and suggests that the clusters retain their identity following overgrowth of titania. The optical properties have been studied with EELS as well as optical reflection and transmission measurements and all three methods observe new excitations within the 1-3 eV range that is relevant for solar photochemistry.

Unprotected, these nanoclusters would quickly degrade in an electrochemical environment. By coating with a thin layer of TiO_2, we expect that it will protect these clusters from oxidizing radicals and produce a functionalized titania surface that incorporates these nanoscale "antennas" to absorb solar radiation. The excited carriers produced by the strong fields near these clusters are generated in close proximity to the sites for water cleavage, enhancing the efficiency of the photoelectrochemical cell. We are currently investigating the application of these functionalized surfaces with electrochemical studies to assess their performance under illumination.

Chapter 5: Cu and Cu Oxide Growth on ZnO(10$\bar{1}$0) and TiO$_2$(110) Surfaces

5.1 Introduction

Catalysis consisting of Cu supported on ZnO has been widely used in a variety of hydrogenation activities, especially methanol synthesis for the past several decades [126-129]. The catalytic processes are very complex, and there are many reactions and products involved. Many questions have to be answered and several issues are still hotly debated, such as the active sites of the catalysts, the roles that metal and support play, the surface morphology and electronic structures of the systems. Various surface science techniques have been adopted to study the reaction mechanism, active sites, overall activity and product selectivity. In this work, the surface morphology of this class of catalysts is studied with Scanning Tunneling Microscopy (STM). The non-polar ZnO(10$\bar{1}$0) surface has been extensively studied and was chosen as the catalyst support. In addition to metallic Cu metal catalysts, a recent electrochemical reaction study [30] shows that Cu(I) species (Cu$_2$O) may play a critical role in product selectivity and can lead to high methanol yield. Both Cu and Cu oxides are found to be dispersed as nanoclusters on the substrate, and Cu oxidation can occur on ZnO surface upon annealing even in the absence of additional oxygen.

In addition to Cu/ZnO catalysts, two other systems Cu/TiO$_2$ and Au/ZnO have been studied in comparison to the main focus on Cu/ZnO catalyst. Both Cu/TiO$_2$ and Au/ZnO are also popular catalysts in hydrogenation of CO$_2$ to methanol [62, 130-134], but STM studies show very different growth behaviors compared to Cu/ZnO.

5.2 Experiment

Experiments in this chapter were performed in an ultra-high vacuum chamber with a base pressure of 2×10^{-10} Torr. This chamber is equipped with sputter gun, LEED, thermal Au evaporator, e-beam Cu evaporator, and an Omicron VT STM. ZnO($10\bar{1}0$) and TiO$_2$(110) single crystals with one side polished were purchased from commercial vendors. Sample surfaces were cleaned by cycles of Ne ion sputtering and vacuum annealing to 600˚C. The surface roughness was checked with LEED before we performed STM measurements. Clear and sharp (1×1) LEED patterns were observed for both ZnO($10\bar{1}0$) and TiO$_2$(110) surfaces after sputtering and annealing. Cu was deposited onto the surface using an e-beam evaporator. In the e-beam evaporator, an ultra-pure Cu rod was heated with one loop of tungsten wire filament around it. The Cu rod was biased to several hundred volts for electron bombardment, thus we could obtain higher temperature with relatively low filament current. Au deposition was accomplished with a simple thermal evaporator, in which ultra-high pure Au wire was wrapped with tungsten filament. Before deposition, all evaporators were fully outgassed, and filaments were kept at a lower temperature than the evaporation temperature. By doing this, we could assure the Cu/Au evaporated was clean and without contamination. STM measurements were performed at room temperature with a tungsten tip. Tunneling voltages and currents were set in the range of 0.5-3V and 0.3-1.5nA respectively, depending on the surface conditions.

5.3 Cu on ZnO($10\bar{1}0$)

5.3.1 STM Studies

Fig. 5.1 shows the ball and stick model of ZnO($10\bar{1}0$) surface. This non-polar surface has Zn-O dimer rows running along the [$1\bar{2}10$] direction. Fig. 5.2 shows the STM image of clean ZnO($10\bar{1}0$) surface prepared by cycles of Ne ion sputtering and vacuum annealing at 600˚C. The surface shows

some big flat terraces of different heights, with two major steps along [1$\bar{2}$10] and [0001] directions. Line profile indicates that the typical height of one step is 2.9Å, which is about the same as the vertical separation of two Zn-O planes (2.8Å) [29, 135]. We tried to resolve the Zn and O atoms but were unable to achieve it. Diebold [29] successfully resolved Zn and O rows as alternating bright and dark rows, however, true atomic resolution of single atom was not achieved either.
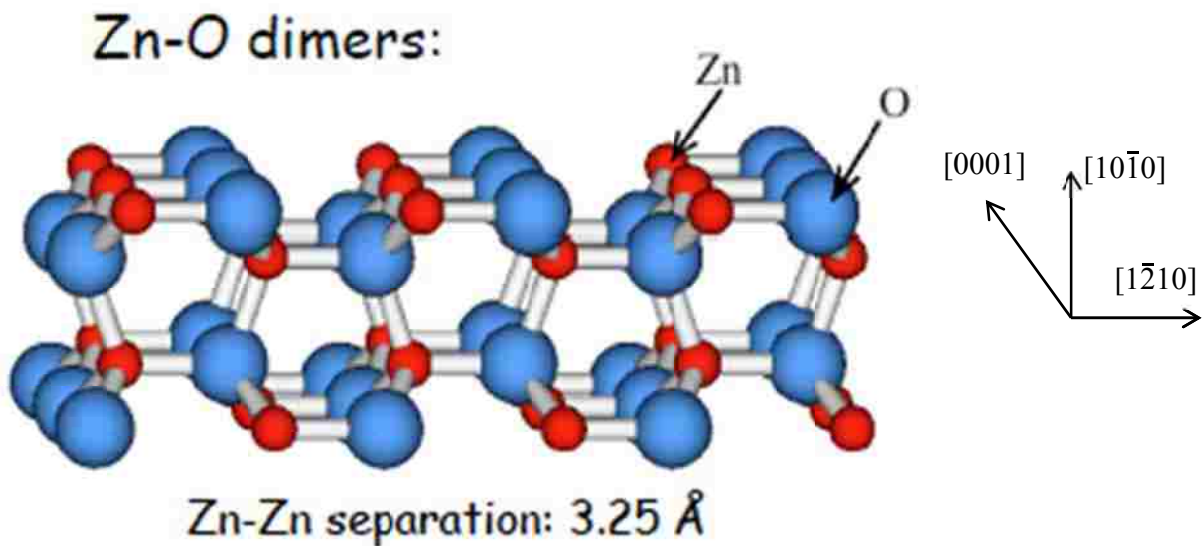
Fig. 5.1 Ball and Stick model of ZnO(10$\bar{1}$0) surface, small red balls represent Zn atoms, while big blue balls are O atoms (Courtesy of U. Diebold)

Fig. 5.3 shows the STM image of 0.2ML Cu deposited on ZnO(10$\bar{1}$0) surface at room temperature. It is clearly seen that 3D cluster growth mode (Vollmer-Weber growth mode) is adopted for very low Cu coverage at room temperature. In contrast, at 130K, Cu was reported to grow as a 2D film on the ZnO(000$\bar{1}$)-O polar surface until it covers a certain critical portion of the surface area, and subsequent annealing was found to cause clustering of Cu atoms [136].

82

Fig. 5.2 STM image of clean ZnO(10$\bar{1}$0) surface, line profile indicates the height of one step is ~ 3Å

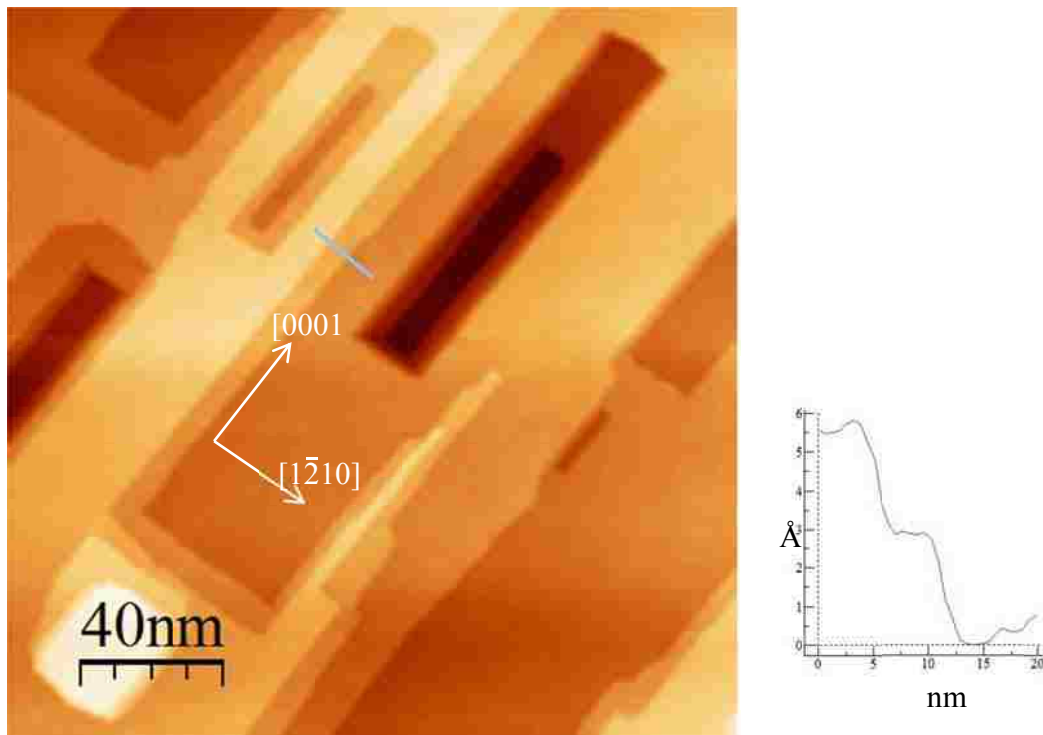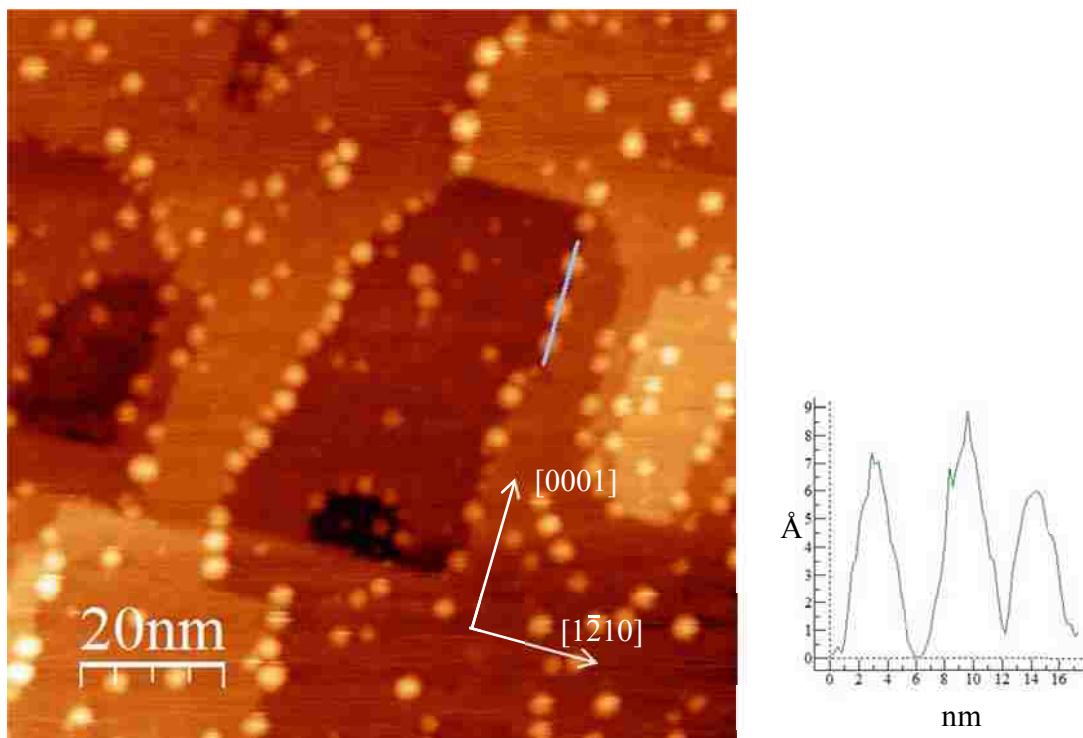Fig. 5.3 STM image of 0.2ML Cu on ZnO(10$\bar{1}$0) surface at RT, 3D clusters mainly decorate the step edges that are perpendicular to the [1$\bar{2}$10] direction

In Fig. 5.3, the most important observation is the preferential nucleation of Cu clusters at step edges, but not all the step edges are equivalent for Cu growth. As we see, most of the Cu clusters are located on the step edges cutting across the $[1\bar{2}10]$ direction, while almost no Cu clusters can be seen on the step edges along $[1\bar{2}10]$ direction. From the ball and stick model shown above, we know that the Zn-O dimer rows are oriented along the $[1\bar{2}10]$ direction. When Cu atoms are evaporated onto the surface, they will probably diffuse along Zn-O dimer rows and form clusters at step edges. The Zn or O rows are not preferred diffusion channels for Cu atoms. Besides the step edges being the most preferred nucleation sties, there are also some small clusters formed on the terraces. The $ZnO(10\bar{1}0)$ surface as prepared is near perfect, and surface defects are probably not the reason for cluster nucleation on terraces. Diebold explained the nucleation mechanism as the Cu atoms meet during the diffusion and then nucleate, forming a nucleation site on the terrace [29]. The line profile in Fig. 5.3 shows that most of the Cu clusters have a size of $\sim$ 5nm in diameter and $\sim$ 0.7nm in height. The 0.7nm height indicates that the clusters are mostly formed with two layers of Cu atoms.

To find out how the vacuum annealing affect Cu clusters, we annealed the sample to 400˚C and tried to image it in STM. Unfortunately, we encountered tip approach problems and could not perform scanning. This could be because the conductivity of the ZnO sample decreased drastically after annealing, and the tunneling current set-point could not be detected. We did not have this kind of problem with TiO_2, but for ZnO, this happened occasionally. Compared with TiO_2, ZnO has fewer surface defects and thus a lower conductivity, which might result in the tip approach problems in STM. It was reported that at very low coverage, small Cu clusters will agglomerate and form larger clusters upon annealing to 450˚C [29]. We were able to study the ripening of Cu clusters for higher coverage, as discussed next.
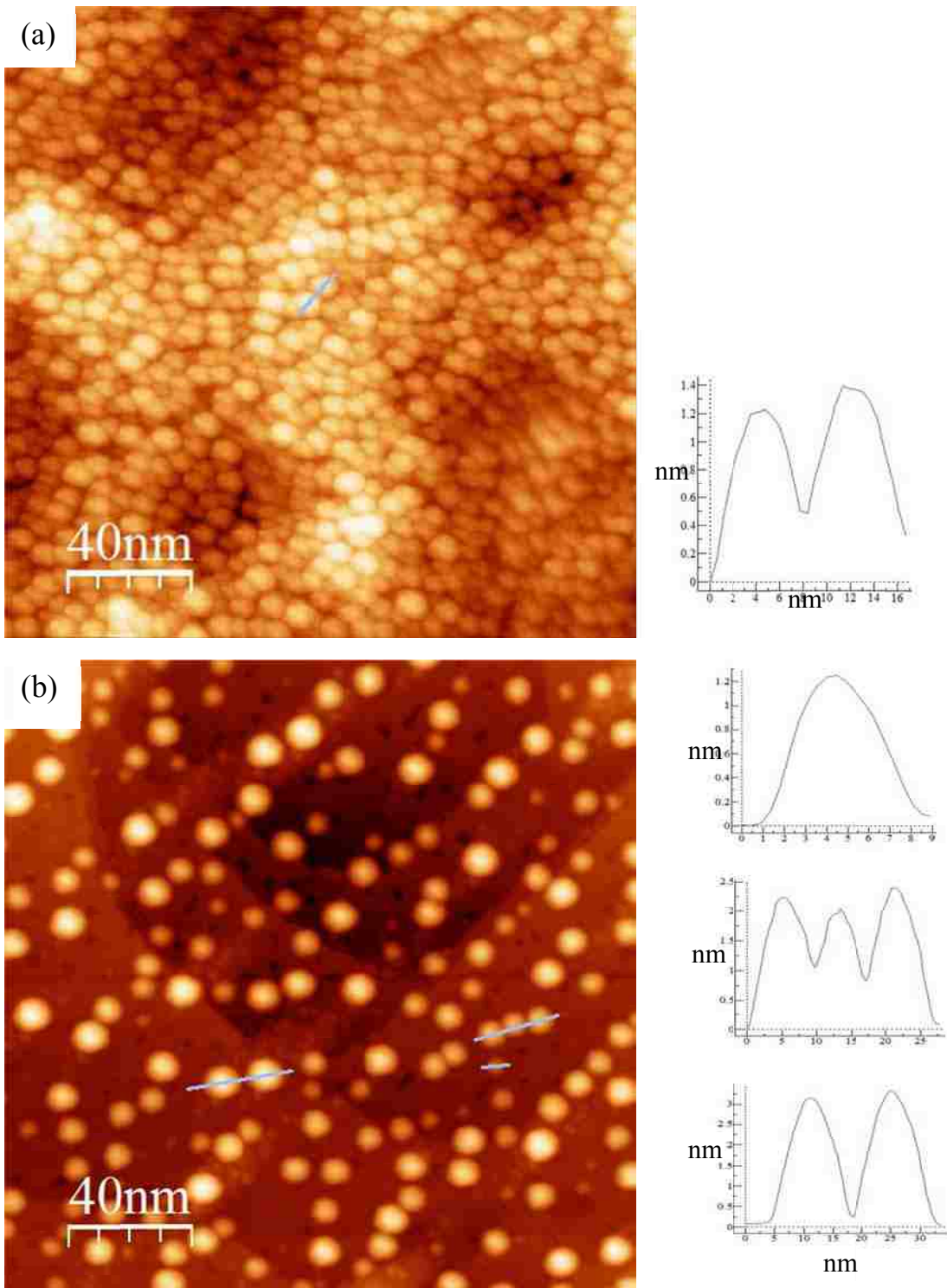
Fig. 5.4 (a) STM image of 2ML Cu/ZnO(10$\bar{1}$0) surface at RT (b) 2ML Cu/ZnO(10$\bar{1}$0) after 400°C anneal for 20min (c) small scale of STM image of 2ML Cu/ZnO(10$\bar{1}$0) after vacuum annealing showing the pits

85

(Fig. 5.4 continued)
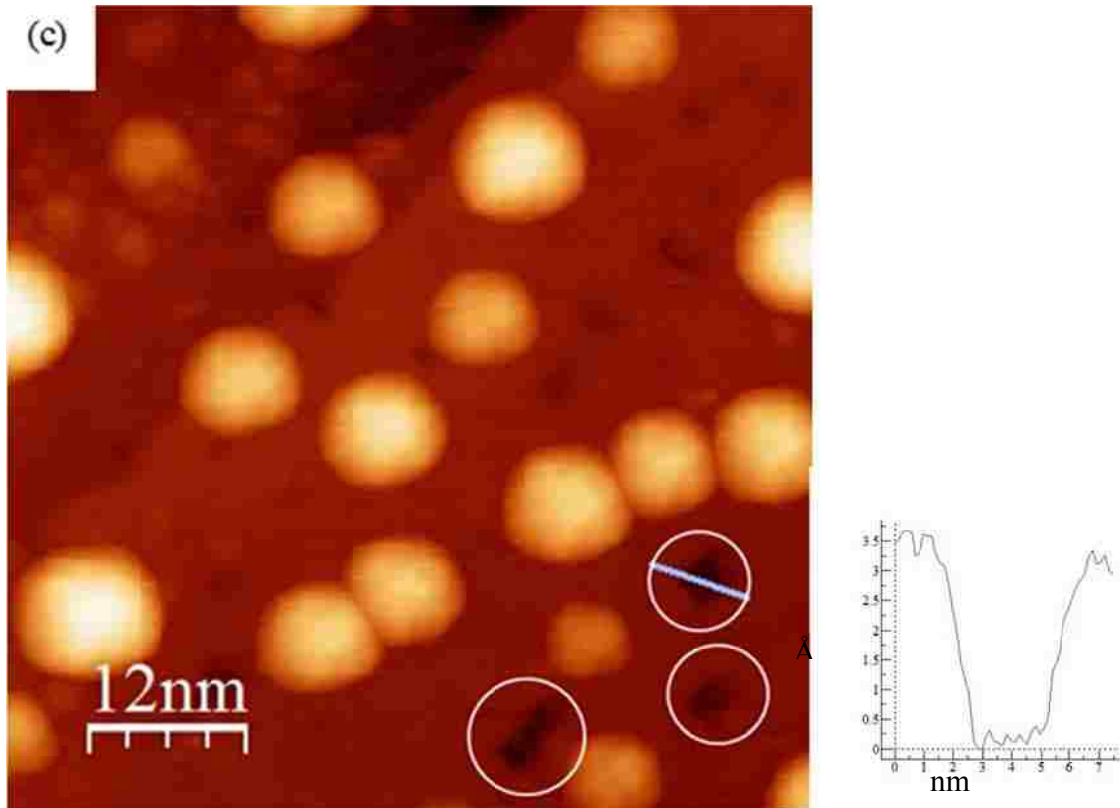
High coverage of Cu deposited on ZnO(10$\bar{1}$0) surface was also studied. Fig. 5.4(a) shows the STM image of 2ML Cu on ZnO(10$\bar{1}$0) at room temperature. From 0.2ML Cu to 2ML coverage, the biggest change in surface morphology is the number density of the clusters. The whole surface is completely covered with Cu clusters. Careful examination of the cluster sizes shows that the clusters did not grow much bigger. Thus at the present experimental parameters, there is a lack of ripening of the Cu clusters. As shown in the line profile, the larger Cu clusters have an average size of ~ 5nm in diameter and ~ 1.2nm in height. Compared to the clusters at 0.2ML coverage, the clusters did not grow in diameter significantly, but they did have one or two more layers of Cu atoms in height.

The 2ML Cu/ZnO($10\bar{1}0$) sample was annealed at 400˚C for 20min, and the STM image taken thereafter is shown in Fig. 5.4(b). Ripening of Cu clusters is clearly observed. After annealing, the small Cu clusters agglomerated to form much bigger Cu clusters, and the number density of clusters drastically decreased. The ripened clusters do not have uniform size. The largest clusters are ~ 15nm in diameter and ~ 3nm in height, the medium ones are ~ 10nm in diameter and ~ 2nm in height, and a few very small clusters can also been seen across the surface. These observations indicate weak interaction between Cu atoms and ZnO substrate, and suggest that Cu atoms have high mobility at high temperature. The existence of many small clusters suggests that the annealing temperature and time might still not be enough to allow the cluster sizes to fully ripen to their equilibrium dimensions.

Another interesting observation following annealing is the existence of many small pits in between the clusters, which appear as black spots. A careful look into these pits marked with white circles is shown in Fig. 5.4(c). Line profile shows these pits are ~ 3Å in depth, which is about the same as the height of one Zn-O layer. This indicates that after vacuum anneal, some Zn-O dimers are removed, leaving these dips in the surface. For clean ZnO($10\bar{1}0$) vacuum annealing may create some surface defects, but pits as large as those in Fig. 5.4(c) are not seen. This means the Cu clusters play an important role in changing the surface upon annealing. A possible scenario is that Cu atoms can react with O atoms on surface and be oxidized upon vacuum annealing, and this was suggested by a prior photoemission study [28]. The heat of formation for ZnO, CuO and Cu_2O are -348.0 kJ/mol, -155.2 kJ/mol and -166.7 kJ/mol respectively. ZnO does have a larger heat of formation than that of CuO and Cu_2O, but the values are for bulk oxides. At the surface, due to defects and step edges, the coordination of O atoms differs from that in the bulk, so Zn-O bonding may not be as strong as that in the bulk. Given some heat, it is possible that the Cu clusters can "steal" some O atoms from the substrate and be

oxidized. However, the pits indicate the removal of O atoms and Zn atoms at the same time, and we do not know with certainty where the Zn atoms go. It is possible that the under-coordinated Zn atoms produced in this manner can diffuse to other surface sites, but this cannot be confirmed with STM. To investigate the chemical reactions that are occurring on the Cu/ZnO surface upon annealing, photoemission and EELS measurements have also been performed, and these studies will be discussed later.
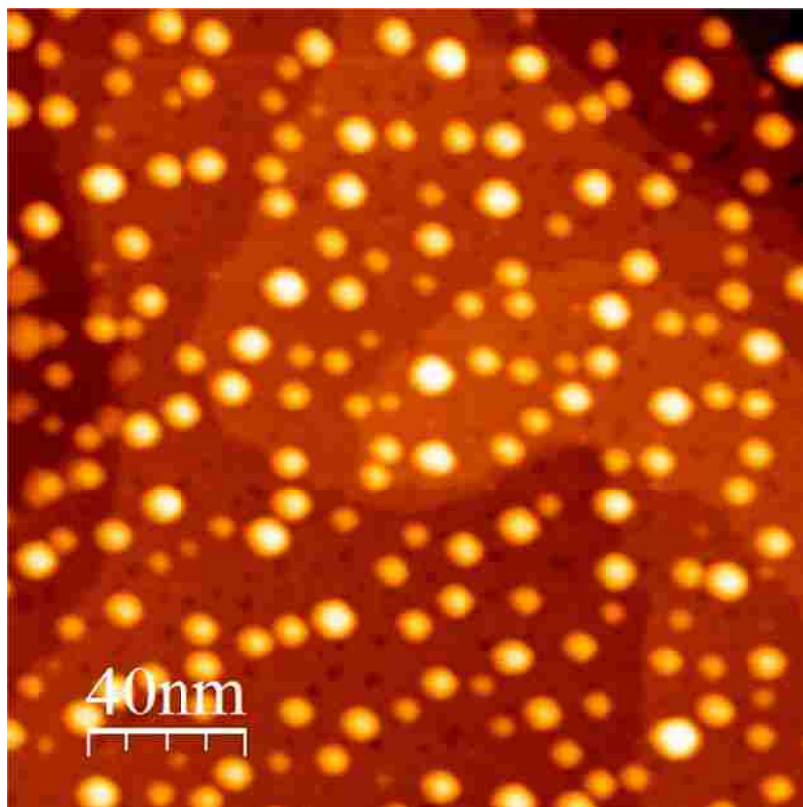
Fig. 5.5 Annealed 2ML Cu on ZnO($10\bar{1}0$) exposed to 2×10^{-7} Torr O_2 for 20min

The Cu clusters on the surface are likely to be partially oxidized upon vacuum annealing as suggested by the STM observation above. We also tried to study the effect of extra oxygen dosed to the Cu clusters. We exposed the pre-annealed 2ML Cu/ZnO($10\bar{1}0$) surface to 2×10^{-7} Torr O_2 for 20min

Fig. 5.6 (a) Pre-annealed 2ML Cu on ZnO($10\bar{1}0$) sample after annealing in 2×10^{-7} Torr O_2 for 20min and (b) enlarged images showing flat terraces with partially oxidized clusters and (c) regions with a rough substrate surface and elongated, irregular clusters

(corresponding to 240 Langmuir (L)) and took the STM image that is shown in Fig. 5.5. After this temperature O_2 treatment, we did not see any change. The Cu clusters remain the same size and density, and the pits we saw before still exist, apparently unchanged. Since room temperature 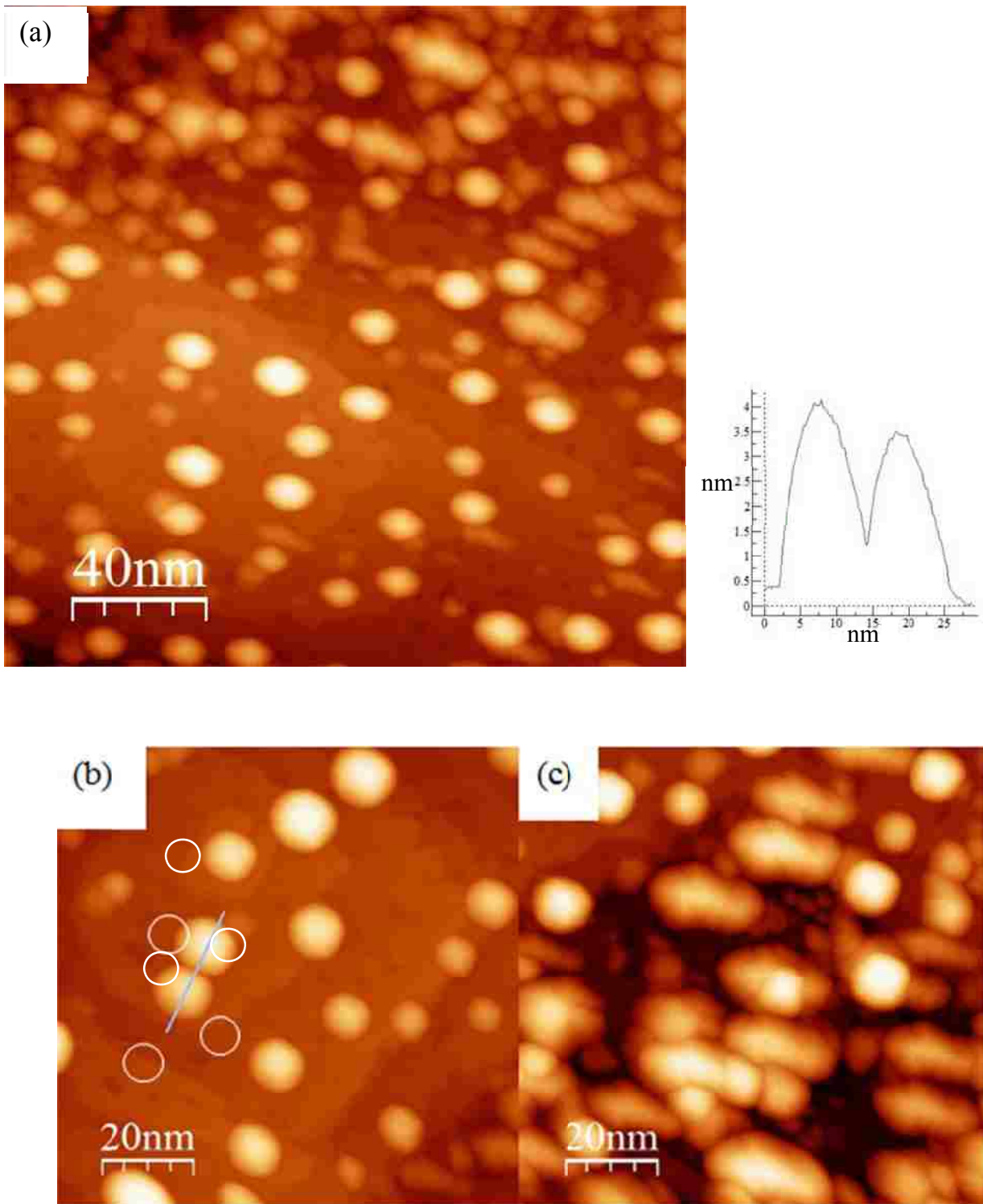O_2 exposure does not produce apparent change to this surface, we annealed the sample to 400°C in 2×10^{-7} Torr O_2 for 20min, which we think will lead to further oxidation of Cu clusters. The STM images obtained after this treatment are shown in Fig. 5.6. As shown in Fig. 5.6, annealing in O_2 did produce substantial changes in the morphology of the surface. Cu clusters on higher terraces seem unchanged in Fig. 5.6(b). A line profile shows that the larger clusters are ~ 4nm in height, which is a little bit bigger than that before O_2 annealing, suggesting some degree of oxidation. The black pits we saw before still exist and the depth is ~ 3.5Å, which is the same as before. Annealing in O_2 cannot apparently heal the missing Zn-O dimers. When we look at the Cu clusters on the shallow rougher area in Fig. 5.6(c), things become a little complicated. The surface looks very rough and some unknown irregular structures are seen in between elongated clusters. We currently do not have a model for how these areas became so rough after being annealed in O_2 nor do we know the precise nature of the elongated clusters.

The oxidation process above was performed on pre-annealed 2ML Cu/ZnO($10\bar{1}0$) surface, on which ripened/oxidized Cu clusters were already formed through partial oxidation from lattice oxygen. In this case, we did not expect complete oxidation of Cu clusters, because only the outmost shell of the Cu cluster was expected to react with O_2 at elevated temperature. To achieve higher degree oxidation of Cu clusters, we performed a layer by layer growth of Cu oxide clusters on ZnO($10\bar{1}0$) surface. We deposited 0.4ML Cu on the surface, and annealed it at 400°C in 2×10^{-7} Torr O_2 for 5min. By repeating this process for 5 times, we obtained a 2ML Cu_xO/ZnO($10\bar{1}0$) sample. Here we do not know the oxidation states of Cu yet, so Cu_xO is used to represent the oxidation state in general. We tried to

image the 2ML $Cu_xO/ZnO(10\bar{1}0)$ surface with STM, however we had tip approach problems with this surface. To make the tip approach successful, we deposited another 2ML Cu on this surface at room temperature, in an attempt to increase the conductivity of the sample. The as prepared surface is shown in Fig. 5.7. In Fig. 5.7, some large clusters are seen with numerous smaller clusters in between. According to the preparation procedure, we ascribe the large clusters to the 2ML Cu_xO obtained using the layer by layer growth, and the smaller clusters are the 2ML Cu deposited in the last step. The line profile shows that the size of smaller clusters is ~ 5nm in diameter and ~ 1nm in height, which is the same as that of the Cu clusters grown at room temperature without annealing.
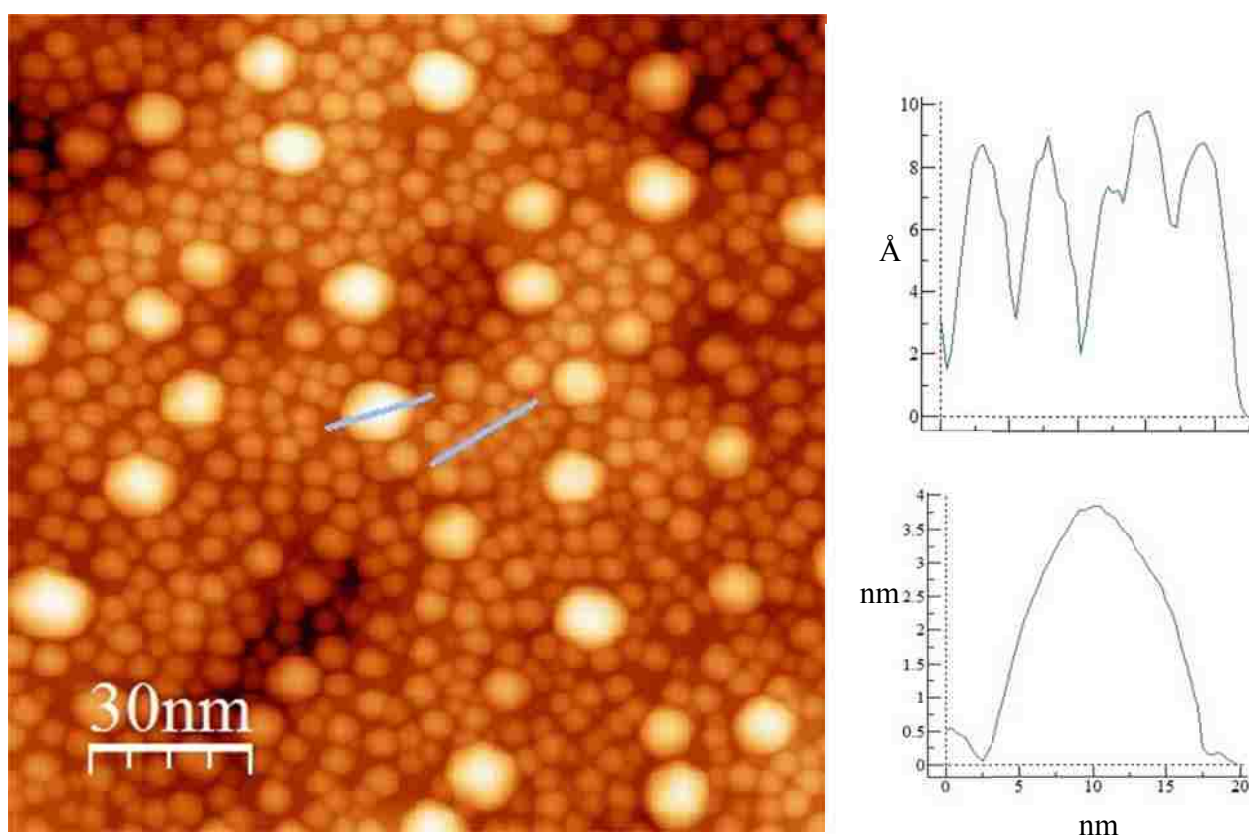

Fig. 5.7 STM image of (2ML Cu + 2ML Cu_xO) on $ZnO(10\bar{1}0)$ surface at RT, small clusters are Cu, while big clusters are Cu_xO

This confirms that they are Cu clusters as seen previously. The larger Cu_xO clusters have a size of ~ 15nm in diameter and ~ 4nm in height.

In Table 5.1, we show a comparison of the size for all clusters prepared in each step. It is clear that the Cu clusters grown at room temperature are smaller than the oxidized clusters. Cu clusters grow much larger upon vacuum annealing, and Cu_xO clusters are probably formed (step 3). Additional annealing in O_2 makes the pre-annealed Cu_xO clusters (step 3) grow a little bit bigger, but not significantly. Cu_xO clusters grown using layer by layer method (step 5) have about the same size as the Cu_xO obtained in step 4. It seems that the ripening/oxidation is essentially complete after vacuum annealing in step 3, and additional annealing in O_2 does not significantly increase cluster size. The layer by layer growth did not create larger Cu_xO clusters either.

Table 5.1. Typical size of the clusters prepared in each step

	Step 1	Step 2	Step 3	Step 4	Step 5
	0.2ML Cu at RT	2ML Cu at RT	2ML Cu annealed in vacuum	2ML Cu annealed in O_2	0.4 ML Cu annealed in O_2 (5 cycles)
Diameter (nm)	5	8	12-15	12-15	12-15
Height (nm)	1-1.2	1-1.2	3-3.5	3.5-4	3.5-4

The series of STM experiments provide us a complete scenario of Cu and Cu_xO clusters growth on ZnO($10\bar{1}0$) surface. At room temperature, Cu grows small 3D clusters at very low coverage, and no 2D thin film growth is observed. As coverage increases, the concentration of Cu clusters increases rapid, while cluster size does not substantially increase until the Cu clusters cover the whole surface.

Annealing the Cu/ZnO(10$\bar{1}$0) surface in vacuum causes the small Cu clusters to agglomerate, forming much larger clusters. The oxidation of Cu probably happens during the annealing procedure, even without the presence of additional O_2. Additional annealing in O_2 does not induce much further oxidation of the Cu clusters.

5.3.2 Photoemission and EELS Studies

In the STM studies above, we proposed that vacuum annealing leads to the oxidation of Cu clusters on ZnO(10$\bar{1}$0) surface. Both Cu_2O (Cu(I)) and CuO (Cu(II)) are stable oxides, and we have direct evidences for the oxidation states of Cu_xO we obtained. The photoemission and EELS experiments will help us know more about the Cu and Cu_xO clusters.

Photoemission spectra were taken with 25eV incident photon energy. Fig. 5.8 shows the spectra of the following samples: clean ZnO(10$\bar{1}$0) (red), 2ML Cu/ZnO(10$\bar{1}$0) (green), 2ML Cu/ZnO(10$\bar{1}$0) annealed in vacuum (brown), and 2ML Cu/ZnO(10$\bar{1}$0) annealed in O_2 (blue). In the clean ZnO spectrum, Zn 3d peak at 10eV BE and O 2p peak between 3eV and 6eV BE are the main features that we observed. When 2ML Cu was deposited on the surface, the Zn 3d and O 2p peaks were significantly suppressed, and a new sharp Cu 3d feature peaking at 3.5eV emerged. The 2ML Cu/ZnO surface was annealed at 400°C in vacuum for 15min, resulting in an increase in the Zn 3d peak intensity, indicating that larger Cu clusters were formed and more ZnO substrate was seen by the photon beam. We tried to identify the oxidation states of the Cu. The Cu(I) and Cu(II) states have been previously reported to produce features at 2.5eV and 1.5eV BE, respectively [137]. The Cu(I) feature overlaps the Cu 3d band, so it is difficult to preciously separate the two. We can still clearly see the change due to the increase in intensity of the Cu(II) state, which is shown in Fig. 5.8(b). After vacuum annealing, this state provides an increase in intensity between 1eV and 2eV BE. This tells us that
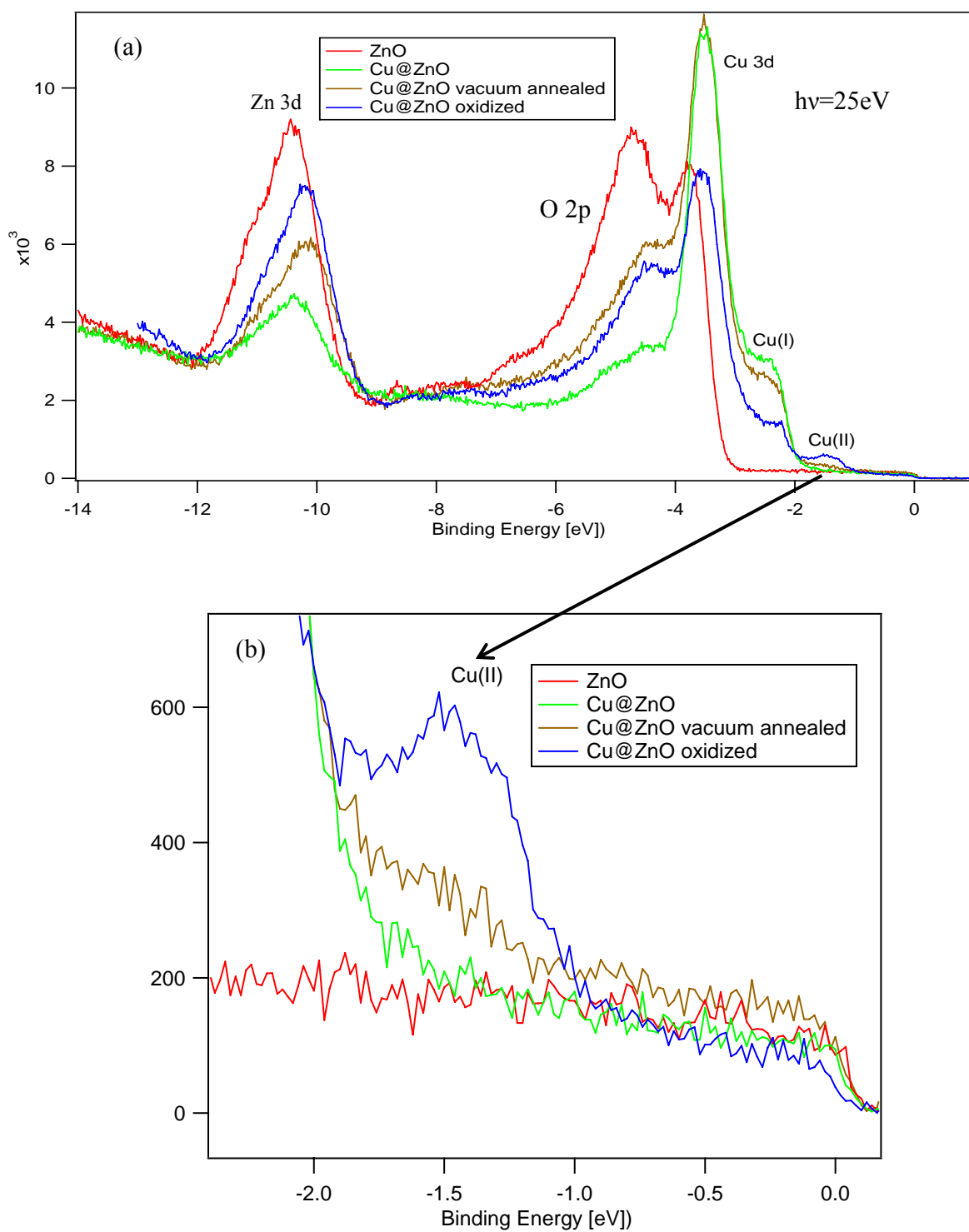
Fig. 5.8 (a) Photoemission spectra of Cu and Cu_xO on $ZnO(10\bar{1}0)$ surface (b) Enlarged Cu(II) feature (Thank Ziyu Zhang for taking the photoemission data)

vacuum annealing leads to partial oxidation of Cu clusters on the ZnO surface, and it is consistent with our STM observations above. Furthermore the Zn 3d peak increases in intensity suggesting a ripening of the cluster size, exposing additional substrate area.

We subsequently annealed the 2ML Cu/ZnO surface at 400°C in 2×10^{-7} Torr O_2 for 20min, as shown in the blue curve. Compared to the 2ML Cu/ZnO annealed in vacuum, the Zn 3d intensity is even higher, implying the ripening/oxidation of Cu clusters is more complete. The intensity ratio of O 2p over Cu 3d is much higher, which is resulted from the additional exposure to O_2 during annealing. Fig. 5.8(b) shows a much stronger Cu(II) peak when Cu/ZnO was annealed in O_2, plotted in blue. In the STM studies, Cu/ZnO sample annealed in O_2 and in vacuum shows a very similar cluster size, but we know from the photoemission spectra that Cu clusters contain more Cu^{2+} species when oxidized in O_2.

We successfully prepared Cu_xO clusters on $ZnO(10\bar{1}0)$ surface, by annealing the $Cu/ZnO(10\bar{1}0)$ sample either in vacuum or in O_2. In photoemission, we clearly saw the Cu(II) state (from CuO), but whether Cu(I) (from Cu_2O) exists in the system is unknown. CuO and Cu_2O have different bandgap [137], so we measured bandgap excitations in EELS, trying to identify the oxidation state of Cu_xO. EELS spectra of $Cu/ZnO(10\bar{1}0)$ sample annealed in vacuum (green) and in O_2 (red) are shown in Fig. 5.9, in which we see different bandgap energies for these two samples. Cu/ZnO annealed in vacuum shows a bandgap of ~ 1.4eV, while the value for sample annealed in O_2 is ~ 2.4eV. The 1.4eV and 2.4eV interband excitation energies correspond to the bandgap of CuO and Cu_2O [137]. This suggests that CuO will form when Cu/ZnO is annealed in vacuum, while Cu_2O is the primary product when Cu/ZnO is annealed in O_2.

5.4 Cu on TiO$_2$(110)

Both Cu/ZnO and Cu/TiO$_2$ are popular catalysts for CO$_2$ reduction, but the mechanisms, reaction pathways, and final products are not the same. We believe that the interaction between the supported metals and oxide substrates plays an important role in the catalytic reaction. The STM experiments of Cu on TiO$_2$(110) surface were performed as a comparison with the Cu on ZnO(10$\bar{1}$0) surface. We examined a series of Cu coverages on TiO$_2$(110), and annealing effects in both vacuum and O$_2$ were also studied.
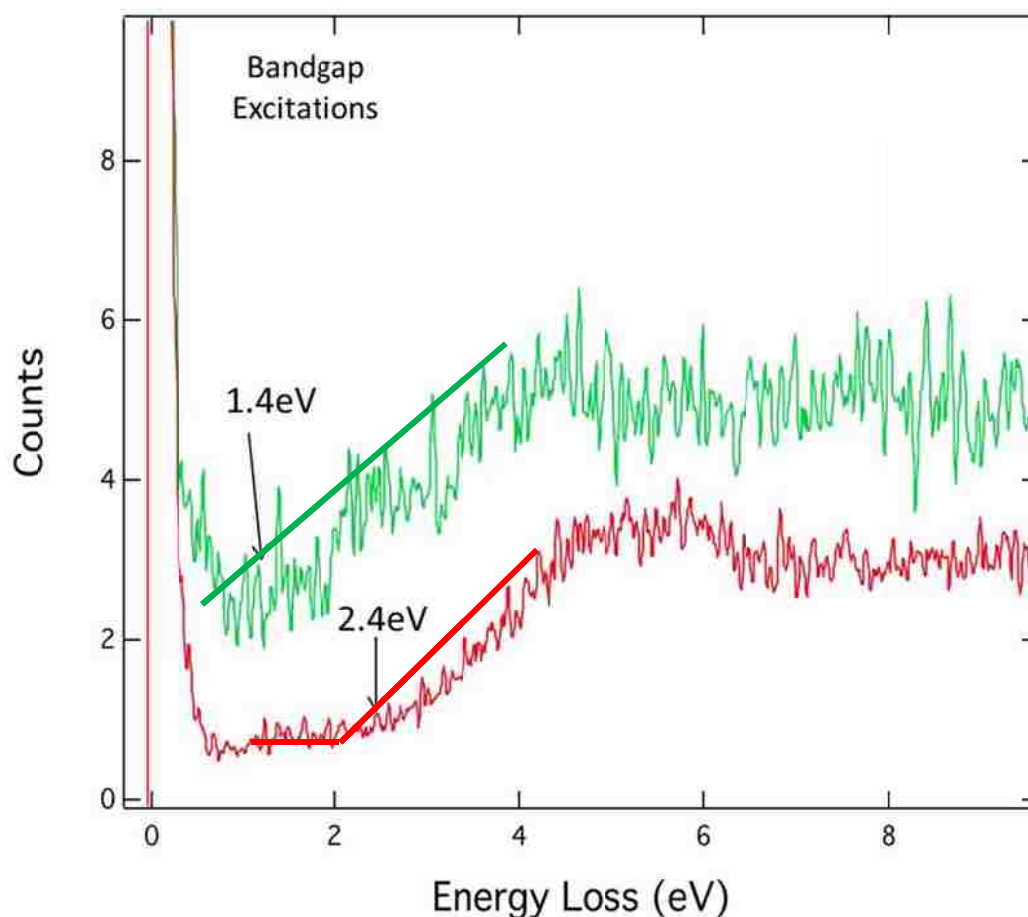

Fig. 5.9 EELS spectra of Cu/ZnO(10$\bar{1}$0) annealed in vacuum (green) and in O$_2$ (red) (Thank Ziyu Zhang for taking the EELS data)

Cu growth on TiO$_2$(110) has been studied with STM by other groups [138, 139]. 3D clusters growth was observed, however, the nucleation sites vary depending on the condition of the surface. Fig. 5.10(a) shows STM images obtained 0.1ML Cu on TiO$_2$(110) surface dosed at room temperature. There are a few interesting observations in this image. At this coverage, Cu mainly forms 3D clusters with preferential nucleation sites at step edges with certain orientations. No 2D thin layer formation has been seen for Cu on TiO$_2$(110) surface at even lower coverage [139]. On the step edges parallel to the [001] direction, few Cu clusters can be seen, and step edges cutting across the [001] directions are fully decorated with Cu clusters. When we look at the ball and stick model of TiO$_2$(110) surface (Fig. 5.11), we know that the [001] is the direction of Ti and O rows. Cu atoms diffuse along the Ti or O rows when they are deposited on the surface, and stop when they meet the steps, forming nucleation sites. At the coverage of 0.1ML, there are some Cu clusters forming on the terraces, while the step edges along [001] direction are still largely without clusters. This tells us the preference of Cu clusters nucleation. Upon deposition, Cu atoms tend to nucleate at steps cutting across the [001] direction. When these steps are fully covered, Cu clusters start to grow on the terraces. The steps along [001] direction are the last choice for Cu atoms to stay.

At 0.1ML coverage, the typical Cu cluster size is ~5nm in diameter and ~1nm in height, corresponding to three or four layers of Cu atoms. Smaller Cu clusters are also seen on the surface. However, another study [138] showed well dispersed 0.1ML Cu clusters on TiO$_2$(110) at room temperature, which is drastically different from our study here. This is probably due to the preparation of TiO$_2$(110) surface. As we know, TiO$_2$(110) surface can be reduced by sputtering and vacuum annealing, and there are various kinds of surface defects. In that paper [138], the DFT calculations indicate a very high bonding energy between Cu atoms and bridging O atoms, while the bonding

between Cu atoms and surface defects is much weaker. On a stoichiometric TiO$_2$(110) surface, because of the strong bonding between Cu atoms and bridging O atoms, the Cu atoms may not be able to overcome the diffusion barrier, thus cannot diffuse to the step edges. If this is the case, well dispersed Cu clusters on the terraces instead of step edges may be observed. Our TiO$_2$(110) sample has a high level of defects at the surface, so the bonding between Cu atoms and the defect rich surface is relatively weak, and diffusion of Cu atoms on the surface becomes more energetically favorable.

We increased the Cu coverage to 0.5ML, and the STM image obtained from the surface is shown in Fig. 5.10(b). From 0.1ML to 0.5ML coverage, there is no obvious increase of cluster density, and the distribution of Cu clusters is very similar to that of 0.1ML coverage. A few small Cu clusters are seen on the steps that are parallel to the [001] direction, but these steps are still not the main nucleation sites for Cu at 0.5ML coverage. A line scan shows a typical cluster size of ~7nm in diameter and ~2-2.5nm in height, which is much larger than that of clusters at 0.1ML coverage.

STM images of 1ML and 3ML Cu on TiO$_2$(110) surface are shown in Fig. 5.10(c) and (d). Form 0.5ML to1ML coverage, we do not observe an increase in the size of the Cu clusters, but there are more clusters growing on the terraces across the surface. For coverage beyond 1ML, the density of Cu clusters almost saturates, and the clusters grow bigger as the coverage increases. At a coverage of 3ML Cu, the typical cluster size is ~ 8-10nm in diameter and ~ 4-4.5nm in height. The height of Cu clusters grows much faster than the diameter. Cu growth on TiO$_2$(110) at room temperature has been investigated with STM. As we saw above, Cu shows distinct growth behavior at different coverage ranges. For very low coverage, Cu adopts 3D cluster growth mode with preferential nucleation at steps cutting across the [001] direction with few clusters seen on the terraces. The surface energy of Cu (~ 2J·m^{-2}) was calculated to be much larger than that of TiO$_2$ (~ 0.7J·m^{-2}) [140, 141]. When Cu atoms are
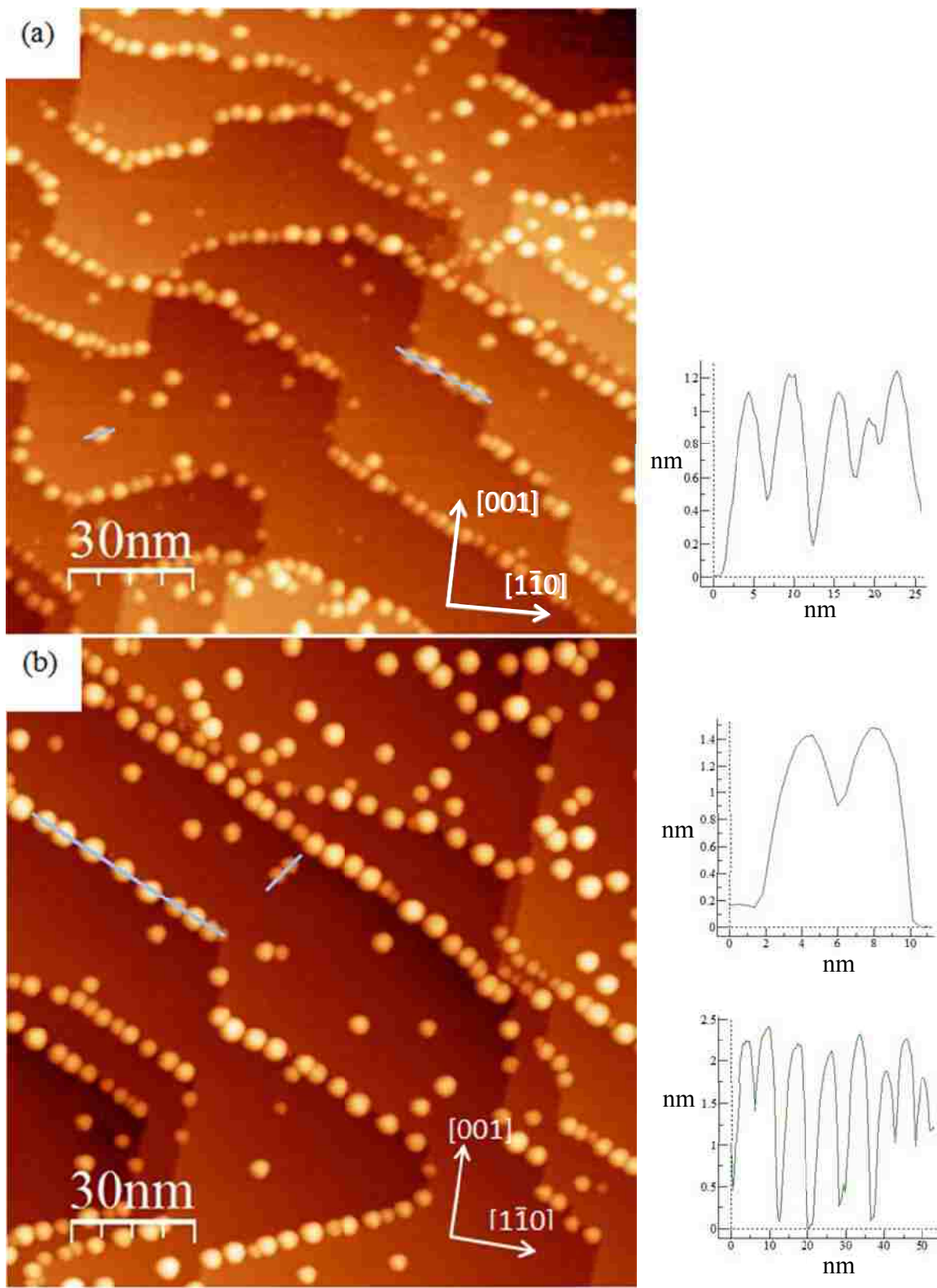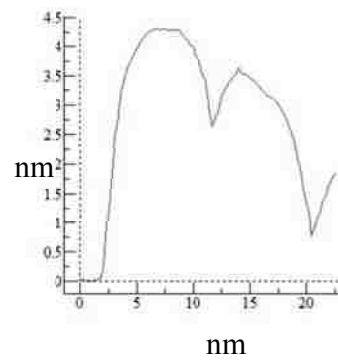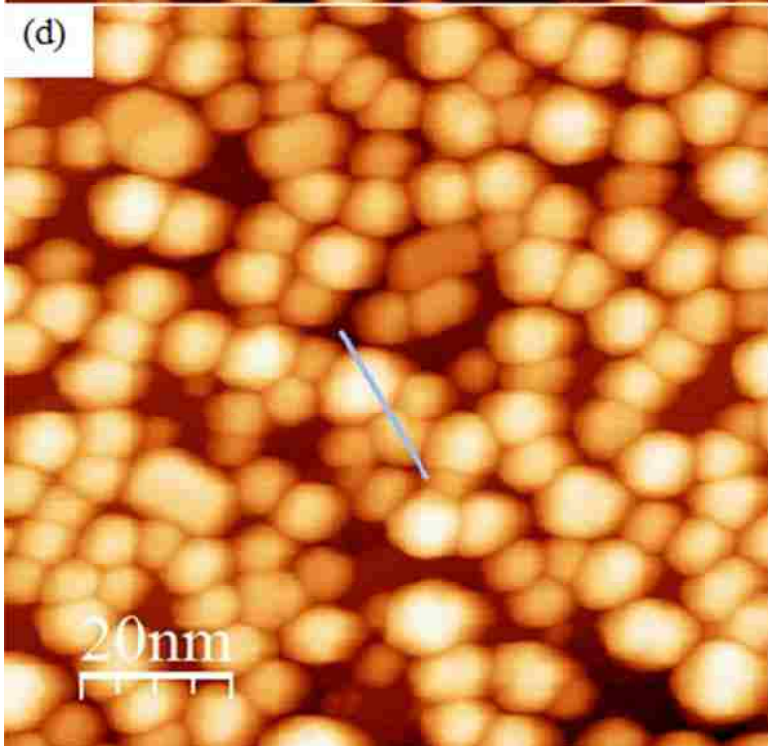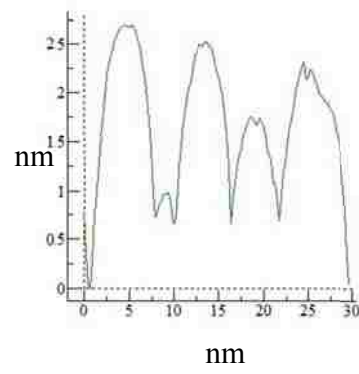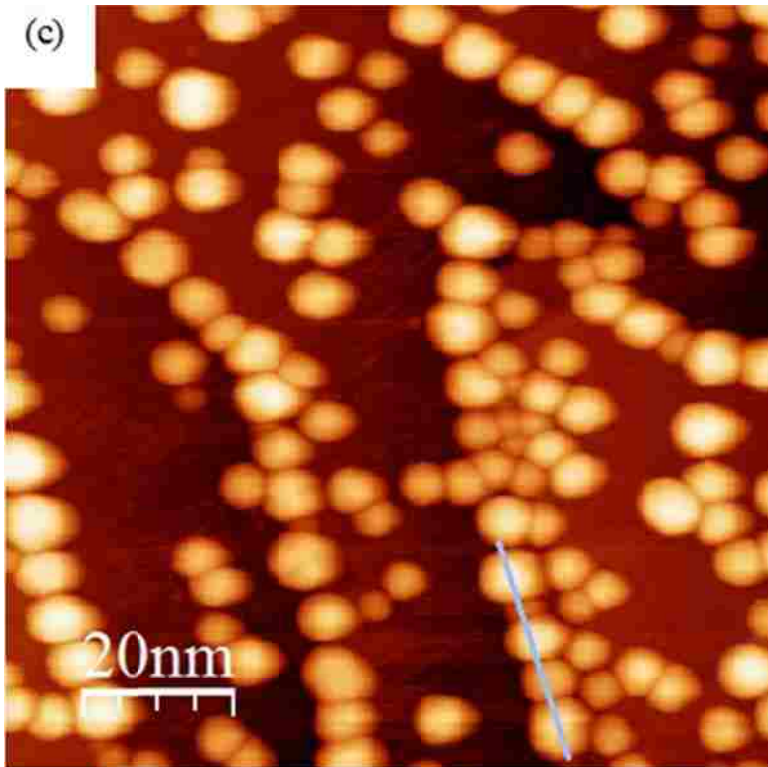
Fig. 5.10 STM images of (a) 0.1ML (b) 0.5ML (c) 1ML and (d) 3ML Cu growth on TiO$_2$(110) surface at room temperature
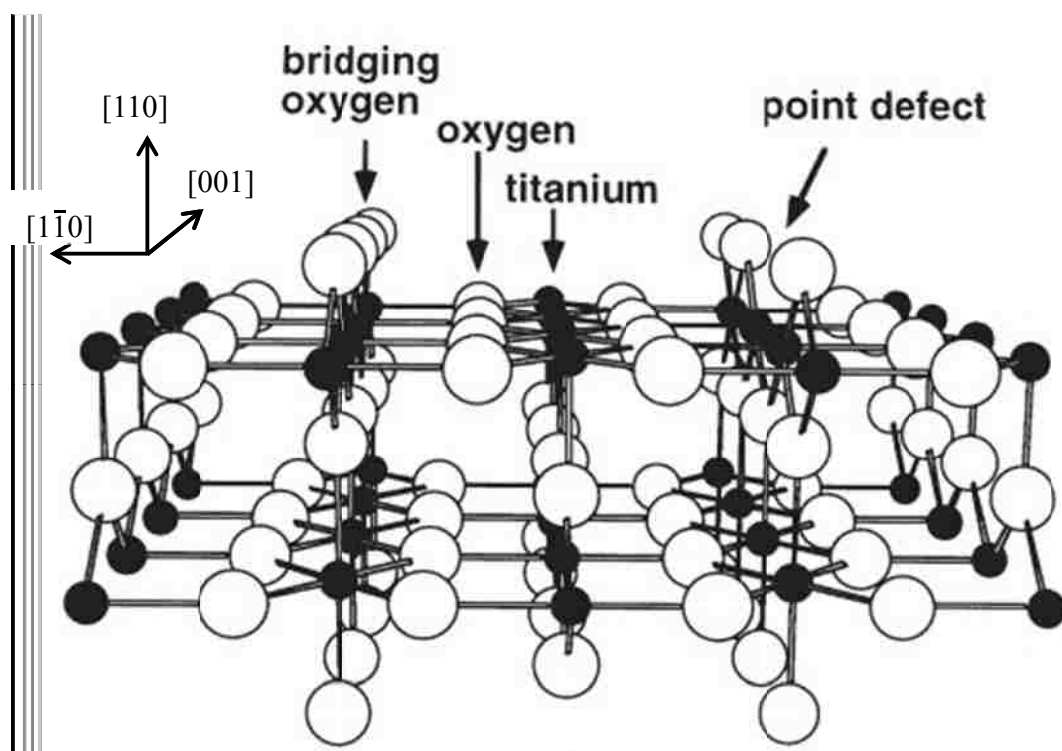
(Fig. 5.10 continued)

Fig. 5.11 Ball and stick model of TiO$_2$(110) surface [142]

deposited on the surface, they tend to form clusters in order to obtain minimal surface area, thus lowering the surface free energy of the system. The 3D growth also indicates high mobility of Cu atoms on defective TiO$_2$(110), and a weak interaction between Cu atoms and the surface. At 0.1ML coverage, Cu clusters almost cover all the step edges, and the cluster size is relatively small. Beyond this coverage, the density of Cu clusters does not change much, but the clusters grow much bigger as we increase the coverage to a certain amount (0.5ML). When the cluster size increases to ~ 7nm in diameter and ~ 2.5nm in height (a little less than 0.5ML coverage), the deposition of additional Cu atoms will not result in additional Cu bonding to the clusters on step edges. Instead, they start to grow on the terraces at new nucleation sites. At 0.5ML Cu coverage, the cluster density at the step edges saturates, and we see additional clusters on the terraces. Further deposition of Cu leads to an increase of cluster density on the terraces, while cluster size remains the same. As we see in Fig. 5.10(c), at

1ML coverage, Cu clusters are well dispersed on the terraces, but the cluster density is not yet saturated. For coverage above 1ML, Cu continues to grow clusters on terraces until the surface is almost fully covered. After that, the clusters will grow bigger, and the cluster size is dependent on the amount of Cu deposited. As shown In Fig. 5.10(d), the typical size of Cu clusters is ~ 8-10nm in diameter and ~ 4-4.5nm in height when the coverage is increased to 3ML. For this high coverage, Cu atoms evaporated to the surface will simply stick on top of the clusters.

High temperature vacuum annealing of the deposited Cu clusters has been studied. Samples of 0.5ML and 3ML Cu on $TiO_2(110)$ surface were annealed at 400˚C in UHV for 20min. The 0.5ML and 3ML coverages were chosen because they are critical coverages for changes in Cu growth modes on $TiO_2(110)$ as discussed above. The STM images of annealed surface are shown in Fig. 5.12(a) and (b). When comparing them with the STM images obtained before annealing (Fig. 5.10(b) and (d)), we do not see any significant changes in the clusters for both Cu coverages. The distribution of Cu clusters remains the same, and line profile does not show a cluster size change either. The 0.5ML coverage TiO_2 terraces do show an apparent increase in defects, however.

In contrast with this data for $Cu/TiO_2(110)$, for Cu on $ZnO(10\bar{1}0)$, we observed an obvious ripening of small Cu clusters when the sample was annealed to 400˚C. It implies that Cu atoms have much higher mobility at elevated temperature than at room temperature, so we would expect the same ripening of Cu clusters upon annealing but this is not the case for Cu on $TiO_2(110)$. This suggests that Cu atoms bond much stronger on $TiO_2(110)$ than to $ZnO(10\bar{1}0)$, and 400˚C is not high enough for Cu atoms to move and grow bigger clusters on TiO_2. However, ripening of Cu clusters on $TiO_2(110)$ was observed previously at higher annealing temperatures [139]. In that study, they annealed the Cu clusters to 700K and 925K. At 700K, there was a slight ripening that occurred, but cluster size did not
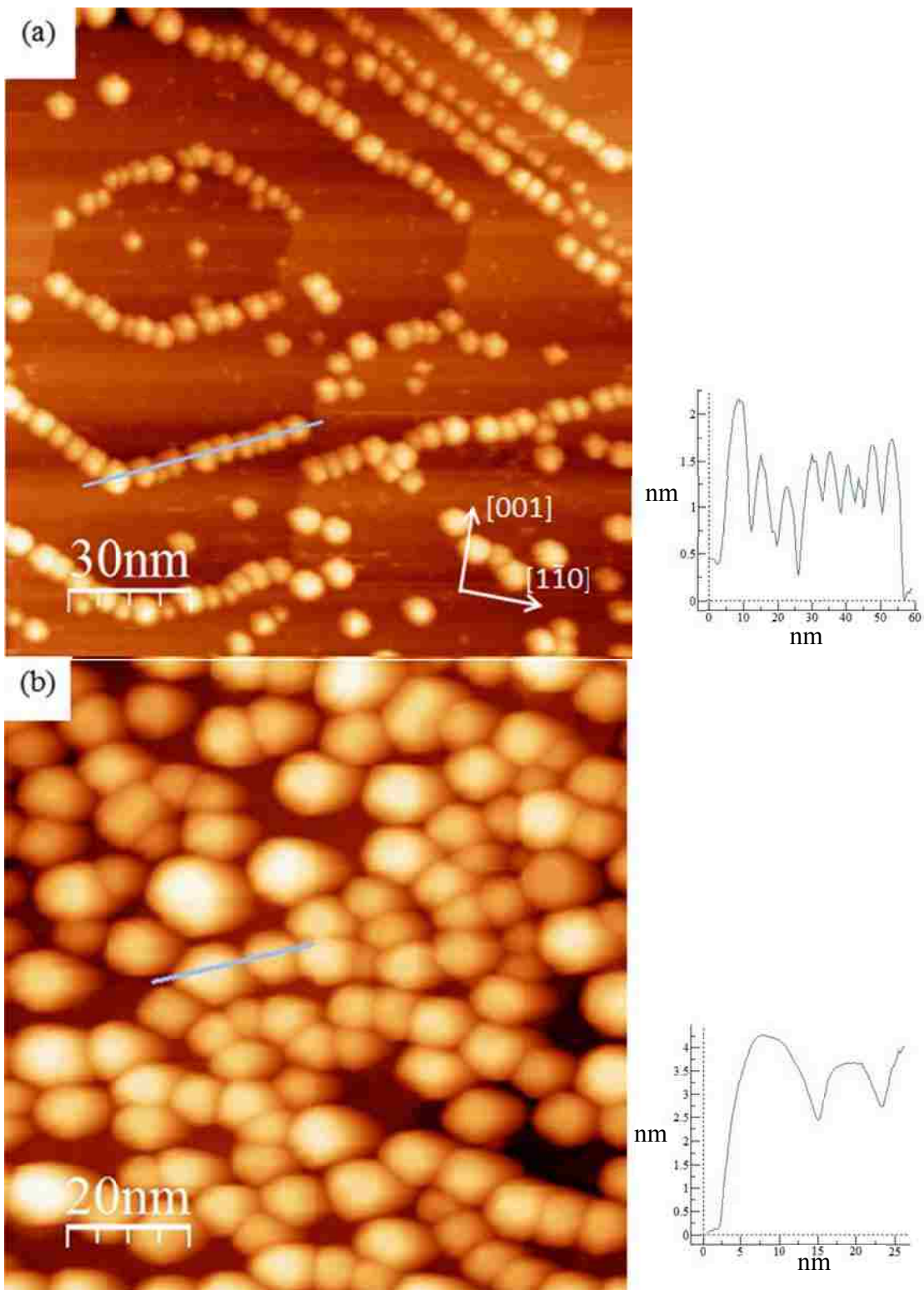
Fig. 5.12 STM images of (a) 0.5ML and (b) 3ML Cu on $TiO_2(110)$ after annealed at 400°C in vacuum for 20min
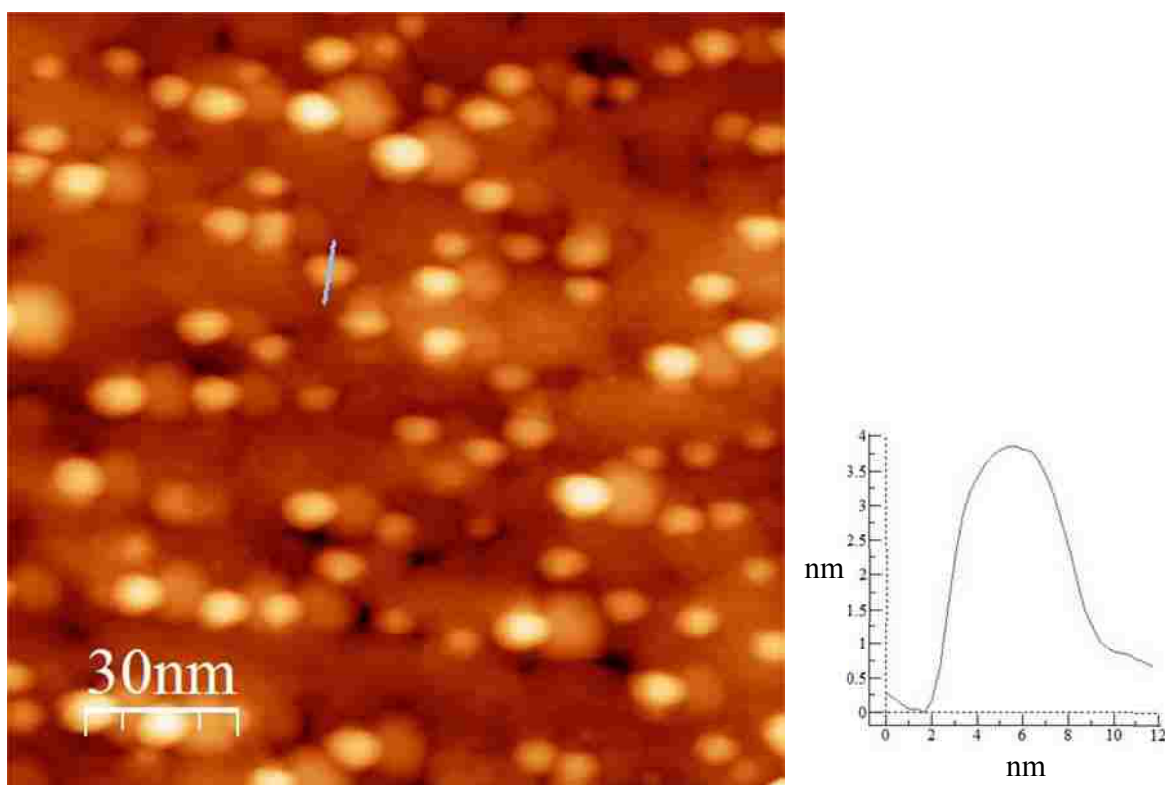
Fig. 5.13 STM image of 0.5ML Cu/TiO$_2$(110) after annealed at 400˚C in 2×10^{-7} Torr O$_2$ for 20min

increase substantially. At 925K, there was a huge increase of cluster size. They found that the Cu cluster size depends only on the annealing temperature, and is independent of the initial Cu coverage [139].

In addition to vacuum annealing, we also annealed the Cu clusters in O$_2$, as we did for Cu on ZnO(10$\bar{1}$0). The 0.5ML Cu on TiO$_2$(110) sample was annealed to 400˚C in 1×10^{-7} Torr O$_2$ for 20min, in order to establish the role that additional O$_2$ plays in the resulting morphology. The STM image of this annealed surface is shown in Fig. 5.13. As we see, there is a significant change in the overall surface morphology compared with the 0.5ML Cu on TiO$_2$(110) at room temperature. According to the discussion above, we found that vacuum annealing to 400˚C did not substantially change the surface of the clusters, so the change we see here must be due to the interactions between Cu clusters and O$_2$. The

clusters in Fig. 5.13 have an average size of ~ 8nm in diameter and ~ 4nm in height, and are much taller than the clusters at room temperature for the same coverage. We have not taken the photoemission measurements of this surface, but from the drastic increase of cluster size, we deduce that the clusters are more fully oxidized during this annealing procedure. The TiO_2 substrate underneath the Cu clusters becomes rough, and we cannot resolve flat terraces and step edges. This oxidation process drastically changed the Cu clusters, as well as the underlying TiO_2 substrate.

5.5 Au on ZnO(10$\bar{1}$0)

Like Cu, Au deposited on certain metal oxides was found to be active for hydrogenation of CO and CO_2 [132]. For methanol synthesis from CO and CO_2, Au/ZnO showed very similar catalytic activity as Cu/ZnO catalysts [132, 143, 144]. The catalytic performance of the Au catalyst depends largely on the particle size, as well as the interaction between Au and substrate [144-146]. We carried out the STM experiments of Au growth on ZnO(10$\bar{1}$0) as a comparison with Cu growth on ZnO(10$\bar{1}$0). Fig. 5.14(a) shows an STM image of 0.05ML Au grown on ZnO(10$\bar{1}$0) at room temperature. It is clearly seen that many small Au islands are well dispersed randomly over the surface.

Unlike low coverages of Cu on ZnO(10$\bar{1}$0), we do not observe preferential nucleation sites for Au, and almost no islands are found at step sites. The small Au islands have an average size of ~ 3nm across and ~ 0.3nm high. We inspected the islands sizes at most places on the surface, and found all the clusters have about the same height. This 0.3nm height represents just one layer of Au, which means an islanding 2D growth mode is adopted for Au on ZnO(10$\bar{1}$0) at initial coverages. Au on TiO_2(110) surfaces have been extensively studied because of its unique catalytic activity for CO oxidation [6, 147]. On TiO_2(110), at a coverage of 0.1ML, Au mainly grows 3D clusters of about 1nm to 1.5nm high, and they preferentially nucleate at step edges. Some quasi 2D small clusters of about

105

0.3nm to 0.6nm high are well dispersed on the surface [72, 148, 149]. For 0.05ML Au on ZnO(10$\bar{1}$0), the clusters are truly 2D flat islands, which are only 0.3nm high. This observation implies that the bonding between Au atoms and ZnO(10$\bar{1}$0) surface is somewhat stronger, and the mobility of Au atoms on this surface is reduced.

STM images of 0.4ML and 3ML Au on ZnO(10$\bar{1}$0) surface are shown in Fig. 5.14(b) and (c). At 0.4ML coverage, there is an obvious increase of island density on the surface, and step sites are still not preferred for island growth. We found the height of islands ranges from 0.3nm to 0.9nm, and most of them are less than 0.7nm high. The existed thin Au islands already present from the prior 0.05ML Au deposition do not act as nucleation sites for the new Au atoms arriving on the surface.
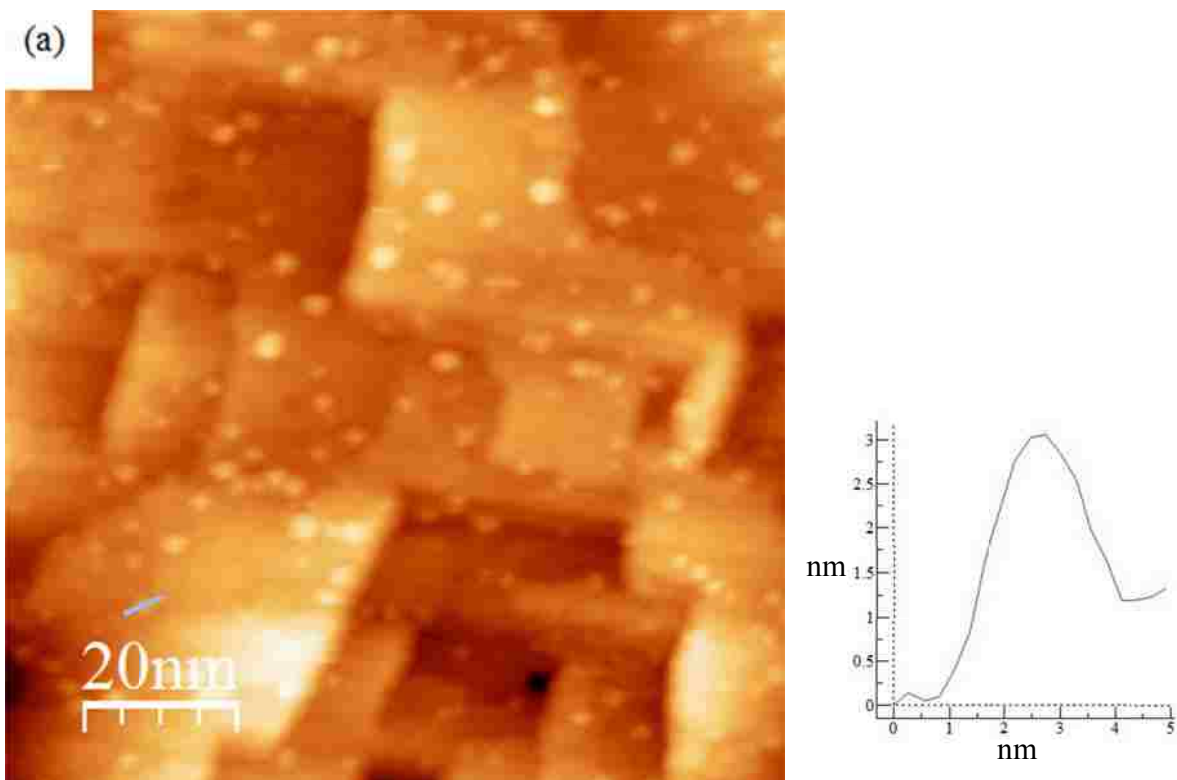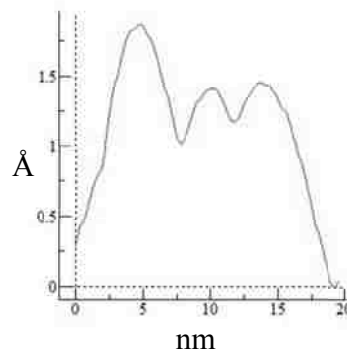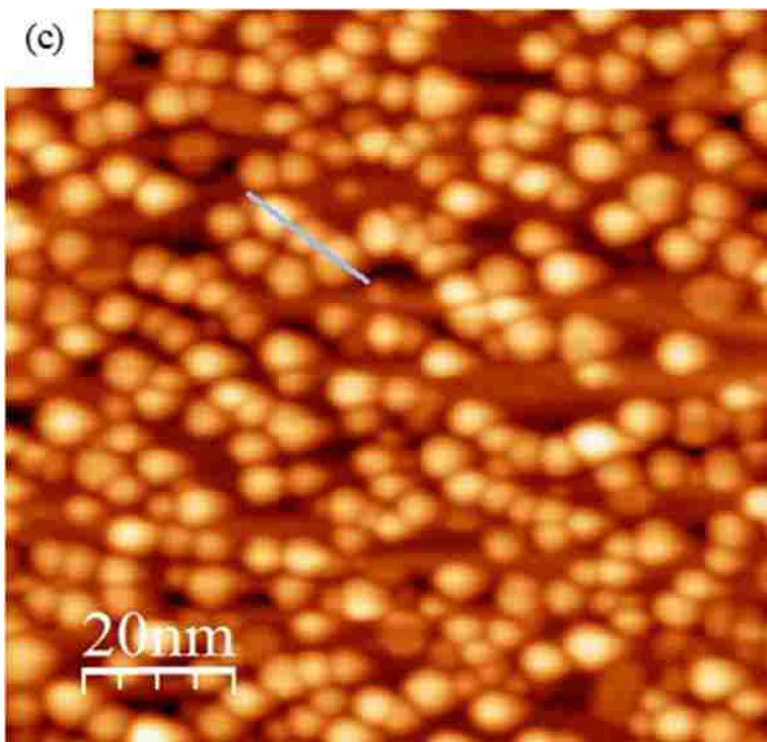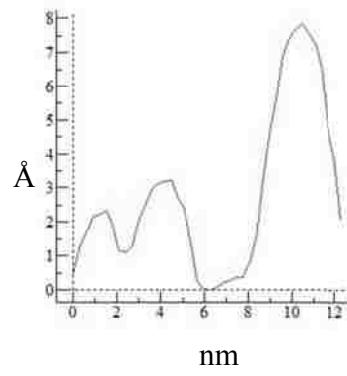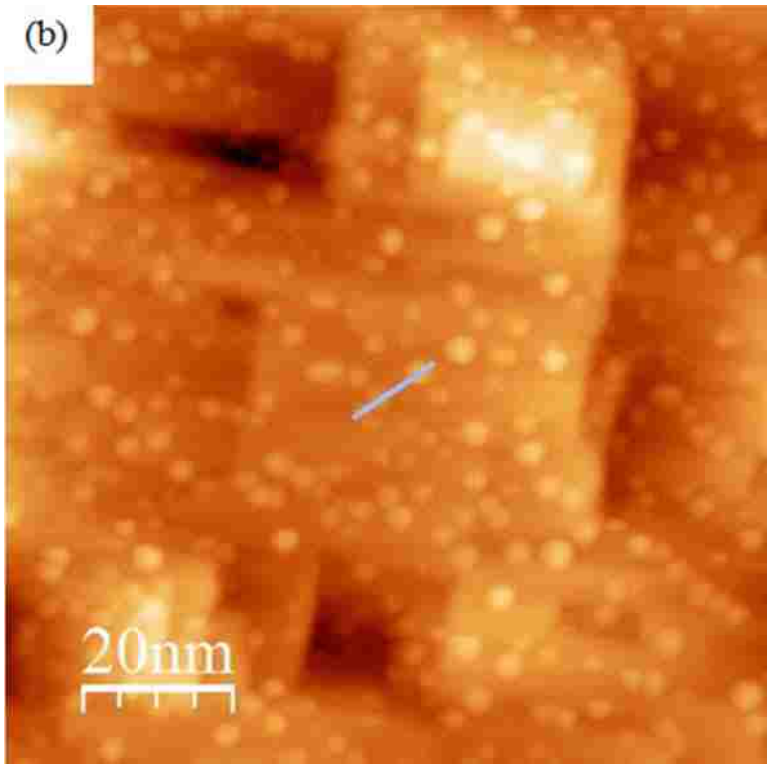

Fig. 5.14 STM image of (a) 0.05ML (b) 0.4ML and (c) 3ML Au growth on ZnO(10$\bar{1}$0) surface

(Fig. 5.14 continued)

With the deposition of more Au, the old Au islands do not grow in size, and remain one or two atomic layers in height. The new Au atoms tend to find unoccupied sites as new nucleation sites. After the island grows to a critical size of 3-4nm across by 0.7nm high, more Au atoms will not stick to the island, instead new islands will be formed. At the critical size, the Au-Au bonding strength probably becomes smaller than the Au-substrate bonding, and a self-limiting growth of Au islands can be observed. After the small Au islands cover a large portion of the surface, no new nucleation sites will be created, and Au islands start to grow bigger and taller. At a coverage of 2ML, 3D Au clusters of ~7nm across and ~1.5nm high are well distributed all over the surface. The diameter is much bigger than height at this size, meaning the clusters are oblate disks and are still not spherical. On $ZnO(10\bar{1}0)$ surface, high coverage of Au exhibits limited 3D cluster growth, but it is not prominent. The islands remain thin, and have a tendency to wet the surface.

The 0.4ML and 3ML Au on $ZnO(10\bar{1}0)$ samples have been annealed to 400˚C for 20min, and the STM images of the annealed surfaces are shown in Fig. 5.15. Comparing to the 0.4ML and 3ML Au coverages before annealing, there seem no significant changes in island size and distribution, but some difference can still be seen. For 0.4ML coverage, before annealing, most of the surface is covered with many Au islands that are limited to one or two layers in height, randomly distributed on the surface. After annealing, we believe there is a slight ripening of Au islands. The size of the islands becomes more uniform, with most of them two atomic layers high. Besides the size change, we also observe a tendency of islands to diffuse to the step edges. Many of the islands are well aligned along the step edges, and the number density of islands on terraces decreases. For 3ML coverage, the Au islands become a little bigger in diameter after annealing, but the height is about the same. Some smaller islands can be seen around the big islands, which are possibly due to the incomplete ripening
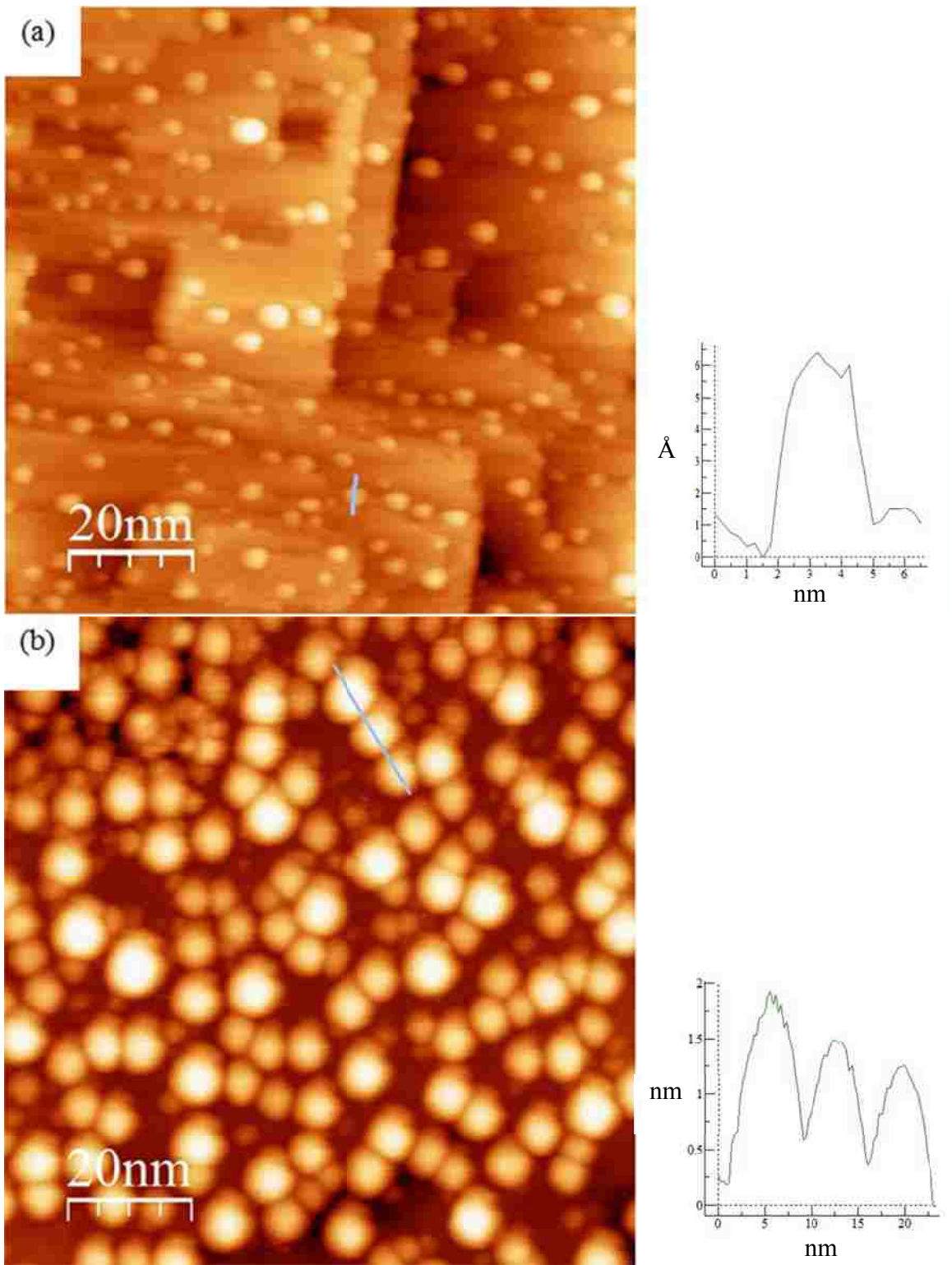
Fig. 5.15 STM image of (a) 0.4ML and (b) 3ML Au on ZnO(10$\bar{1}$0) surface after vacuum annealing at 400˚C for 20min

of the Au islands. We did not perform the photoemission experiments of the Au on ZnO(10$\bar{1}$0) system, so we do not have an independent measure of whether there are additional chemical reactions occurring on the surface upon annealing. Because of the positive heat of formation of gold oxide, we do not anticipate oxidation to occur and only expect that the Au islands ripen.

5.6 Conclusions

In this chapter, we have investigated the surface morphology of noble metals (Cu, Au) supported on ZnO(10$\bar{1}$0) and TiO$_2$(110) surfaces. All three metal and metal oxide combinations show very different growth behavior.

On ZnO(10$\bar{1}$0) surface, 3D cluster growth is observed for very low Cu coverage, and clusters preferentially nucleate on the step edges cutting across the steps aligned along [1$\bar{2}$10] direction. Upon deposition, the diffusion of Cu atoms is constrained along the Zn-O dimer rows. More deposition of Cu will significantly increase the number density of clusters until the whole surface is covered by clusters, at which point the cluster size remains the same. Upon vacuum annealing to 400˚C, the small Cu clusters agglomerate to form much larger clusters, which cover only a fraction of surface area. Photoemission spectra clearly show oxidation state of Cu changes after vacuum annealing, meaning the Cu clusters can react with oxygen atoms on ZnO surface during this procedure. In the meanwhile, many one atomic layer deep pits are found on the surface. This is a strong indication that the ZnO surface is also changed after vacuum annealing. Clearly lattice oxygen atoms are involved in the reaction but the fate of the Zn atoms left on the surface is not well established. Annealing the well dispersed small Cu clusters in oxygen to 400˚C also leads to ripening and oxidation of Cu clusters. EELS measurements show different oxidation states of Cu for clusters annealed in vacuum and in oxygen. After annealing in vacuum, most Cu oxides exist in the Cu(II) state, while Cu(I) state

dominates the Cu oxide obtained by annealing Cu clusters in an oxygen ambient. Electrochemical reactions show that ~3ML Cu oxide clusters in Cu(I) state are most active in CO_2 reduction, giving the largest yield of methanol [30].

On $TiO_2(110)$, similar Cu 3D cluster growth is seen with preferential nucleation on step edges with certain step directions favored at very low coverage. Cu atoms on this surface will diffuse along the Ti or O rows in the [001] direction. After the steps are decorated, more Cu deposition will lead to an increase of the cluster size and not the number density of clusters as we saw for $ZnO(10\bar{1}0)$. Vacuum annealing to 400˚C does not change either the clusters or the TiO_2 substrate. Our study of Au growth on $ZnO(10\bar{1}0)$ conducted because of its similar catalytic activity as Cu/ZnO catalysts provides another useful comparison indicating the role of the substrate in the resulting morphology of oxide supported metal clusters. At coverages below 0.5ML, Au forms quasi-2D islands with one or two atomic layers high and randomly dispersed all over the surface. As we increase the coverage, Au islands grow bigger, but they do not grow much taller, which is significantly different from Cu cluster growth.

Chapter 6: Summary

The work in this dissertation has focused on elucidating and better understanding the structural and electronic properties of catalytic systems that involve noble metals on metal-oxides. In particular, I have studied the morphology of the surfaces produced under well-characterized conditions, trying to understand how and why a noble metal grows in a particular fashion on a metal oxide surface. The questions which have been raised are numerous: What is the growth mode? Does the metal wet the surface or nucleate as clusters? What are the kinetics and thermodynamics that govern the growth of the metal? In addition to the surface morphology, electronic and optical properties of the supported noble metals have also been investigated.

To summarize the work, I would like to address the most important and interesting findings here. In the introduction chapter, I mentioned the catalysis of Au nanoclusters on $TiO_2(110)$ for CO oxidation at low temperature. The catalytic efficiency is extremely sensitive to the cluster size, with a very narrow size window of 2-3nm for optimal performance. As the size of a material approachs the nanometer size region, it will undergo the transition from bulk material to that approaching a real atomic level, and quantum size effects will drastically change its electronic, optical, and magnetic properties. Differing from the bulk metal, the electron energy levels of the nanoclusters are not continuous. One of the main observations in this work is the evolutions of Ag 4d and 5sp band with the change of Ag coverage. At very low coverage of a fraction of ML, Ag 5sp feature shows a distinct peak below the Fermi level. As we increase the coverage, the Ag 5sp peak continues to broaden and finally evolves a well-defined Fermi edge. This is a direct observation of Ag 5sp band changing from a discrete atomic level to metallic bulk behavior with the increase of cluster size. However, the surface

of the substrate largely determines the cluster growth mode, including the size and density distribution. I did a comparison of Ag growth on r- and o- $TiO_2(110)$ surfaces. On the r-TiO_2 surface, Ag clusters of a few nanometers in dimension mainly grow on the step edges at low coverage, while much smaller Ag clusters will disperse across the terraces of the surface in the presence of oxygen adatoms. These more dispersed nanoclusters provide very large surface area for catalytic activities, demonstrating that one can engineer the nature of clusters in a well-controlled manner for future applications. In addition to determining the morphology of the clusters, the electronic interaction between clusters and substrate is also crucial in catalysis. Prior work suggested that the electron charge will transfer from surface oxygen vacancies on r-TiO_2 surface to Ag nanoclusters, but in contrast, my work indicates a charge transfer in the opposite direction for Ag on o-TiO_2 surface. As we know, the recombination of photo-generated hot electron-hole pairs is a huge obstacle for photocatalysis, and the charge transfer within the interface can become an effective way to separate the electron-hole pairs and decrease the recombination rate. For instance, Ag nanoclusters on r-TiO_2 can act as an electron trap, which may potentially increase the number of hot electrons and holes actively involved in the catalysis process.

I provided the Ag/TiO_2 system as an example to explain why the surface science study of supported noble metals is so important to industrial applications. The unique catalytic behaviors of supported noble metal clusters are largely due to their nanometer size, and our surface morphology studies using STM shows how the metal grows on the substrate. In addition, the substrate is far more than a simple physical support. The interaction between the metal clusters and substrate may change the electronic structures of the interface, thus affect the surface chemistry and catalytic behaviors.

Subsequently, I also investigated the surface morphologies of several other noble metal/oxide systems: Cu/ZnO, Cu/TiO_2 and Au/ZnO. By observing the same metal growth on different substrates,

or different metals on the same substrate, we will be able to obtain more information about the kinetics of the deposition and diffusion of the metals. For $ZnO(10\bar{1}0)$, Cu grows 3D hemispherical nanoclusters with preferred nucleation sites on step edges of certain orientations. Unlike Cu, Au grows quasi 2D disk-like islands well dispersed all over the surface. The surface free energy and bonding between metal and substrate are the determining factors for the metal growth. The thermodynamic stability of the system is also an issue in catalysis. A very interesting result of Cu/ZnO surface is the reaction of Cu clusters with surface oxygen atoms upon vacuum annealing, which is not commonly seen for other metal/oxide interfaces. For most of other systems, metal clusters will ripen to reach equilibrium with some external heat.

An extension research of the Ag/TiO_2 system is an effort to enhance the solar absorption for its photocatalysis efficiency. The strong light absorption of Ag nanoclusters due to their plasmon excitation at 3.8eV is seen in EELS. An additional thin layer of titania coated on Ag nanoclusters is believed to improve the catalytic performance, because it may modify the optical response of Ag clusters and can also act as a protection layer for Ag. After including this titania coating, I observed much strong absorption in the energy range of 0.5-2.5eV, which is a large portion of the solar spectrum. This structure provides a possible solution for improving the performance of Ag/TiO_2 catalyst.

My studies of several noble metals [Ag, Cu, and Au] growth on metal oxide surfaces [TiO_2 and ZnO] revealed distinct growth behaviors and differing electronic structures. The morphologies of the metal/oxide surface, which are governed by the kinetics/thermodynamics, can largely determine the surface chemistry, thus influence its catalytic performance. However, due to the extreme complexity of the metal-oxide interfaces, a complete scenario of the noble metals on metal oxide surfaces cannot be

described without careful and complete investigations using various surface science techniques as well as model calculations.

The STM studies of Cu and Cu oxides on ZnO in this work, although important, provide only the initial stages of understanding of the catalytic synthesis of methanol from CO_2. For a more complete understanding, further studies are warranted. For example, understanding the initial CO_2 adsorption sites on the catalytic surface should is critical, because this becomes the first step in a longer set of intermediates to the final products. Because of this necessity, one further study would be to determine how and where CO_2 molecules are adsorbed. It is quite challenging to use STM to image individual CO_2 molecules because of the relative high corrugation of Cu/Cu oxide nanoclusters on the ZnO. However, PES and EELS could be employed to investigate the adsorption. By extracting the modified electronic structure of CO_2 adsorbed on different substrates, for example, clean ZnO, Cu clusters/ZnO and Cu oxide clusters/ZnO, we may be able to identify the adsorption sites and adsorbed species. The vibrational modes of CO_2 on the substrates could also be probed with EELS. The data along with temperature programmed desorption would allow us for a direct comparison with DFT calculation and hence could yield insight into the initial adsorption behavior. Another interesting study will be the comparisons between Cu/ZnO and Au/ZnO. As mentioned before, these two catalysts show very similar catalytic activities for methanol synthesis, either in product selectivity or the yields, indicating that the similarities they share could be the most critical factors in the catalysis reactions. Surprisingly, I have observed significant differences in the surface morphologies between Cu/ZnO and Au/ZnO, and this implies that factors other than surface morphologies may determine the catalysis process. As a result, it would be very interesting to study the electronic properties as well as the vibrational modes of CO_2 adsorbed on Au/ZnO system. If the results represent something very similar

to that of Cu/ZnO, we could be able to obtain a better underlying understanding of the driving forces in the methanol synthesis process. Finally, all the work mentioned above would be under ideal UHV surface science conditions. If we were able to develop a method to construct similar clusters on the oxide substrates under ambient conditions and correspondingly observe similar catalytic activities for methanol synthesis, it would validate and add credibility to the insight gained in our surface science studies and, in turn, be a huge accomplishment in this project.

References

[1] H.-J. Freund, Surf. Sci., 500 (2002) 271.

[2] C.T. Campbell, Surf. Sci. Rep., 27 (1997) 1.

[3] F. Ernst, Mater. Sci. Eng. R, 14 (1995) 97.

[4] V.E. Henrich, P.A. Cox, The Surface Science of Metal Oxides, (1994).

[5] M. Bäumer, H.-J. Freund, Prog. Surf. Sci. (1999).

[6] M.S. Chen, D.W. Goodman, Science, 306 (2004) 252.

[7] O. Dulub, W. Hebenstreit, U. Diebold, Phys. Rev. Lett., 84 (2000) 3646.

[8] U. Diebold, J.M. Pan, T.E. Madey, Surf. Sci., 331-333 (1995) 845.

[9] C. Noguera, Physics and Chemistry of Oxide Surfaces, (1996).

[10] C.R. Henry, Surf. Sci. Rep., 31 (1998) 231.

[11] A. Fujishima, K. Honda, Nature, 238 (1972) 37.

[12] U. Diebold, Surf. Sci. Rep., 48 (2003) 53.

[13] A. Mills, H.R. Davies, D. Worsley, Chem. Soc. Rev., 22 (1993) 417

[14] Y. Paz, Z. Luo, L. Rabenberg, A. Heller, J. Mater. Res., 10 (1995) 2842.

[15] O. Legrini, E. Oliveros, A.M. Braun, Chem. Rev., 93 (1993) 671.

[16] M. Hoffman, S. Martin, W. Choi, D. Bahnemann, Chem. Rev., 95 (1995) 69.

[17] A.L. Linsebigler, G. Lu, J. J. T. Yates, Chem. Rev., 95 (1995) 735.

[18] B. O'Regan, M. Grätzel, Nature, 353 (1991) 737.

[19] W. Zhu, X. Qiu, V. Iancu, X.Q. Chen, H. Pan, W. Wang, N.M. Dimitrijevic, T. Rajh, H.M.M. III, M.P. Paranthaman, G.M. Stocks, H.H. Weitering, B. Gu, G. Eres, Z. Zhang, Phys. Rev. Lett., 103 (2009) 226401.

[20] R. Asahi, T. Morikawa, T. Ohwaki, K. Aoki, Y. Taga, Science, 293 (2001) 269.

[21] T.L. Thompson, J. J. T. Yates, Chem. Rev., 106 (2006) 4428.

[22] J.Ø. Hansen, E. Lira, P. Galliker, J. Wang, P.T. Sprunger, Z. Li, E. Lægsgaard, S. Wendt, B. Hammer, F. Besenbacher, J. Phys. Chem. C, 114 (2010) 16964.

[23] S. Wendt, P.T. Sprunger, E. Lira, G.K.H. Madsen, Z. Li, J.Ø. Hansen, J. Matthiesen, A.B. Rasmussen, E. Lægsgaard, B. Hammer, F. Besenbacher, Science, 320 (2008) 1755.

[24] C.M. Yim, C.L. Pang, G. Thornton, Phys. Rev. Lett., 104 (2010) 036806.

[25] S. Wendt, R. Bechstein, S. Porsgaard, E. Lira, J.Ø. Hansen, P. Huo, Z. Li, B. Hammer, F. Besenbacher, Phys. Rev. Lett., 104 (2010) 259703.

[26] C.M. Yim, C.L. Pang, G. Thornton, Phys. Rev. Lett., 104 (2010) 259704.

[27] M.S. Spencer, Top. Catal., 8 (1999) 259.

[28] K. Ozawa, Y. Oba, K. Edamoto, Surf. Sci., 601 (2007) 4053.

[29] O. Dulub, L.A. Boatner, U. Diebold, Surf. Sci., 504 (2002) 271.

[30] M. Le, M. Ren, Z. Zhang, P.T. Sprunger, R.L. Kurtz, J.C. Flake, J. Electrochem. Soc., 158(5) (2011) E45.

[31] G. Binnig, H. Rohrer, C. Gerber, E. Weibel, Phys. Rev. Lett., 49 (1981) 57.

[32] G. Binnig, H. Rohrer, IBM Journal of Research and Development, 30 (1986) 4.

[33] G. Binnig, H. Rohrer, Rev. Mod. Phys., 59 (1987) 615.

[34] C. Bai, Scanning Tunneling Microscopy and its Applications, (2000).

[35] D. Bonnell, Scanning Probe Microscopy and Spectroscopy, (2000).

[36] R. Eiesendanger, Scanning Probe Microscopy and Spectroscopy, (1994).

[37] G. Binnig, Atomic Force Microscopy and Method for Imaging Surfaces with Atomic Resolution, US Patent No. 4, 724, 318.

[38] M.P.I.o.M. Physics, http://www.mpi-halle.mpg.de/~theory/pro/t_project_henk/stm.tunnel.htm.

[39] I. Senevirathne, PhD dissertation, Louisiana State University, (2008).

[40] W. Zhao, PhD dissertation, Louisiana State University, (2005).

[41] D. Hite, PhD dissertation, Louisiana State University, (2001).

[42] O. Kizilkaya, PhD dissertation, Louisiana State University, (2003).

[43] M. Schmid, http://www.iap.tuwien.ac.at/www/surface/stm_gallery/stm_schematic, (2005).

[44] Omicron VT-STM manual.

[45] Omicron Variable Temperature UHV SPM manual.

[46] LK 2000 Spectrometer manual.

[47] H. Hertz, Ann. Phys., 17 (1887) 983.

[48] A. Einstein, Ann. Phys., 31 (1905) 132.

[49] S. Hüfner, Photoelectron Spectroscopy, (1995).

[50] G.A. Sawatzky, Nature, 342 (1989) 480.

[51] J.C. Green, Ann. Rev. Phys. Chem., 28 (1977) 161.

[52] E.W. Plummer, W. Eberhardt, Advances in Chemical Physics, 49 (1982) 533.

[53] H. Lüth, Surfaces and Interfaces of Solid Materials, (1995).

[54] R. Matzdorf, Surf. Sci. Rep., 30 (1998) 153.

[55] J.B. Hudson, Surface Science: An introduction, (1992).

[56] H. Ibach, D.L. Mills, Electron Energy Loss Spectroscopy, (1982).

[57] CAMD 2003 Annual Report, edited by L. A. Broussard http://www.camd.lsu.edu/newsletters/CAMD2003AR.pdf, (2003).

[58] H. Lüth, Solid Surfaces, Interfaces and Thin Films, (2001).

[59] P.V. Kamat, J. Phys. Chem. B, 106 (2002) 7729.

[60] Q. Fu, T. Wagner, Surf. Sci. Rep., 62 (2007) 431-498.

[61] A. Fujishima, X. Zhang, D. Tryk, Surf. Sci. Rep., 63 (2008) 515-582.

[62] G.C. Bond, D.T. Thompson, Catal. Rev. Sci. Eng., 41 (1999) 319.

[63] G.J. Hutchings, D.W. Goodman, Topics Catal., 44 (2007).

[64] G.J. Hutchings, Catal. Today, 100 (2005) 55.

[65] R.A.v. Santen, H. Kuipers, Adv. Catal., 35 (1987) 337.

[66] A.L.d. Oliveira, A. Wolf, F. Schüth, Catal. Lett., 73 (2001) 157.

[67] S. Wendt, P.T. Sprunger, E. Lira, G.K.H. Madsen, Z. Li, J.O. Hansen, J. Matthiesen, A. Blekinge-Rasmussen, E. Laegsgaard, B. Hammer, F. Besenbacher, Science, 320 (2008) 1755-1759.

119

[68] E. Lira, S. Wendt, P. Huo, J.Ø. Hansen, R. Streber, S. Porsgaard, Y. Wei, R. Bechstein, E. Lægsgaard, F. Besenbacher, J. Am. Chem. Soc., 133 (2011) 6529.

[69] E. Lægsgaard, F. Besenbacher, K. Mortensen, I. Stensgaard, J. Microsc., 152 (1988) 663.

[70] U. Diebold, J.F. Anderson, K.O. Ng, D. Vanderbilt, Phys. Rev. Lett., 77 (1996) 1322.

[71] P.A. Cox, V.E. Henrich, The Surface Science of Metal Oxides, Cambridge University Press, Cambridge, 1994.

[72] X. Lai, T.P.S. Clair, M. Valden, D.W. Goodman, Prog. Surf. Sci., 59 (1998) 25.

[73] L. Zhang, R. Persaud, T.E. Madey, Phys. Rev. B, 56 (1997) 10549.

[74] D. Martin, F. Creuzet, J. Jupille, Y. Borensztein, P. Gadenne, Surf. Sci., 377-379 (1997) 958.

[75] D. Martin, J. Jupille, Y. Borensztein, Surf. Sci., 404 (1998) 433.

[76] K. Luo, T.P.S. Clair, X. Lai, D.W. Goodman, J. Phys. Chem. B, 104 (2000) 3050.

[77] D.A. Chen, M.C. Bartelt, K.F. McCarty, Surf. Sci., 464 (2000) L708.

[78] C. Su, J.C. Yeh, J.L. Lin, J.C. Lin, Appl. Surf. Sci., 169-170 (2001) 366.

[79] Y. Du, Z. Dohnálek, I. Lyubinetsky, J. Phys. Chem. C, 112 (2008) 2649.

[80] S. Wendt, R. Schaub, J. Matthiesen, E.K. Vestergaard, E. Wahlström, M.D. Rasmussen, P. Thostrup, L.M. Molina, E. Lægsgaard, I. Stensgaard, B. Hammer, F. Besenbacher, Surf. Sci., 598 (2005) 226.

[81] C. Lun Pang, R. Lindsay, G. Thornton, Chemical Society Reviews, 37 (2008) 2328.

[82] W.S. Epling, C.H.F. Peden, M.A. Henderson, U. Diebold, Surf. Sci., 412-413 (1998) 333.

[83] X. Wu, A. Selloni, M. Lazzeri, S.K. Nayak, Phys. Rev. B, 68 (2003) 241402(R).

[84] M.D. Rasmussen, L.M. Molina, B. Hammer, J. Chem. Phys., 120 (2004) 988.

[85] K. Tsutsumi, O. Aita, K. Ichikawa, Phys. Rev. B, 15 (1977) 4638.

[86] Z. Zhang, S.P. Jeng, V. Henrich, Phys. Rev. B, 43 (1991) 12004.

[87] Y. Kitsudo, A. Iwamoto, H. Matsumoto, K. Mitsuhara, T. Nishimura, M. Takizawa, T. Akita, Y. Maeda, Y. Kido, Surf. Sci., 603 (2009) 2108.

[88] A. Howard, D.N.S. Clark, C.E.J. Mitchell, R.G. Egdell, V.R. Dhanak, Surf. Sci., 518 (2002) 210.

[89] T. Okazawa, M. Kohyama, Y. Kido, Surf. Sci., 600 (2006) 4430.

[90] M. Chen, D. Goodman, Structure–activity relationships in supported Au catalysts, Catalysis Today, 111 (2006) 22-33.

[91] H. Hövel, G. Grimm, M. Pollmann, B. Reihl, Phys. Rev. Lett., 81 (1998) 4608.

[92] A. Romanyuk, P. Oelhafen, Sol. Energy Mater. & Sol. Cells, 91 (2007) 1051.

[93] X. Bao, M. Muhler, T.S. Niedrig, R. Schlögl, Phys. Rev. B, 54 (1996) 2249.

[94] L.H. Tjeng, M.B. Meinders, J.V. Elp, J. Ghijsen, G.A. Sawatzky, R.L. Johnson, Phys. Rev. B, 41 (1990) 3190.

[95] S.W. Gaarenstroom, N. Winograd, J. Chem. Phys., 67 (1977) 15.

[96] S. Wendt, P.T. Sprunger, E. Lira, G.K.H. Madsen, Z. Li, J. Hansen, J. Matthiesen, A.B. Rasmussen, E. Lægsgaard, B. Hammer, F. Besenbacher, Science, 320 (2008) 1755.

[97] Reference Solar Spectral Irradiance: Air Mass 1.5, http://rredc.nrel.gov/solar/spectra/am1.5/#about.

[98] G. Xu, M. Tazawa, P. Jin, S. Nakao, K. Yoshimura, Appl. Phys. Lett., 82 (2003) 3811.

[99] J.A.A.J. Perenboom, P. Wyder, P. Meier, Phys. Rep., 78 (1981) 173.

[100] C.G. Granqvist, O. Hunderi, Phys. Rev. B, 16 (1977) 3515.

[101] E. Anno, J. Opt. Soc. Am. B, 3 (1986) 194.

[102] J.P. Marton, J.R. Lemon, Phys. Rev. B, 4 (1971) 271.

[103] J. Kottman, O. Martin, Optics Express, 8 (2001) 655.

[104] H.-J. Freund, Surf. Sci., 500 (2001) 271.

[105] G. Mie, Ann. Phys., 25 (1908) 377.

[106] N. Nilius, N. Ernst, H.-J. Freund, Chem. Phys. Lett., 349 (2001) 351.

[107] N. Nilius, N. Ernst, H.-J. Freund, Photon emission spectroscopy of individual oxide-supported silver clusters in the STM, Phys. Rev. Lett., 84 (2000) 3994.

[108] N. Nilius, N. Ernst, H.-J. Freund, Photon emission from individual supported gold clusters: thin film versus bulk oxide, Surf. Sci., 478 (2001) L327-L332.

[109] R.L. Kurtz, R.L. Stockbauer, T.E. Madey, Chemically Modified Oxide Surfaces, 3 (1990) 179.

[110] R.L. Kurtz, R.L. Stockbauer, T.E. Madey, Surf. Sci., 218 (1989) 178.

[111] K. Luo, T.P.S. Claire, X. Lai, D.W. Goodman, J. Phys. Chem. B, 104 (2000) 3050.

[112] W. Zhao, O. Kizilkaya, Y. Losovyi, R.L. Kurtz, P.T. Sprunger, Electronic structure of silver nanowires on Cu(110), Nuclear Instr. and Methods, 582 (2007) 267-269.

[113] L.L. Kesmodel, J.A. Gates, Y.W. Chung, Phys. Rev. B, 23 (1981) 489.

[114] K.T. Park, M. Pan, V. Meunier, E.W. Plummer, Phys. Rev. B, 75 (2007) 245415.

[115] K.T. Park, V. Meunier, M. Pan, W.A. Shelton, N.-H. Yu, E.W. Plummer, Surf. Sci., 603 (2009) 3131.

[116] U. Diebold, W. Hebenstreit, G. Leonardelli, M. Schmid, P. Varga, Phys. Rev. Lett., 81 (1998) 405.

[117] M. Rocca, Y. Li, F.B.d. Mongeot, U. Valbusa, Phys. Rev. B, 52 (1995) 14947.

[118] A. Marini, R.D. Sole, G. Onida, Phys. Rev. B, 66 (2002) 115101.

[119] H. Hövel, S. Fritz, A. Hilger, U. Kreibig, M. Vollmer, Phys. Rev. B, 48 (1993) 18178.

[120] M. Quinten, Appl. Phys. B: Lasers & Optics, 67 (1998) 101.

[121] O. Stenzel, A. Stendal, M. Roder, C.v. Borczyskowski, Tuning of the plasmon absorption frequency of silver and indium nanoclusters via thin amorphous silicon films, Pure and Applied Optics: Journal of the European Optical Society Part A, 6 (1997) 577-588.

[122] G. Xu, M. Tazawa, P. Jin, S. Nakao, K. Yoshimura, Wavelength tuning of surface plasmon resonance using dielectric layers on silver island films, Appl. Phys. Lett., 82 (2003) 3811-3813.

[123] J. Kottman, O. Martin, Plasmon resonant coupling in metallic nanowires, Optics Expr., 8 (2001) 655-663.

[124] J. Kottman, O. Martin, D. Smith, S. Schultz, Spectral Response of plasmon resonant nanoparticles with a non-regular shape, Optics Expr., 6 (2000) 213-219.

[125] J. Kottmann, O. Martin, D. Smith, S. Schultz, Dramatic localized electromagnetic enhancement in plasmon resonant nanowires, Chem. Phys. Lett, 341 (2001) 1-6.

[126] C.N. Satterfield, Heterogeneneous Catalysis in Industrial Practice, (1991).

[127] Y. Choi, K. Futagami, T. Fujitani, J. Nakamura, Appl. Catal. A, 208 (2001) 163.

[128] T. Fujitani, J. Nakamura, Appl. Catal. A, 191 (2000) 111.

[129] J.D. Grunwaldt, A.M. Molenbroek, N.Y. Topsoe, H. Topsoe, B.S. Clausen, J. Catal, 194 (2000) 452.

[130] N. Nomura, T. Tagawa, S. Goto, Appl. Catal. A, 166 (1998) 321.

[131] K.K. Bando, K. Sayama, H. Kusama, K. Okabe, H. Arakawa, Appl. Catal. A, 165 (1997) 391.

[132] H. Sakurai, M. Haruta, Appl. Catal. A, 127 (1995) 93.

[133] H. Sakurai, M. Haruta, Catal. Today, 29 (1996) 361.

[134] J. Strunk, K. Kähler, X. Xia, M. Comotti, F. Schüth, T. Reinecke, M. Muhler, Appl. Catal. A, 359 (2009) 121.

[135] T.M. Parker, N.G. Condon, R. Lindsay, F.M. Leibsle, G. Thornton, Surf. Sci. Lett., 415 (1998) L1046.

[136] C.T. Campbell, A. Ludviksson, J. Vac. Sci. Technol. A, 12 (1994) 1825.

[137] J. Ghijsen, L.H. Tjeng, J.v. Elp, H. Eskes, J. Westerink, G.A. Sawatzky, M.T. Czyzyk, Phys. Rev. B, 38 (1988) 11322.

[138] J.A. Rodriguez, J. Evans, J. Graciani, J.B. Park, P. Liu, J. Hrbek, J.F. Sanz, J. Phys. Chem. C, 113 (2009) 7364.

[139] D.A. Chen, M.C. Bartelt, R.Q. Hwang, K.F. McCarty, Surf. Sci., 450 (2000) 78.

[140] L. Vitos, A.V. Ruban, H.L. Skriver, J. Kollár, Surf. Sci., 411 (1998) 186.

[141] S.P. Bates, G. Kresse, M.J. Gillan, Surf. Sci., 385 (1997) 386.

[142] U. Diebold, J. Lehman, T. Mahmoud, M. Kuhn, G. Leonardelli, W. Hebenstreit, M. Schmid, P. Varga, Surf. Sci., 411 (1998) 137.

[143] H. Sakurai, S. Tsubota, M. Haruta, Appl. Catal. A, 102 (1993) 125.

[144] M. Haruta, CATTECH, 6 (2002) 102.

[145] D.C. Meier, D.W. Goodman, J. Am. Chem. Soc., 126 (2004) 1892.

[146] M. Chen, Y. Cai, Z. Yan, D.W. Goodman, J. Am. Chem. Soc., 128 (2006) 6341.

[147] M. Valden, X. Lai, D.W. Goodman, Science, 11 (1998) 1647.

[148] Y. Maeda, T. Fujitani, S. Tsubota, M. Haruta, Surf. Sci., 562 (2004) 1.

[149] C.E.J. Mitchell, A. Howard, M. Carney, R.G. Egdell, Surf. Sci., 490 (2001) 196.

Vita

Fei Wang was born and raised in Hefei, China. He received his Bachelor of Science degree majored in physics from University of Science and Technology of China, China, in 2004. He entered Louisiana State University (LSU), in 2005 to pursue his doctoral degree in physics.